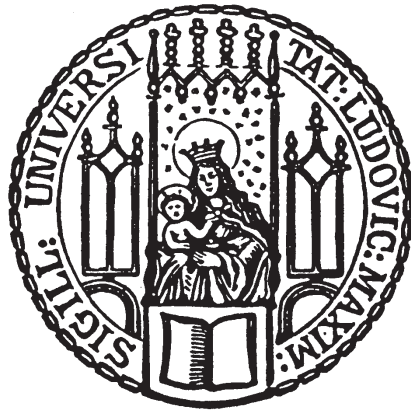


Search for new physics in  $pp$  collisions in  
final states with tau leptons,  $b$ -jets and  
missing transverse momentum with the  
ATLAS detector in LHC Run 2



DISSERTATION

an der Fakultät für Physik  
der Ludwig-Maximilians-Universität München

vorgelegt von

Ferdinand Krieter

geboren in München

München, 26. Februar 2021

Erstgutachter: PD Dr. Alexander Mann

Zweitgutachter: Prof. Dr. Wolfgang Dünneberger

Tag der mündlichen Prüfung: 22. April 2021

# Zusammenfassung

Obwohl die Vorhersagen des Standardmodells (SM) der Teilchenphysik eine hervorragende Übereinstimmung mit experimentellen Daten aufweisen, deuten dennoch zahlreiche Beobachtungen auf Physik jenseits des SMs hin. In dieser Arbeit wird eine Suche nach neuer Physik in Endzuständen mit Tau-Leptonen,  $b$ -Jets und fehlendem Transversalimpuls vorgestellt. Solche Signaturen können in vielen Erweiterungen des SMs auftreten, welche versuchen, Lösungen zu einigen der offenen Fragestellungen zu liefern. Die Suche benutzt Daten aus Proton-Proton-Kollisionsereignissen mit einer Schwerpunktsenergie von  $\sqrt{s} = 13 \text{ TeV}$ , aufgezeichnet mit dem ATLAS-Detektor in Run 2 des Large Hadron Colliders, was einer integrierten Luminosität von  $139 \text{ fb}^{-1}$  entspricht.

Es werden zwei Signalmodelle betrachtet. Das erste beschreibt die Paarproduktion des supersymmetrischen Partners des Top-Quarks, während das andere Paarproduktion skalarer Leptoquarks der dritten Generation behandelt. In den Daten wurden keine signifikanten Abweichungen von der SM-Vorhersage beobachtet, und die Ergebnisse werden in Form von Ausschlussgrenzen auf die Signalparameter interpretiert. Im Rahmen der vorgestellten Modelle werden Top-Quark-Partner mit Massen von bis zu  $1,4 \text{ TeV}$  sowie skalare Leptoquarks mit Massen von bis zu  $1,25 \text{ TeV}$  mit einem Konfidenzniveau von  $95 \%$  ausgeschlossen.



# Abstract

While the predictions made by the Standard Model (SM) of particle physics show an exceptionally good agreement with experimental data, numerous observations point towards physics beyond the SM. In this thesis, a search for new physics in final states with tau leptons,  $b$ -jets and missing transverse momentum is presented. Such signatures can emerge in multiple extensions of the SM which try to provide solutions to some of the open problems. The search uses data of proton–proton collision events at a center-of-mass energy of  $\sqrt{s} = 13$  TeV, recorded with the ATLAS detector in Run 2 of the Large Hadron Collider, corresponding to an integrated luminosity of  $139 \text{ fb}^{-1}$ .

Two signal models are considered in this thesis. The first describes the pair production of the supersymmetric partner of the top quark, while the other involves pair-produced scalar leptoquarks of the third generation. No significant deviations from the SM prediction are observed in the data, and the results are interpreted in terms of exclusion limits on the signal parameters. In the context of the presented models, top-quark partners with masses of up to 1.4 TeV and scalar third-generation leptoquarks with masses of up to 1.25 TeV are excluded at 95 % confidence level.



# Contents

|          |  |           |
|----------|--|-----------|
| <b>1</b> | <b>Introduction</b>  | <b>1</b>  |
| <b>2</b> | <b>Theory</b>  | <b>3</b>  |
| 2.1      | The Standard Model of particle physics . . . . .                   | 3         |
| 2.1.1    | Particle content and interactions . . . . .                        | 4         |
| 2.1.2    | Open questions . . . . .   | 5         |
| 2.2      | Supersymmetry . . . . .  | 8         |
| 2.2.1    | Minimal Supersymmetric Standard Model . . . . .                    | 10        |
| 2.2.2    | $R$ -Parity . . . . .  | 11        |
| 2.2.3    | Symmetry breaking . . . . .  | 12        |
| 2.3      | Leptoquarks . . . . .  | 13        |
| 2.3.1    | Motivation . . . . .   | 13        |
| 2.3.2    | Phenomenology . . . . .  | 14        |
| 2.4      | Simplified models . . . . .  | 15        |
| 2.4.1    | Pair production of top squarks decaying via tau sleptons . . . . . | 16        |
| 2.4.2    | Pair production of third-generation scalar leptoquarks . . . . .   | 18        |
| <b>3</b> | <b>Experimental Setup</b>  | <b>21</b> |
| 3.1      | The Large Hadron Collider . . . . .                                | 21        |
| 3.2      | The ATLAS Experiment . . . . .                                     | 22        |
| 3.2.1    | Coordinate system . . . . .  | 23        |
| 3.2.2    | Detector components . . . . .                                      | 24        |
| 3.2.3    | Trigger system . . . . .   | 28        |
| 3.2.4    | Luminosity and pile-up . . . . .                                   | 29        |
| <b>4</b> | <b>Analysis overview</b>   | <b>31</b> |
| 4.1      | Analysis strategy outline . . . . .                                | 31        |
| 4.2      | Collision data . . . . .   | 33        |
| 4.3      | Simulation . . . . .   | 33        |
| 4.3.1    | Background . . . . .   | 35        |
| 4.3.2    | Top squarks decaying via tau sleptons . . . . .                    | 37        |
| 4.3.3    | Third-generation scalar leptoquarks . . . . .                      | 38        |
| 4.4      | Object definitions . . . . .                                       | 39        |
| 4.4.1    | Tracks and vertices . . . . .                                      | 40        |
| 4.4.2    | Jets . . . . .   | 40        |
| 4.4.3    | $b$ -tagging . . . . .   | 41        |

|           |  |           |
|-----------|--|-----------|
| 4.4.4     | Electrons . . . . .  | 41        |
| 4.4.5     | Muons . . . . .  | 42        |
| 4.4.6     | Hadronically decaying tau leptons . . . . .                        | 43        |
| 4.4.7     | Overlap removal . . . . .  | 44        |
| 4.4.8     | Missing transverse momentum . . . . .                              | 45        |
| 4.5       | Kinematic observables . . . . .                                    | 46        |
| 4.6       | Trigger . . . . .  | 47        |
| 4.7       | Event preselection . . . . .                                       | 49        |
| <b>5</b>  | <b>Statistical methods</b>   | <b>53</b> |
| 5.1       | Likelihood . . . . .   | 53        |
| 5.2       | Hypothesis tests . . . . .   | 54        |
| 5.3       | Fit setups . . . . .   | 56        |
| <b>6</b>  | <b>Signal regions</b>  | <b>59</b> |
| 6.1       | General optimization strategy . . . . .                            | 59        |
| 6.2       | Signal region in the di-tau channel . . . . .                      | 60        |
| 6.3       | Signal regions in the single-tau channel . . . . .                 | 64        |
| <b>7</b>  | <b>Background estimation and validation</b>                        | <b>69</b> |
| 7.1       | Control and validation regions in the di-tau channel . . . . .     | 69        |
| 7.2       | Control and validation regions in the single-tau channel . . . . . | 71        |
| <b>8</b>  | <b>Systematic uncertainties</b>                                    | <b>75</b> |
| 8.1       | Experimental systematic uncertainties . . . . .                    | 75        |
| 8.1.1     | Jets . . . . .   | 75        |
| 8.1.2     | Electrons and muons . . . . .                                      | 76        |
| 8.1.3     | Taus . . . . .   | 76        |
| 8.1.4     | Missing transverse momentum . . . . .                              | 76        |
| 8.1.5     | Luminosity and pile-up reweighting . . . . .                       | 76        |
| 8.2       | Theory uncertainties . . . . .                                     | 77        |
| 8.2.1     | Sources of theory uncertainties . . . . .                          | 77        |
| 8.2.2     | Background theory uncertainties . . . . .                          | 79        |
| 8.2.3     | Signal theory uncertainties . . . . .                              | 80        |
| 8.3       | Impact on signal regions . . . . .                                 | 81        |
| <b>9</b>  | <b>Results</b>   | <b>83</b> |
| 9.1       | Observations . . . . .   | 83        |
| 9.2       | Exclusion limits . . . . .   | 89        |
| 9.3       | Model-independent limits . . . . .                                 | 92        |
| <b>10</b> | <b>Conclusion</b>  | <b>93</b> |
|           | <b>Bibliography</b>  | <b>95</b> |

|  |            |
|--|------------|
| <b>List of abbreviations</b>                             | <b>115</b> |
| <b>Appendix</b>  | <b>117</b> |
| A Stop-stau exclusion limits per signal region . . . . . | 117        |
| B Additional data vs. MC comparison plots . . . . .      | 119        |
| <b>Acknowledgements</b>                                  | <b>131</b> |



# 1 Introduction

The Standard Model (SM) of particle physics provides a remarkably successful theoretical framework to describe the fundamental interactions of elementary particles with the exception of gravity. The discovery of its last missing building block, the Higgs boson, at the Large Hadron Collider LHC in 2012 marks an important milestone in high-energy physics while also putting the spotlight on the question of what comes next. The center-of-mass energy of proton–proton collision has since been increased to 13 TeV, shifting the experimental frontier to unprecedented energy scales.

What is the reason for the matter–antimatter asymmetry in the universe? What is the nature of dark matter? These and many other questions have been left largely unanswered by the SM so far. Furthermore, the unification of the electromagnetic and weak force motivates that a unification of all fundamental interactions might be possible at even higher energy scales. Hence, the SM is believed to be embedded in a much more fundamental theory, an all-encompassing description of all fundamental particles and interactions.

A step in this direction is presented by the introduction of a new symmetry, called Supersymmetry (SUSY), which postulates the existence of supersymmetric partners of the known SM particles, differing in spin by half a unit. As such particles have not been observed yet, SUSY must be spontaneously broken which allows these superpartners to acquire a higher mass than their SM counterparts. Due to the strong coupling to the Higgs field, the top squark, the supersymmetric partner of the top quark, might nonetheless be sufficiently light and thus within the reach of the LHC [1].

Many extensions of the SM, such as Grand Unified Theories (GUTs), predict the existence of new bosonic states, called leptoquarks, which carry both baryon and lepton quantum numbers and fractional electric charge. Theories involving leptoquarks can potentially explain the apparent symmetries of the quark and lepton sector in the SM. Experimental constraints suggest that there are three generations of leptoquarks, each coupling only to the quarks and leptons of the same generation [2].

In this thesis the results from a search for new physics are reported. To this end, the full dataset of Run 2 of the LHC, recorded with the ATLAS detector between 2015 and 2018, is analyzed. The search strategy has been optimized for two simplified models: One involves pair production of top squarks, the other considers pair-produced scalar leptoquarks of the third generation. The analysis focuses on final states with tau leptons,  $b$ -quarks and particles invisible to the detector.

The thesis is structured as follows: The main theoretical concepts and investigated

signal models are introduced in Chapter 2. The LHC and ATLAS detector are described in Chapter 3. An overview of the general analysis strategy, the recorded and simulated data and reconstruction of physics objects is given in Chapter 4. After a brief review of the statistical methods in Chapter 5, the sensitivity optimization and background estimation strategies are described Chapters 6 and 7, respectively. The results are presented and interpreted in Chapter 9, followed by a brief conclusion in Chapter 10.

## 2 Theory

The Standard Model (SM) of particle physics presents a description of all elementary particles and their interactions. This chapter reviews its particle content and interactions and discusses its shortcomings that motivate the introduction of new physics beyond the SM. The SM is widely believed to be a low-energy approximation to a more fundamental theory. One possible step towards a unified ‘theory of everything’ might be given by a proposed fundamental symmetry relating bosons to fermions and vice versa. In this chapter, the key concepts and predictions of this so-called Supersymmetry (SUSY) are established and the supersymmetric model, on which the presented search is based on, is introduced. Furthermore, an effective model of leptoquarks, hypothetical bosons coupling to both a quark and a lepton, is discussed. One such model of leptoquark production is considered as it exhibits a phenomenology to which the presented search is also highly sensitive.

### 2.1 The Standard Model of particle physics

With the exception of gravity, the SM provides a renormalizable quantum fields theory of all fundamental interactions of quarks and leptons, the constituents of all known matter, as well as their charge-conjugates representing antimatter: the strong interaction described by quantum chromodynamics (QCD), as well as the electromagnetic and weak interactions which have been combined in a single electroweak framework. The dynamics are governed by the symmetries of local gauge invariance which introduce gauge fields that couple to the fermions and mediate their interactions. The structure of the SM is given by the combination of these gauge groups, i. e.

$$SU(3)_C \times SU(2)_L \times U(1)_Y, \quad (2.1)$$

where the subscripts  $C$ ,  $L$  and  $Y$  denote the associated conserved charges: color, weak isospin and hypercharge, respectively. The strong interaction is described by  $SU(3)_C$ , while  $SU(2)_L \times U(1)_Y$  describes the electroweak interactions.

An educational introduction and rigorous mathematical description of the SM can be found in Refs. [3, 4] and is not repeated here. Instead, the following section briefly reviews its main building blocks, the elementary matter particles and force carriers.

### 2.1.1 Particle content and interactions

The gauge bosons of the strong interaction are the massless gluons which couple to the three  $SU(3)_C$  representations of the quarks. These representations are denoted by the colors red, green and blue. Antiquarks carry the corresponding anticolors. This analogy helps to visualize the phenomenological concept of color confinement: Below a critical temperature color-charged particles cannot appear isolated. They must therefore form colorless hadrons, bound states of either three (anti-)quarks of each (anti-)color or quark-antiquark pairs with canceling color and anticolor. Gluons carry both color and anticolor and feature strong self-interaction, leading to the short range of the strong force.

A single complex  $SU(2)_L$  doublet of spin-0 fields is introduced which acquire a non-zero vacuum expectation value. This leads to a spontaneous breakdown of the electroweak symmetry, generating a different gauge group,  $U(1)_{em}$ , which is identified with the familiar electromagnetic interaction of charged particles mediated by the photon  $\gamma$ . The residual  $W^\pm$  and  $Z$  bosons become massive and are identified with the mediators of the weak interaction which consequently has only a short range. The electromagnetic interaction with its massless photon on the other hand has an infinite range. The charged  $W$  bosons couple to themselves, left-chiral (right-chiral) (anti-)fermions and photons, while the neutral  $Z$  boson can couple to fermions (and antifermions) of any chirality and the  $W$  bosons. This implementation of electroweak symmetry breaking is known as the Higgs mechanism and leads to the massive spin-0 Higgs boson, the last basic building block of the SM discovered in 2012 [5, 6]. The Yukawa-type interactions of the fermions, except neutrinos, with the scalar field allows them to acquire masses without spoiling the gauge invariance of the theory.

The magnitude of the coupling constants associated to each interaction determines their strengths. This leads to a hierarchy in which, as their names suggest, the strong interaction dominates and the weak interaction, aside from gravity, is the most feeble. As a consequence, the production rate of colored particles is much higher at a hadron collider such as the LHC compared to electroweak production processes.

Figure 2.1 gives a summary of all known particles in the SM. The content of the table and the following discussion is restricted to fermions, as antifermions feature the same structure and masses but with opposite quantum numbers. Fermions come in three generations which only differ from one another in mass. The individual states are therefore also often referred to as different flavors of quarks and leptons. The three quark generations come in two types: Up-type quarks ( $u, c, t$ ) carry a fractional charge of  $+2/3 e$ , while down-type quarks ( $d, s, b$ ) carry a fractional charge of  $-1/3 e$ . Only the  $W$  boson can couple to quarks of different generations, and flavor-changing neutral currents, i.e. via  $Z$ -boson exchange, are forbidden in the SM at first order of perturbation theory (tree-level). The inter-generational couplings, given by the Cabibbo–Kobayashi–Maskawa (CKM) matrix, are weakest for quarks of the first and third generation and strongest for quarks within the same generation. The CKM matrix

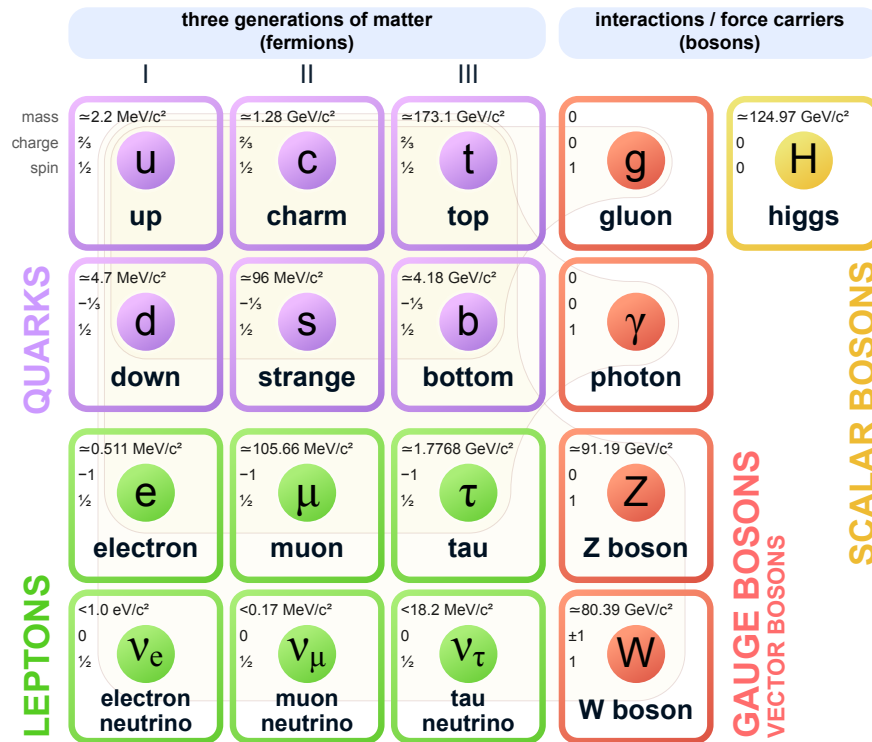


**Figure 2.1:** Particle content of the Standard Model (SM). Figure adapted from Ref. [7].

also contains a complex phase giving rise to charge-parity ( $CP$ ) violation in the quark sector. The three generations of leptons are all colorless and consist of the negatively charged electron, muon and tau lepton and their associated uncharged neutrinos. In the SM, neutrinos are treated as massless, but observations of neutrino oscillations show that at least two neutrino flavors are in fact massive [8, 9]. Due to their larger mass, fermions of the second and third generation eventually decay into first-generation fermions. In particular, the top quark is so heavy that it decays before it can form hadrons.

### 2.1.2 Open questions

Despite its success at predicting particle interactions at energy scales across many orders of magnitude, the SM leaves several problems unanswered. In the following, several experimental observations and theoretical considerations are discussed which all hint at a more fundamental description. Such a theory might predict new phenomena at even higher energy scales and is approximated by the SM at the currently accessible scales.

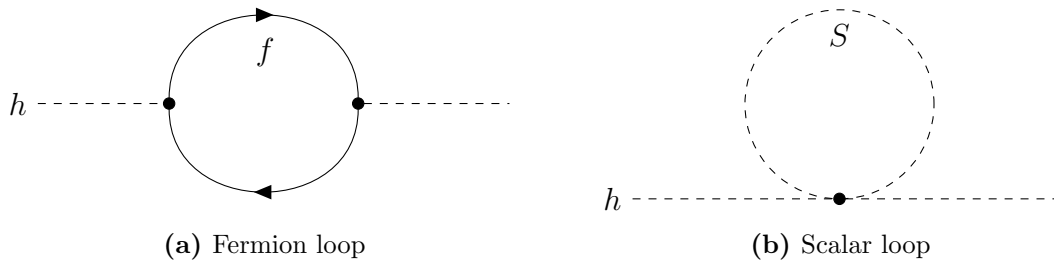


**Figure 2.2:** One-loop contributions to the Higgs propagator due to a fermion (a) or a boson (b).

### Dark matter

The distribution of visible matter in a galaxy can be derived from the relative brightness across it. For spiral galaxies such as our own it is observed that the majority of luminous matter is concentrated in the central region. According to Newtonian dynamics, the tangential velocity of matter at a distance  $r$  from the center is therefore expected to fall as  $1/\sqrt{r}$ . However, the observed rotational velocities deduced from spectral analysis seem to take an almost constant value above a certain distance, indicating the presence of huge amounts of non-luminous ‘dark matter’ [10].

Further evidence for the presence of dark matter stems from gravitational lensing effects. A massive object such as a cluster of galaxies causes spacetime to curve, deflecting light emitted from a distant source behind the object as it travels towards the observer. With all three objects aligned, the distant light source, e. g. a galaxy, appears as a distorted image of itself around the galaxy cluster in the foreground. It is found, however, that the mass of the visible luminous matter of the cluster alone cannot account for the lensing effects [11].

The elusiveness of dark matter implies that it is stable and does not interact electromagnetically or via the strong interaction. While the neutrinos in the SM also feature these properties, their relativistic character does not allow for a formation of the dense dark matter structures derived from astrophysical observations and simulations. The cosmological Lambda-CDM (cold dark matter) model [12, 13] therefore assumes that dark matter is composed mainly of so far undiscovered weakly interacting massive particles (WIMPs). As will be discussed in Section 2.2.2, SUSY can offer a WIMP candidate.

### The Fine-Tuning Problem

The masses of all SM particles are subject to radiative corrections introduced by virtual loop contributions. The mass of the scalar Higgs boson is especially prone to quantum corrections as opposed to fermions or gauge bosons, which are largely protected by chiral or local gauge symmetries, respectively [14]. Figure 2.2 shows examples for

a second order correction to the Higgs propagator with a fermionic or bosonic loop. Unitarity demands to consider all possible higher order corrections and then add their contributions. The leading correction terms are

$$\Delta m_H = -\frac{|\lambda_f|^2}{8\pi^2} \lambda_{UV}^2 + \dots \quad (2.2)$$

for a loop involving a fermion  $f$ , and

$$\Delta m_H = \frac{\lambda_S}{16\pi^2} \lambda_{UV}^2 + \dots \quad (2.3)$$

for a loop with a scalar boson  $S$ , with coupling constants  $\lambda_f$  and  $\lambda_S$ , respectively, and a quadratical divergence in the ultraviolet momentum cut-off scale  $\lambda_{UV}$  used in the regularization scheme [15]. This cut-off scale should be interpreted as a lower bound on the energy scale at which new physics are expected to enter. If the Planck mass  $m_P = \sqrt{\hbar c/G} \approx 10^{19}$  GeV is the cut-off, these corrections become many orders of magnitude larger than the observed Higgs mass of about 125 GeV. An extreme amount of fine-tuning of all the parameters entering the calculation would therefore be required in order to retain the observed Higgs mass which seems quite unnatural. As fermionic and bosonic loops contribute with opposite sign, the symmetry between fermions and boson proposed by SUSY offers a natural solution to this issue.

### Unification of gauge couplings

The unification of the electromagnetic and weak forces in the SM sparks the question whether all three force can be described by a single gauge group. Such theories attempting to unify the fundamental forces are commonly referred to as grand unified theories (GUTs). The strength of an interaction as represented by its coupling constant depends on the scale of the transferred momentum. This energy dependence, coined ‘running’ of the coupling constants, is shown in Figure 2.3. The left plot shows that the values of the three couplings, extrapolated following the predictions of the SM, do not meet in one single point. However, the introduction of new fields predicted by SUSY can lead to a natural convergence of the couplings as shown in the right plot. The unification scale depends on the masses of these new fields as they modify the energy dependence of the couplings.

### *B*-Meson decays

Lepton universality states that the coupling of all leptons to gauge boson is flavor-independent. While this hypothesis agrees with the outcomes of multiple experiments, such as the measurement of the  $Z$ -boson partial decay widths at LEP [17], recent precision tests yield contradicting observations. The BaBar, Belle and LHCb experiments accumulated data on the measurements of several observables related to the decay of  $B$ -

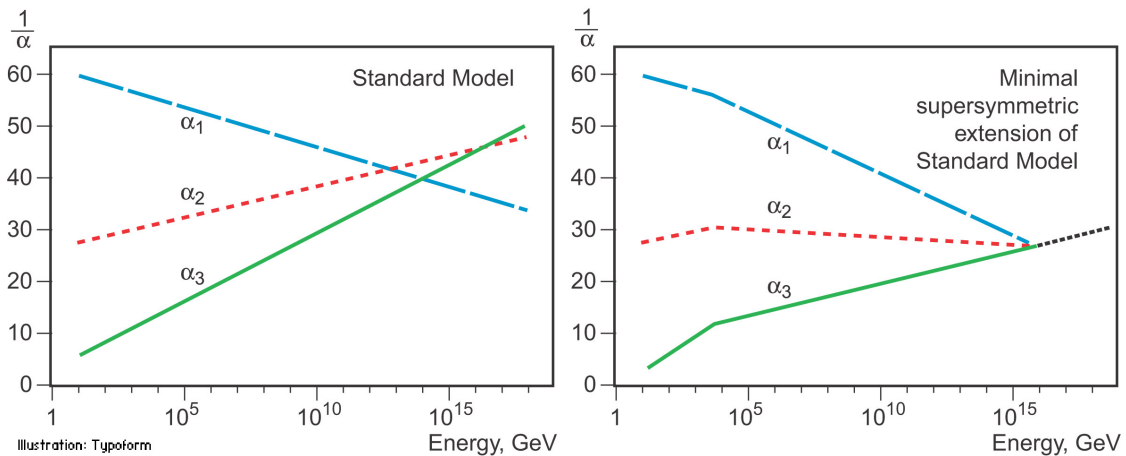


**Figure 2.3:** Running of the gauge couplings in the SM (left) and the MSSM (right). Here,  $\alpha_1$ ,  $\alpha_2$  and  $\alpha_3$  denote the coupling constants of the  $U(1)_Y$ ,  $SU(2)_L$  and  $SU(3)_C$  gauge group, respectively. Figure adapted from Ref. [16].

mesons showing in many cases significant deviations from the SM predictions [18–24]. Take for example the following ratios of branching ratios:

$$R(D^{(*)}) = \frac{B(\bar{B} \rightarrow D^{(*)}\tau\bar{\nu}_\tau)}{B(\bar{B} \rightarrow D^{(*)}\ell\bar{\nu}_\ell)}, \quad (2.4)$$

$$R(K^{(*)}) = \frac{B(B \rightarrow K^{(*)}\mu\mu)}{B(B \rightarrow K^{(*)}ee)}, \quad (2.5)$$

where  $\ell$  denotes an electron or a muon. The combined measurements on  $R(D^{(*)})$  by Belle [19] and on  $R(K^{(*)})$  by LHCb [20, 21] deviate by 1.6 and 2.5 standard deviations ( $\sigma$ ), respectively, from SM calculations. Angular observables of the decay products exhibit deviations of similar magnitude [22–24]. These observations might hint at new particles that introduce sources for lepton-universality violation.

## 2.2 Supersymmetry

The first concepts of Supersymmetry (SUSY) as an extension of the SM were developed in the 1970s [25–30]. This section aims to convey a basic understanding of the general concepts of SUSY, the particle content of the Minimal Supersymmetric SM (MSSM),  $R$ -parity and its consequences and the mechanism of SUSY breaking. It follows closely the pedagogical introductions provided by Stephen P. Martin [15], Mauricio Bustamante et al [31] as well as Howard Baer and Xerxes Tata [14].

SUSY proposes a symmetry between the elementary fermions and bosons. With respect to the SM, the particle content is then (more than) doubled, as each known particle is associated with a supersymmetric partner, or superpartner, which differs in spin by

one half unit.

Consider a fermionic operator  $Q$  as the generator for SUSY transformations:

$$Q|\text{Fermion}\rangle = |\text{Boson}\rangle, \quad Q|\text{Boson}\rangle = |\text{Fermion}\rangle, \quad (2.6)$$

with the spinor  $Q$  and its hermitian conjugate  $\bar{Q}$ , taken in the Weyl representation<sup>1</sup>. This fermionic operator only changes the spin of a state by  $1/2$  and leaves all other quantum numbers unchanged. While it is in principle possible to introduce more generators, only the approach with one generator is considered here. This is called  $N = 1$  SUSY and presents the only direct extension of the SM with phenomenological relevance [14].

The SUSY algebra can be summarized with the following (anti-)commutation relations:

$$[Q_\alpha, P^\mu] = 0, \quad [\bar{Q}^{\dot{\alpha}}, P^\mu] = 0, \quad (2.7)$$

$$[Q_\alpha, M^{\mu\nu}] = i(\sigma^{\mu\nu})_\alpha{}^\beta Q_\beta, \quad [\bar{Q}_{\dot{\alpha}}, M^{\mu\nu}] = i(\sigma^{\mu\nu})^{\dot{\alpha}}{}_{\dot{\beta}} \bar{Q}^{\dot{\beta}}, \quad (2.8)$$

$$\{Q_\alpha, Q_\beta\} = 0, \quad \{\bar{Q}^{\dot{\alpha}}, \bar{Q}^{\dot{\beta}}\} = 0, \quad (2.9)$$

$$\{Q_\alpha, \bar{Q}_{\dot{\beta}}\} = 2(\sigma^\mu)_{\alpha\dot{\beta}} P_\mu, \quad (2.10)$$

where  $P^\mu$  denotes the generator for spacetime translations and  $M^{\mu\nu}$  the generator for Lorentz transformations. The Minkowski metric is defined as  $\eta_{\mu\nu} = \text{diag}(+, -, -, -)$  while  $\sigma^\mu = (\mathbb{1}_2, \sigma^i)$  and  $\bar{\sigma}^\mu = (\mathbb{1}_2, -\sigma^i)$  with  $i \in \{1, 2, 3\}$  contain the Pauli matrices  $\sigma_i$  and  $\sigma^{\mu\nu} = \frac{i}{4}[\gamma^\mu, \gamma^\nu]$  with the Dirac matrices  $\gamma^\mu$  taken in the Weyl basis.

From Equation (2.7) it follows that also the squared mass operator  $P^2 = P^\mu P_\mu$  commutes with  $Q$ , implying that superpartners must have the same mass. This is however not observed and thus SUSY has to be a broken symmetry such that superpartners acquire more mass than the SM particles. Possible realizations of SUSY breaking are explored in Section 2.2.3.

Equation (2.8) simply means that  $Q$  transforms as a spinor under spacetime rotations and that SUSY transformations are a priori global, i. e. independent of the position in spacetime. Furthermore it can be shown that  $Q$  also commutes with the generators of the gauge transformations. Thus all quantum numbers of the superpartners, with the exception of spin, match those of the associated SM partners.

Maybe the most striking implication is given by Equation (2.10): The anticommutator of a SUSY generator and its hermitian conjugate connects to a local coordinate translation. Therefore, if SUSY is promoted to a local symmetry, it naturally unifies the spacetime symmetry of general relativity with local SUSY transformations [32]. The resulting locally supersymmetric theory is called supergravity.

---

<sup>1</sup>Weyl spinors have two components and represent particles of spin  $1/2$ . The component with left (right) chirality is denoted by  $\psi_\alpha$  ( $\bar{\psi}^{\dot{\alpha}}$ ) with  $\alpha \in \{1, 2\}$ . The matrix  $\epsilon_{\alpha\beta} = \epsilon_{\dot{\alpha}\dot{\beta}} = i\sigma_2$  and  $\epsilon^{\alpha\beta} = \epsilon^{\dot{\alpha}\dot{\beta}} = -i\sigma_2$  can be used to raise and lower the spinorial indices.

SUSY is thus not only an internal symmetry of bosons and fermions but also inherently related to the isometries of spacetime represented by the Poincaré group. By adjoining the anticommuting, fermionic SUSY generator to the generators of translation and Lorentz transformations, as shown above, Haag, Lopuszański and Sohnius showed that this gives the most general (but non-trivial) extension of the Poincaré algebra [33]. This relation can only be achieved with fermionic SUSY generators, as bosonic ones are excluded by the fundamental Coleman-Mandula theorem [34].

### 2.2.1 Minimal Supersymmetric Standard Model

The Minimal Supersymmetric Standard Model (MSSM) is the supersymmetric extension of the SM containing the minimal set of new particles and interactions consistent with phenomenology. A representation of the SUSY algebra is given by supermultiplets combining fermion and boson states with the same quantum numbers apart from spin. In each supermultiplet the number of fermionic degrees of freedom must be equal to the number of bosonic ones.

The SM gauge bosons and gauge eigenstates of the fermions reside in such supermultiplets. The most straight-forward realization is given by chiral and gauge supermultiplets: A chiral supermultiplet contains a spin- $1/2$  Weyl fermion and its complex scalar superpartner, called *sfermion*. A massless spin-1 gauge boson together with its spin- $1/2$  superpartner the *gaugino* forms a gauge supermultiplet. By convention, superpartners of fermions have the prefix ‘s’ and superpartners of gauge bosons have the suffix ‘ino’. Expressed with symbols, the superpartners of the SM fields are denoted by a tilde symbol ( $\tilde{\phantom{x}}$ ) above the character. It should be noted that for the superpartner of a chiral particle, such as for example the left-handed top quark  $t_L$  and its superpartner, the top squark  $\tilde{t}_L$ , the subscript  $L/R$  is not related to the chirality of the SUSY field since it is scalar.

Given this structure, the scalar Higgs field is thus integrated into a chiral supermultiplet. To avoid gauge anomalies [15], and provide all particles (except the Higgs bosons) with a possibility to become massive, at least two chiral Higgs supermultiplets and therefore two weak isospin doublets  $H_u = (H_u^+, H_u^0)$  and  $H_d = (H_d^0, H_d^-)$  are required. The superscripts of the individual weak isospin components indicate their electrical charge.  $H_u$  can only couple to up-type quarks, while  $H_d$  only couples to down-type quarks. The two complex Higgs doublets have in total eight degrees of freedom. Three of them are absorbed by the weak gauge bosons giving them mass which leaves five degrees of freedom appearing as physical particles:

- $h^0, H^0$ : One light and one heavy, neutral,  $CP$ -even Higgs, respectively. The former is usually identified with the SM Higgs boson.
- $A^0$ : One neutral,  $CP$ -odd Higgs boson.
- $H^+, H^-$ : Two oppositely charged Higgs bosons.

The superpartners of the neutral (charged) Higgs bosons, called Higgsinos, will mix with the neutral (charged) electroweak gauginos to form mass eigenstates called neutralinos  $\tilde{\chi}_i^0$  (charginos  $\tilde{\chi}_j^\pm$ ) with  $i \in \{1, 2, 3, 4\}$  ( $j \in \{1, 2\}$ ). The indices rank the mass eigenstates from light to heavy. Conservation of color prevents gluinos, the superpartners of the gluons, from mixing with higgsinos and the other gauginos, although they can acquire mass via the SUSY breaking mechanism, discussed in Section 2.2.3. All sfermions with the same electric charge and color can mix with each other to form mass eigenstates, e. g.  $\tilde{t}_L$  and  $\tilde{t}_R$  will form the two massive states  $\tilde{t}_1$  and  $\tilde{t}_2$ . Depending on the details of the SUSY breaking mechanism, they usually have different masses, i. e.  $m(\tilde{t}_1) < m(\tilde{t}_2)$ . In order to provide a natural solution to the fine-tuning problem, sfermions of the third generation are expected to be the lightest and might therefore be accessible at collider experiments [1, 35].

As mentioned before, gravity can be included into the MSSM by making the SUSY generator local. The gravitino, the hypothesized massless, spin-2 mediator of gravity, together with its spin- $3/2$  superpartner, the gravitino, are then assembled in a gravity supermultiplet. While the massless graviton and gravitino each have two helicity states in an unbroken theory of SUSY, the gravitino can acquire mass and thus two additional longitudinal polarizations if the symmetry is spontaneously broken. The necessity and implications of a broken SUSY are discussed in Section 2.2.3.

### 2.2.2 $R$ -Parity

In SM processes baryon number  $B$  and lepton number  $L$  are conserved. Within the SM the proton, being the lightest baryon, is thus stable. This prediction is in agreement with experiments searching for proton decay with the Super-Kamiokande detector which set lower limits on the proton lifetime at  $\mathcal{O}(10^{34})$  years [36].

By introducing SUSY, new interaction vertices can occur which would allow for the proton to decay. To guarantee baryon and lepton number conservation within the MSSM the conservation of a new multiplicative quantum number, called  $R$ -parity [37], is introduced:

$$R = (-1)^{3(B-L)+2S} = \begin{cases} +1 & \text{for SM particles,} \\ -1 & \text{for SUSY particles,} \end{cases} \quad (2.11)$$

where  $S$  is the spin and  $B = \frac{1}{3}(N_q - N_{\bar{q}})$ , with  $N_q$  ( $N_{\bar{q}}$ ) the number of (anti-)quarks or (anti-)squarks, and  $L = N_\ell - N_{\bar{\ell}}$ , with  $N_\ell$  ( $N_{\bar{\ell}}$ ) the number of (anti-)leptons or (anti-)sleptons.

The MSSM is defined to conserve  $R$ -parity. This has a series of phenomenological implications:

- At collider experiments, sparticles can only be produced in even numbers.
- A sparticle can only decay into an odd number of sparticles. Consequently, the

lightest supersymmetric particle (LSP) is stable.

- The LSP has to be electrically uncharged and colorless to be compatible with astrophysical data [38, 39]. A massive LSP would be a suitable candidate for dark matter.
- Due to these properties, the LSP cannot be detected directly in a collision experiment. Its presence can be inferred indirectly via the momentum imbalance of all observable final state particles.

SUSY models with  $R$ -parity violation are viable if the interactions that violate  $B - L$  conservation have small couplings and violate only  $B$  or  $L$  at tree level but not both simultaneously, thus preventing rapid proton decay [40, 41].

### 2.2.3 Symmetry breaking

From observations it is clear that the SM particles are not degenerate with their superpartners, and therefore SUSY must be a broken symmetry. To preserve its features SUSY must be spontaneously broken, rather than explicitly, meaning that the underlying Lagrangian density is supersymmetric but the vacuum state is not [15]. In addition the breaking is desired to be ‘soft’, which means that it should not spoil the renormalizability of the theory. A consequence of spontaneous SUSY breaking is the existence of a massless Goldstone fermion, the goldstino, which is absorbed by the gravitino if SUSY is defined to be local. The gravitino then becomes massive with two transverse (helicity  $\pm 3/2$ ) and two longitudinal (helicity  $\pm 1/2$ ) modes. Moreover, it inherits the non-gravitational interactions of the goldstino and thus the longitudinal modes of the gravitino can be of relevance in collider experiments [14].

Several models exist that describe the mechanisms of SUSY breaking. In these models, the breaking occurs in a hidden sector, and the effect is propagated to the visible sector of the MSSM via messenger fields. Depending on the implementation, the scale at which the breaking occurs varies and different LSPs are predicted. For instance, in models with gravity-mediated SUSY breaking the lightest neutralino,  $\tilde{\chi}_1^0$ , is usually the LSP [14, 15].

The scenario studied in this thesis is based on local SUSY and assumes a gauge-mediated symmetry breaking (GMSB) mechanism [42–44]. Here, the messenger fields that mediate the SUSY breaking effects have SM gauge couplings. Compared to gravity-mediated breaking, the breaking scale is significantly lower, which leads to a light gravitino  $\tilde{G}$ , which is often assumed to be the LSP in such models and hence also a good dark matter candidate [14]. At tree level, SUSY is unbroken in the MSSM sector but sparticles receive radiative corrections to their mass via their coupling to the messenger fields in loops [14]. Therefore, due to their additional loop contributions, colored sparticles are heavier than uncolored ones and, likewise, uncolored sparticles that have only hypercharge gauge interactions are lighter than those which also couple to  $SU(2)_L$ . In GMSB models, the next-to-lightest supersymmetric particle (NLSP) is

often given by the light mass eigenstate of the tau-lepton superpartner  $\tilde{\tau}_1$  [14]. The relatively strong coupling to the Goldstino, incorporated in the spin- $1/2$  component of the gravitino, leads to a short-lived tau slepton [45, 46].

## 2.3 Leptoquarks

Leptoquarks are defined as color-triplet bosons carrying both lepton and baryon number, and can have a spin of 0 or 1. They are charged under all SM gauge groups and thus couple to both a quark and a lepton, enabling direct transitions between the two. Leptoquarks are proposed by a variety of beyond-SM theories briefly touched upon in the following. Many of their characteristics, such as their spin or electric charge, are model-independent and their phenomenology can be described using effective models.

### 2.3.1 Motivation

Because of their colour charge and weak isospin, leptoquarks can give rise to flavor-changing neutral currents, and enable the violation of lepton flavor universality. Therefore, they can explain the anomalies observed in measurements of  $B$ -meson decays [47–53], discussed in Section 2.1.2. Theories involving leptoquarks might also be able to resolve other open questions of the SM. For instance, leptoquarks can explain the origins of neutrino masses [54–57]. Furthermore, they can give rise to sources of CP violation, thereby explaining the observed matter/antimatter asymmetry in the universe [58, 59]. Leptoquarks can also give a satisfying connection between the apparent symmetry of the quark- and lepton-sector in the SM [60].

Such leptoquark states arise in several theories describing physics beyond the SM. In the following, a list of the most prominent ones is compiled. It is worth noting that these theories do not necessarily mutually exclude each other.

**Supersymmetry:** Several viable models exist in which the  $R$ -parity conservation introduced for the MSSM in Section 2.2.2 can be violated to a certain extent [40, 41]. The scalar superpartners of fermions in such models can feature leptoquark-like decays through Yukawa couplings in addition to their normal decay modes through gauge couplings.

**Pati-Salam model:** In its most basic form, the Pati-Salam model proposes that quarks carry an additional fourth color that represents the lepton number [61]. Thereby, the  $SU(3)_C$  gauge group of the SM is extended, leading to a unification of baryonic and leptonic matter in a global structure of the form  $SU(4) \times SU(2)_L \times SU(2)_R$ . This model predicts the existence of gauge bosons carrying both lepton and baryon number which can be identified as leptoquarks.

**Grand Unified theories:** In GUTs, all known SM interactions are embedded in one gauge group with a single coupling constant. GUTs based on  $SO(10)$  [62, 63],  $SU(5)$  [60] and  $E_6$  [64] imply the existence of leptoquark states. This larger single gauge symmetry is broken at the lower energy scales reached in today’s collider experiments, resulting in the known SM group structure. The gauge group of the Pati-Salam model, for example, represents the maximal subgroup of supersymmetric  $SO(10)$  GUTs [65].

**Quark and lepton compositeness:** Models postulating that SM fermions are made of constituents, so-called preons, can give rise to either new bound states or Goldstone bosons with leptoquark properties [66, 67].

**Technicolor:** In extended models of technicolor, which describe a dynamic mechanism of electroweak symmetry breaking, scalar leptoquarks appear as the bound states of technifermions [68, 69].

### 2.3.2 Phenomenology

Effective models, which are independent of the beyond-SM theories predicting leptoquarks, can be employed in a search at collider experiments. Experimental constraints impose limits on the nature of leptoquarks. The Buchmüller-Rückl-Wyler (BRW) model is a general effective leptoquark model [70]. It requires leptoquarks to only couple to SM fermions and gauge bosons and have renormalizable interactions, invariant under the SM gauge transformations. Furthermore, in order for the leptoquark to be sufficiently light to be relevant for searches at colliders and preserve the stability of the proton, the lepton and baryon number must be conserved independently in leptoquark interactions. Such leptoquarks carry a fermionic number

$$F = 3B + L \tag{2.12}$$

with an absolute value of either 2 or 0. Table 2.1 lists the resulting seven scalar leptoquarks in the BRW model, along with their electric charge  $Q$ , weak isospin  $T_3$  and decay products. The subscripts denote the chirality  $L/R$  of the coupled lepton and whether the leptoquark is singlet (1), doublet (2) or triplet (3) under  $SU(2)_L$ , respectively. Mass-degeneracy is assumed for experimental searches. The equivalent set of seven vector leptoquarks (spin 1) is not of immediate relevance to the search presented in this thesis and therefore not discussed here. Instead, a description can be found in Refs. [70, 71]. Except for a GUT based on  $SU(15)$ , only a subset of the 14 leptoquarks described by the BRW model generally appear in the more specific models discussed in the previous Section 2.3.1.

Further constraints, motivated by observations from low-energy experiments, are imposed in the *minimal* BRW model [72] to ensure sufficiently light leptoquarks: Leptoquarks are defined to be ‘diagonal’, meaning they can only couple to quarks and leptons of the same generation. Inter-generational couplings are forbidden as they would give

|           | Leptoquark       | $Q$  | $T_3$  | Couplings   | $\beta$   |       |
|-----------|------------------|--|--------|---|---|-------|
| $ F  = 2$ | $S_{1L}$         | $1/3$  | $0$    | $\lambda_L(\ell^+\bar{u}), \lambda_L(\bar{\nu}\bar{d})$ | $1/2$   |       |
|           | $S_{1R}$         | $1/3$  | $0$    | $\lambda_R(\ell^+\bar{u})$                              | $1$   |       |
|           | $\tilde{S}_{1R}$ | $4/3$  | $+1$   | $\lambda_R(\ell^+\bar{d})$                              | $1$   |       |
|           | $S_{3L}$         | $\left\{ \begin{array}{ll} 4/3 & +1 \\ 1/3 & 0 \\ -2/3 & -1 \end{array} \right.$ | $4/3$  | $+1$  | $-\sqrt{2}\lambda_L(\ell^+\bar{d})$                       | $1$   |
|           |                  |  | $1/3$  | $0$   | $-\lambda_L(\ell^+\bar{u}), -\lambda_L(\bar{\nu}\bar{d})$ | $1/2$ |
|           |                  | $-2/3$   | $-1$   | $\sqrt{2}\lambda_L(\bar{\nu}\bar{d})$                   | $0$   |       |
| $ F  = 0$ | $R_{2L}$         | $\left\{ \begin{array}{ll} 5/3 & +1/2 \\ 2/3 & -1/2 \end{array} \right.$         | $5/3$  | $+1/2$  | $\lambda_L(\ell^+u)$                                      | $1$   |
|           |                  |  | $2/3$  | $-1/2$  | $\lambda_L(\bar{\nu}u)$                                   | $0$   |
|           | $R_{2R}$         | $\left\{ \begin{array}{ll} 5/3 & +1/2 \\ 2/3 & -1/2 \end{array} \right.$         | $5/3$  | $+1/2$  | $\lambda_R(\ell^+u)$                                      | $1$   |
|           |                  |  | $2/3$  | $-1/2$  | $-\lambda_R(\ell^+d)$                                     | $0$   |
|           | $\tilde{R}_{2L}$ | $\left\{ \begin{array}{ll} 2/3 & +1/2 \\ -1/3 & -1/2 \end{array} \right.$        | $2/3$  | $+1/2$  | $\lambda_L(\ell^+d)$                                      | $1$   |
|           |                  |  | $-1/3$ | $-1/2$  | $\lambda_L(\bar{\nu}d)$                                   | $0$   |

**Table 2.1:** Scalar leptoquark states together with their electric charge  $Q$  (in unit of  $e$ ), weak isospin  $T_3$  and couplings. Here,  $\beta$  denotes the branching ratio into charged leptons assuming massless decay products. The coupling constants  $\lambda_{L/R}$  describe the strength of the Yukawa coupling to left/right-handed fermions (usually also given in units of  $e$ ). The leptoquark indices are described in the text. No distinction is made between the representation and its conjugate. Table adapted from Ref. [71].

rise to flavor changing neutral currents and violate flavor universality at tree-level. Measurements of the helicity-suppressed  $\pi \rightarrow e\nu_e$  decay rate as well as the anomalous magnetic moment of the muon require a purely chiral coupling of the leptoquark. This means that leptoquarks couple only to either left- or right-handed fermions. However, depending on the details of the considered model, it is possible to relax some of the imposed constraints.

## 2.4 Simplified models

Predictive theories describing possible beyond-SM physics depend on a series of free parameters. Their values are not fixed by first principles and require experimental input as long as a more fundamental theory is not yet available. In order to efficiently analyze the immense datasets recorded at collider experiments simplified models are designed to involve only a small number of new particles and interactions [73–75]. By fixing many of the free parameters to phenomenologically motivated values the analysis of the data focuses only on certain kinematics, such as certain decay modes of the hypothesized new particles. This way, the parameter space of a wide framework such as the MSSM can be tested by multiple dedicated searches in parallel. If one of the searches observes an excess above the SM prediction, the simplified model used to

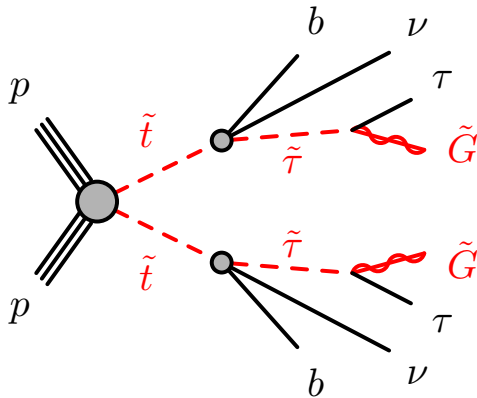


**Figure 2.4:** Diagram illustrating the pair-production of top squarks and their subsequent decay chain considered in the simplified models of the supersymmetric scenario. The tau slepton produced in the three-body decay of the top-squark decays into a SM tau lepton and a gravitino. The branching fractions of both decays are assumed to be 100 %.

design the analysis would then serve as a stepping stone to perform a more general search. Thus simplified model are to be understood as part of a broad effort to identify events associated to possible new physics.

In the following, two simplified signal models are introduced. One considers a SUSY benchmark scenario, the other involves leptoquarks. Due to their similar final states, an analysis with high sensitivity to both models can be designed.

### 2.4.1 Pair production of top squarks decaying via tau sleptons

The primary signal scenario studied in this thesis is based on the MSSM and is motivated by GMSB. This  $R$ -parity conserving signal model features natural gauge mediation [1], specifically targeting the fine-tuning problem described in Section 2.1.2. It requires that the superpartners of the third generation SM fermions are sufficiently light to allow for a natural stabilization of the Higgs mass [76, 77].

Only three sparticles are assumed to be sufficiently light to be relevant: the lighter top squark  $\tilde{t}_1$ , the lighter tau slepton  $\tilde{\tau}_1$  and the gravitino  $\tilde{G}$ . The top squark is assumed to be the lightest squark and directly pair-produced via the strong interaction in  $pp$ -collisions at a center-of-mass-energy of  $\sqrt{s} = 13$  TeV. The gravitino is assumed to be nearly massless, making it the LSP in this  $R$ -parity conserving scenario. The varied parameters of this signal model are the sfermion masses,  $m(\tilde{t}_1)$  and  $m(\tilde{\tau}_1)$ . The top-squark pair-production and subsequent decay chain is illustrated in Figure 2.4. First, the top squark decays into a  $b$ -quark, a tau neutrino and a tau slepton which is the NLSP in this model. The latter then decays into a tau lepton and the LSP. The branching ratios for both of these decays are fixed to 100 %. The three-body decay can

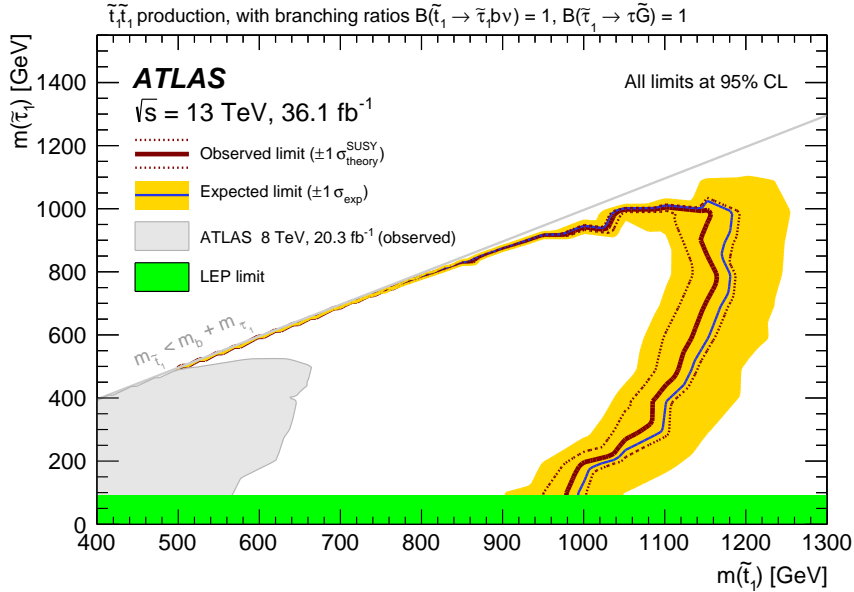


**Figure 2.5:** Limits on  $m(\tilde{t}_1)$  and  $m(\tilde{\tau}_1)$  for pair production of top-squarks decaying via tau sleptons set by ATLAS using an integrated luminosity of  $36.1 \text{ fb}^{-1}$ . The green band indicates the limit on the tau slepton mass from the LEP experiments [81]. Figure adapted from Ref. [82].

be imagined as proceeding through an off-shell chargino,  $\tilde{t}_1 \rightarrow b\tilde{\chi}_1^\pm$  with  $\tilde{\chi}_1^\pm \rightarrow \tilde{\tau}_1\nu_\tau$ . The tau leptons are assumed to be unpolarized, i. e. no assumption is made on chargino and stau-mixing. Direct top-squark decays into the gravitino LSP and a SM particle are suppressed due to its weak coupling, except for the NLSP.

Throughout this thesis, the short-hand term *stop-stau* signal is used to refer to this simplified SUSY benchmark model. SUSY models with gravity-mediated instead of gauge-mediated symmetry breaking and the neutralino as LSP would suggest a high branching ratio of  $\tilde{t}_1 \rightarrow t\tilde{\chi}_1^0$ , which has been studied elsewhere [78–80].

A search for the stop-stau signal has been conducted by ATLAS first using  $20 \text{ fb}^{-1}$  of  $\sqrt{s} = 8 \text{ TeV}$  data taken in Run 1 [83] and again using  $36.1 \text{ fb}^{-1}$  of  $\sqrt{s} = 13 \text{ TeV}$  data taken in Run 2 of the LHC [82]. No significant excess over the SM prediction was observed in either iteration and thus limits were set on the masses of the top squark and tau slepton in the context of this simplified model. The limits, shown in Figure 2.5, exclude top-squark masses of up to 1.15 TeV and tau-slepton masses up to 1.0 TeV at 95% confidence level. The analysis was conducted as search in two complementary final states, depending on the decay mode of the tau lepton. Overall, the had-had channel, which assumes both tau leptons decay hadronically, showed superior performance across the  $m(\tilde{t}_1) - m(\tilde{\tau}_1)$  parameter-space when compared to the lep-had channel, which assumes one of the tau leptons to decay leptonically instead [84]. Final states where both tau leptons decay leptonically were not considered in the previous iteration due

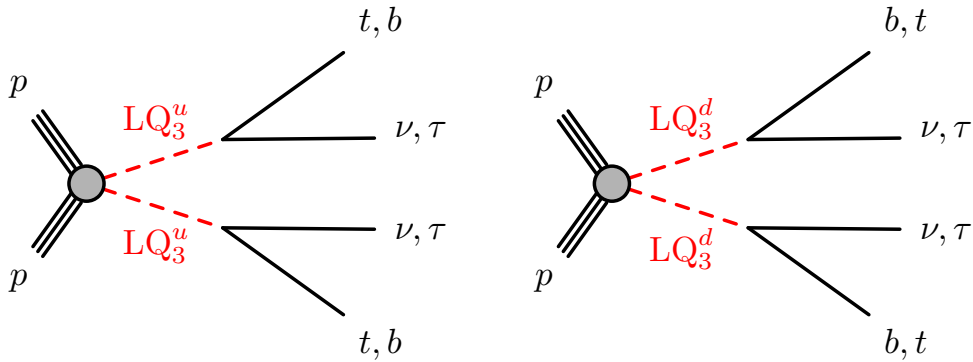


**Figure 2.6:** Diagram illustrating the pair-production of up- or down-type scalar leptoquarks and their subsequent decays into third-generation quark-leptons pairs. Depending on their coupling  $\beta$  to charged leptons, different decays are considered. In the following, this simplified model is referred to as the  $LQ_3^{u/d}$  signal.

to the lower branching ratio  $B(\tau \rightarrow \nu_\tau \ell \bar{\nu}_\ell) \sim 35\%$ . The LEP experiment has set limits on the tau-slepton mass at around 90 GeV from searches for direct pair-production of tau sleptons in  $e^+e^-$  collisions [81]. A search for top-squark pair production in final states with tau leptons has also been conducted by CMS on  $77.2\text{fb}^{-1}$  of data using a simplified model with a neutralino as the LSP, in which top-squark masses up to 1.1 TeV are excluded for a nearly massless neutralino [85].

### 2.4.2 Pair production of third-generation scalar leptoquarks

The second signal model considered in this thesis involves pair-production of scalar leptoquarks of the third generation following the minimal BRW model introduced in Section 2.3.2, with the exception that  $\beta \in [0, 1]$  is assumed to be a free parameter, which allows for a more general investigation. Leptoquarks are assumed to decay into a quark-lepton pair of the third generation only. Both up- and down-type leptoquarks with a fractional electric charge of  $2/3e$  and  $-1/3e$ , respectively, are considered. In the following, they are abbreviated with  $LQ_3^{u/d}$ .

The modelling of the production process is described in Ref. [86], where the coupling to right-handed charged leptons is set to zero since the analysis is not sensitive to the chiral coupling fractions of the leptoquark. The Yukawa couplings of leptoquarks to the quark-lepton pair are then determined by two parameters: a common coupling strength  $\lambda$  and the parameter  $\beta$  that defines the strength of the coupling to a charged lepton. The coupling to the tau lepton is given by  $\lambda\sqrt{\beta}$ , and the coupling to the tau neutrino by  $\lambda\sqrt{1-\beta}$ . Figure 2.6 illustrates the production and decays of  $LQ_3^{u/d}$ -pairs. The search is carried out for both up-type ( $LQ_3^u \rightarrow t\nu_\tau/b\tau$ ) and down-type ( $LQ_3^d \rightarrow b\nu_\tau/t\tau$ ) leptoquark pairs with varying mass  $m(LQ_3^{u/d})$ . The analysis primarily focusses on intermediate values of  $\beta$  and other values are studied elsewhere [78, 87, 88].

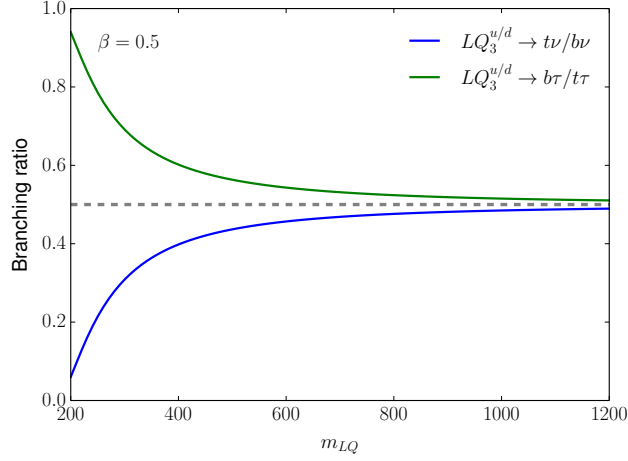


**Figure 2.7:** Branching ratio of  $LQ_3^{u/d}$  into charged or uncharged leptons with respect to  $m_{LQ}$  and using  $\beta = 0.5$ .

Due to the high mass of the top quark, the actual branching ratio of the leptoquark to a charged lepton  $B_{cl}$  is not identical to  $\beta$  but slightly skewed depending on  $m(LQ_3^{u/d})$  as illustrated in Figure 2.7. For increasing leptoquark masses,  $B_{cl}$  asymptotically approaches  $\beta = 0.5$ . The dependence of the  $LQ_3^{u/d}$  decay width on  $\lambda$ ,  $\beta$  and the masses of the daughter particles is given in Equations (2.13) to (2.16) [89].

$$\Gamma(LQ_3^u \rightarrow t\nu_\tau) = \frac{(m(LQ_3^u)^2 - m(t)^2)^2 3\lambda^2 (1 - \beta)}{48\pi m_{LQ}^3} \quad (2.13)$$

$$\begin{aligned} \Gamma(LQ_3^u \rightarrow b\tau) &= \frac{(m(LQ_3^u)^2 - m(b)^2 - m(\tau)^2)^2 3\lambda^2 \beta}{48\pi m_{LQ}^3} \\ &\times \sqrt{m(LQ_3^u)^4 + m(b)^4 + m(\tau)^4 - 2(m(LQ_3^u)^2 m(b)^2 + m(LQ_3^u)^2 m(\tau)^2 + m(b)^2 m(\tau)^2)} \end{aligned} \quad (2.14)$$

$$\Gamma(LQ_3^d \rightarrow b\nu_\tau) = \frac{(m(LQ_3^d)^2 - m(b)^2)^2 3\lambda^2 (1 - \beta)}{48\pi m_{LQ}^3} \quad (2.15)$$

$$\begin{aligned} \Gamma(LQ_3^d \rightarrow t\tau) &= \frac{(m(LQ_3^d)^2 - m(t)^2 - m(\tau)^2)^2 3\lambda^2 \beta}{48\pi m_{LQ}^3} \\ &\times \sqrt{m(LQ_3^d)^4 + m(t)^4 + m(\tau)^4 - 2(m(LQ_3^d)^2 m(t)^2 + m(LQ_3^d)^2 m(\tau)^2 + m(t)^2 m(\tau)^2)} \end{aligned} \quad (2.16)$$

In the considered model, the value of  $\lambda$  is set to 0.3, which results in a decay width of about 0.2% of its mass and corresponds to a interaction strength of the same order as

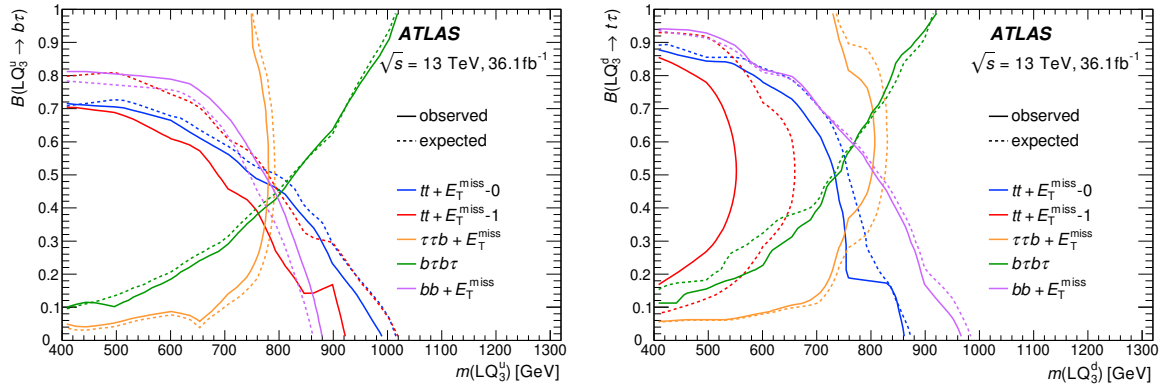


**Figure 2.8:** Limits on  $m(\text{LQ}_3^{\text{u/d}})$  and the branching ratio into charged leptons for pair production of scalar third-generation up-/down-type leptoquarks set by ATLAS using an integrated luminosity of  $36.1 \text{ fb}^{-1}$ . The orange exclusion contours are derived from a reinterpretation of the stop-stau search using  $36.1 \text{ fb}^{-1}$  [82]. Figures adapted from Ref. [92].

electromagnetic interactions [70, 90]. For such a value of  $\lambda$ , contributions to the total production cross-sections from lepton-mediated  $t$ -channel processes are negligible, in particular for third-generation leptoquarks as this mode would require third-generation quarks in the initial state [91]. The dominant production modes are thus  $gg$  fusion and  $q\bar{q}$  annihilation.

The model is identical to the one used for the search for scalar first- and second-generation leptoquarks with ATLAS [93]. A previous ATLAS publication [92] summarizing searches for third-generation leptoquarks used  $36.1 \text{ fb}^{-1}$  of data taken at  $\sqrt{s} = 13 \text{ TeV}$ . It comprises a dedicated reoptimization of the ATLAS search for di-higgs production as well as four reinterpretations of ATLAS searches for SUSY, targeting different values of  $B_{\text{cl}}$ . This includes a reinterpretation of the previous iteration of the stop-stau search [82]. As no excess in data over the background expectation was observed by any of the searches, individual exclusion limits have been set on the signal parameters as summarized in Figure 2.8: Limits on the  $\text{LQ}_3^{\text{u/d}}$  mass are close to 850 GeV for  $B_{\text{cl}} \sim 0.5$  and reach up to  $\sim 1 \text{ TeV}$  for minimal and maximal  $B_{\text{cl}}$ . The exclusion contours from the reinterpreted  $36.1 \text{ fb}^{-1}$  stop-stau search are shown in orange, which is most sensitive to intermediate values of the branching ratio. The newly developed search strategy described in this thesis targets even higher leptoquark masses and again  $B_{\text{cl}} \sim 0.5$ . Smaller or larger values of  $B_{\text{cl}}$  are covered by other dedicated searches or reinterpretations of existing results based on the full Run 2 dataset [78, 87, 88]. This shared effort can also be seen in Figure 2.8. A search in a final state consisting of two tau leptons and two  $b$ -quarks has high sensitivity to  $B_{\text{cl}} \sim 1$ , while the  $B_{\text{cl}} \sim 0$  regime can for example be covered by a search in final states with two  $b$ -quarks and missing transverse momentum in the event which originates from the detector-invisible neutrinos. Note that the top-quark decay will virtually always yield a  $b$ -quark.

# 3 Experimental Setup

The proton–proton ( $pp$ ) collision events analyzed in this thesis have been produced by the Large Hadron Collider (LHC) and recorded with the ATLAS detector. This section gives an overview of the design and working principles of the accelerator complex and the main detector elements of the ATLAS experiment.

## 3.1 The Large Hadron Collider

The LHC [94] is a circular accelerator designed to collide two beams of hadrons at four designated interaction points. It is located near Geneva, Switzerland, below ground and is designed and operated by the European Organization for Nuclear Research (CERN). With about 27 km in circumference it is the largest particle accelerator in the world. It is capable of accelerating protons as well as heavy ions. The infrastructure previously hosted the LEP collider from 1989 through 2000. The LHC started nominal operation in 2010. In its first data-taking phase, Run 1, protons were collided with a center-of-mass energy of  $\sqrt{s} = 7$  TeV until 2011 and 8 TeV in 2012. After a maintenance and upgrade shut down, Run 2 started in 2015 with  $\sqrt{s} = 13$  TeV and ended in 2018.

Figure 3.1 shows a schematic overview of the CERN accelerator chain and the various experiments. Protons are produced by ionizing hydrogen atoms and are then accelerated in several steps before being injected in bunches into the evacuated beam pipes of the LHC [96]. In a first step, the protons are accelerated up to 50 MeV by the linear accelerator LINAC-2. From there they are injected into the Proton Synchrotron Booster (PSB) where the protons are gathered in bunches and accelerated to 1.4 GeV. They are then sent to the Proton Synchrotron (PS) where they eventually reach an energy of 25 GeV. The energy of the protons is further increased to 450 GeV by the Super Proton Synchrotron (SPS) before they are injected into the LHC ring as clockwise or counter-clockwise beams where they reach their current maximum of 6.5 TeV [97]. Superconducting dipole magnets, generating field strengths of up to 8.3 T, force the protons onto nearly circular orbits.

The beams are focused and brought to collision at four interaction points (IPs), where the four major detectors ATLAS [98], ALICE [99], CMS [100] and LHCb [101] record the collisions. The up to 2808 bunches per beam consist of  $\mathcal{O}(10^{11})$  protons each and have a minimum bunch spacing of 25 ns, leading to about 40 million bunch crossings per second at the four IPs [102]. The actual number of  $pp$  interactions per second

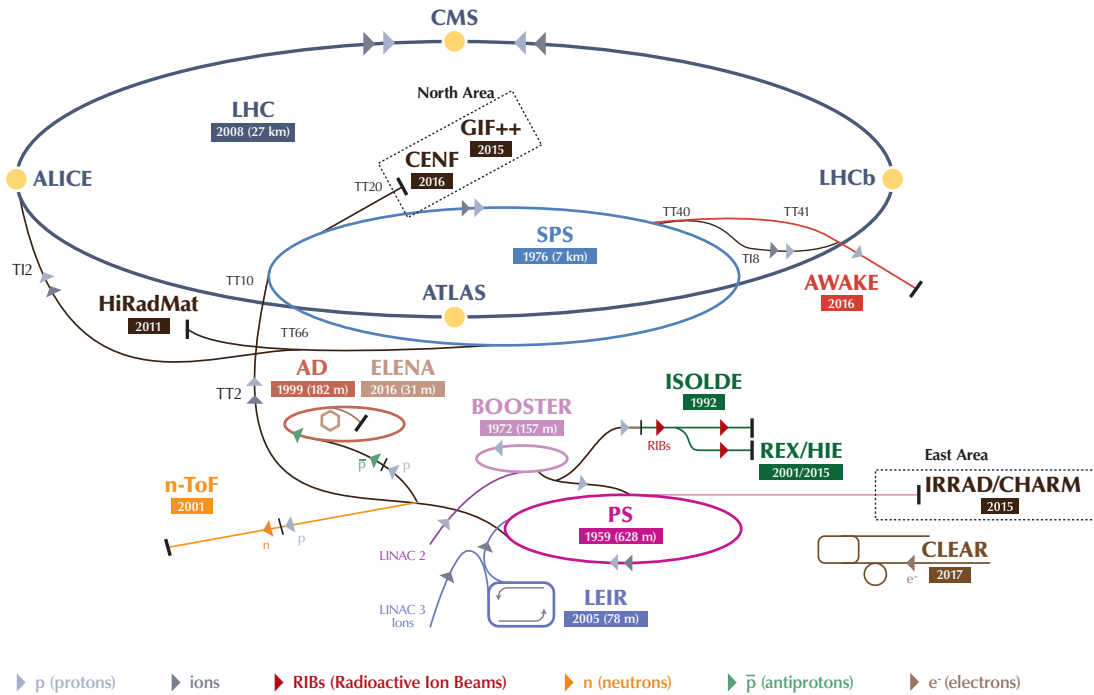


**Figure 3.1:** Schematic illustration of the CERN accelerator complex. Figure adapted from Ref. [95].

depends on the number of collisions per bunch crossing, referred to as *pile-up*, which will be discussed in Section 3.2.4.

## 3.2 The ATLAS Experiment

The ATLAS detector is a general-purpose particle detector designed to measure and identify the particles produced in the  $pp$  interactions. A full description of the detector design is given in Ref. [102], which is briefly reviewed in the following.

Its central element, called barrel region, consists of multiple layers of complementary subsystems concentrically arranged around the beam axis. Each side of the cylindrical volume is covered by a similar sequence of subdetectors arranged in discs orthogonal to the beam axis. These so-called end-caps are used to detect and track particles scattered in the forward or backward direction. In total the ATLAS detector measures 44 m in length and 25 m in diameter.

A schematic view of the detector is shown in Figure 3.2. The various subsystems used for particle reconstruction and identification are discussed in Section 3.2.2.

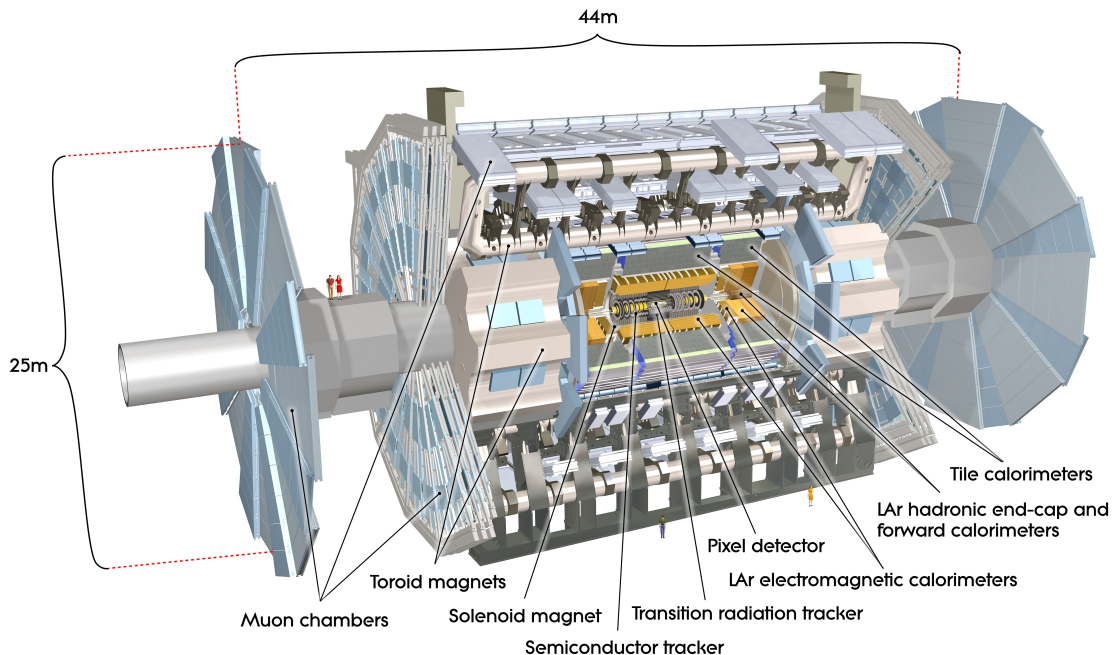


**Figure 3.2:** Schematic layout of the ATLAS detector. The front part of the barrel is removed to show the interior structure. Figure adapted from Ref. [103].

### 3.2.1 Coordinate system

A right-handed Cartesian coordinate system is used to describe the detector layout and reconstructed objects produced in the collisions. The origin is located at the nominal IP at the center of the detector. The  $z$ -axis points along the beam direction, the  $y$ -axis upwards towards the surface and the  $x$ -axis towards the center of the LHC ring. The azimuthal angle  $\phi$  is measured in the  $x$ - $y$  or *transverse* plane relative to the positive  $x$ -axis and the polar angle  $\theta$  is measured from the positive  $z$ -axis. As the momentum fractions carried by the interacting partons in the  $pp$  collisions are unknown, so are the longitudinal boosts of the final state particles with respect to the center-of-mass system. Many observables, such as the energy or momentum, are therefore projected on the transverse plane, which is indicated by the subscript ‘T’. Particles, which escape detection, such as neutrinos, manifest in a non-zero net transverse momentum, referred to as missing transverse momentum  $\mathbf{E}_T^{\text{miss}}$ . Its absolute value is denoted as  $E_T^{\text{miss}}$ .

The rapidity of a particle with energy  $E$  and longitudinal momentum  $p_z$  is defined as

$$y = \frac{1}{2} \ln \frac{E + p_z}{E - p_z}. \quad (3.1)$$

As an alternative to  $\theta$ , it is preferred due to its Lorentz invariance with respect to boosts in  $z$ -direction. In the ultrarelativistic limit ( $E \gg m$ ) an equivalent description

is given by the pseudorapidity

$$\eta = -\ln(\tan \theta/2) \quad (3.2)$$

which has the advantage of being independent of the energy and momentum calibration of the reconstructed objects. The Lorentz invariant angular separation of two objects is defined as

$$\Delta R = \sqrt{\Delta\eta^2 + \Delta\phi^2}, \quad (3.3)$$

assuming they originate from the same point in space. The impact parameters  $d_0$  and  $z_0$  refer to the distance to a point, e.g. to the IP or a reconstructed vertex, in the transverse and longitudinal direction, respectively.

### 3.2.2 Detector components

The various subsystems of the ATLAS detector can be grouped into three major elements: The Inner Detector (ID), the calorimeters and the Muon Spectrometer (MS), sorted by increasing distance from the IP. Additionally, there are forward detectors located along the beam pipe further away from the IP. They are primarily used to measure the instantaneous luminosity which is discussed in Section 3.2.4.

In the following, the layout and working principle of the main detector subsystems as described in Refs. [102, 104, 105] are summarized. The order of discussion follows the path of a particle emerging from the IP, i.e. going from the inside of the ATLAS detector to the outside.

#### Inner Detector

The ID is the first subsystem traversed by the particles produced in the  $pp$  collisions. It is designed to enable the reconstruction of charged-particle trajectories with high precision by measuring hits in three-dimensional space. The reconstructed tracks can then be extrapolated inwards, to reconstruct production and decay vertices within the beam pipe, or outwards, to associate tracks with measurements in the subsequent detector systems. The ID is surrounded by a thin superconducting solenoid magnet, embedding it in a magnetic field of 2 T oriented parallel to the  $z$ -axis. The tracks of charged particles are bent due to the Lorentz force and a measurement of the curvature allows for a precise reconstruction of the particle's momentum, while the direction of the curvature is determined by the sign of the charge. Three different technologies are employed and a schematic overview is shown in Figure 3.3.

The beam pipe is surrounded by four layers of silicon pixel detectors. The innermost is called the Insertable B-Layer (IBL) and was added before the start of Run 2 [106], improving the tracking and vertex reconstruction [107]. Three disc layers are located in

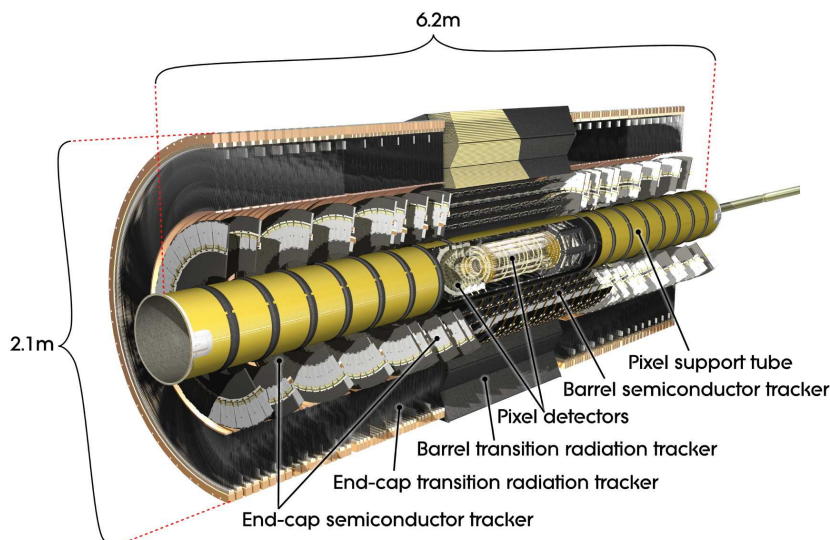


**Figure 3.3:** Schematic view of the Inner Detector and its components. Figure adapted from Ref. [102].

each of the end-caps. In total, the pixel detector has an accuracy of  $10\ \mu\text{m}$  and  $115\ \mu\text{m}$  in the transverse plane and longitudinal direction, respectively [102].

The pixel detector is surrounded by the Semiconductor Tracker (SCT). Together they cover an absolute pseudorapidity range of  $|\eta| < 2.5$ . It consists of four cylindrical layers in the barrel and nine discs in each end-cap. They each consist of two silicon microstrip sensors glued together back to back and slightly twisted with respect to each other by a small angle of  $40\ \text{mrad}$ , resulting in a longitudinal resolution of  $580\ \mu\text{m}$ . In the transverse plane, the SCT has an accuracy of  $17\ \mu\text{m}$ .

The next subsystem traversed by outgoing particles is the Transition Radiation Tracker (TRT). It consists of  $4\ \text{mm}$  wide straw drift tubes filled with a xenon-based gas mixture and a gold-plated tungsten anode wire in the center. They are aligned parallel to the beam pipe in the barrel region and radially in the end-caps, providing a total coverage of  $|\eta| < 2.0$ . The tubes are interleaved with a radiator material which facilitates the creation of transition radiation by traversing charged particles and is used for the identification of electrons. The relatively low resolution of  $120\ \mu\text{m}$  in the transverse plane is compensated by a large number of hits per track ( $\gtrsim 30$ ) and the long lever arm due to the distance from the IP [108].

## Calorimeters

After passing through the ID, emerging particles enter the calorimeters. They are designed to absorb most particles and measure their deposited energy. Two different types of calorimetric systems are discriminated: An inner electromagnetic (EM) calorimeter

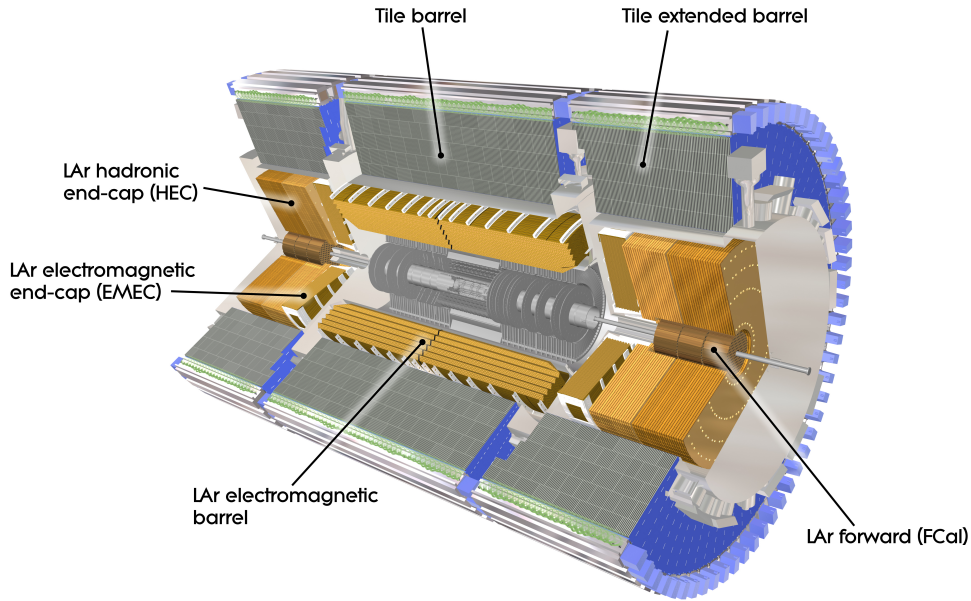


**Figure 3.4:** Schematic view of the calorimeter system. Figure adapted from Ref. [109].

absorbs most of the electrons, positrons and photons and an outer hadronic calorimeter is designed to stop hadrons. Both are sampling calorimeters, i. e. they consist of alternating layers of absorber and scintillating material. In absorber layers, particles lose a portion of their energy and produce showers of secondary particles. The intensity and shape of the showers is measured in the scintillating layers from which the energy loss of the primary particle is inferred. Neutrinos and sufficiently energetic muons are the only SM particles expected to pass through the calorimeters. A schematic view of the calorimeters is shown in Figure 3.4.

In the EM calorimeter, the alternating layers of lead absorber plates and liquid argon (LAr), serving as active medium, are arranged in an accordion shape, allowing for a uniform coverage in  $\phi$  without cracks. The EM calorimeter is divided into concentric layers with radially decreasing  $\Delta\eta \times \Delta\phi$  granularity. The inner two layers have the finest segmentation, in particular in the range  $|\eta| < 2.5$ . The second layer where most of the energy is typically deposited has a granularity of  $0.025 \times 0.025$  (for  $|\eta| < 1.4$ ). The barrel part of the EM calorimeter covers the range  $|\eta| < 1.475$ , while the two end-caps extend the range to  $|\eta| < 3.2$ . An additional LAr layer, called the presampler, is located in the range  $|\eta| < 1.8$  in front of the innermost layer, allowing for corrections for the energy loss in the upstream detector material. Due to the additional passive material in the transition region between barrel and end-cap cryostats, the energy resolution is significantly degraded in the range  $1.37 < |\eta| < 1.52$ . It is therefore often excluded for particles relying on precise calorimeter measurements.

The hadronic calorimeter in the barrel region consists of alternating layers of steel

absorber plates and scintillating tiles oriented perpendicular to the beam axis. It is segmented in a central barrel part and two extended barrels next to it, covering in total the range  $|\eta| < 1.7$ . Each barrel part consists of three radial layers and 64 wedges in  $\phi$ . Segments have a typical cell size of  $\Delta\eta \times \Delta\phi = 0.1 \times 0.1$  in the first two layers and  $0.2 \times 0.1$  in the last layer. The hadronic calorimetry is extended to  $|\eta| < 3.2$  by a LAr calorimeter using copper plates as absorber material located in the end-caps behind the EM calorimeter. Each end-cap calorimeter consists of two wheels with 32  $\phi$ -sectors. The  $\Delta\eta \times \Delta\phi$  granularity is  $0.1 \times 0.1$  in the region  $|\eta| < 2.5$  and  $0.2 \times 0.2$  for larger values of  $\eta$ .

Lastly, the absolute pseudorapidity range between 3.1 and 4.9 is covered by two forward LAr calorimeters consisting of three cylindrical modules each. The first module is designed for EM calorimetry and uses copper as absorber material. The outer two modules use a tungsten absorber for hadronic calorimetry.

### Muon Spectrometer

The MS constitutes the outermost layer of the ATLAS detector and covers the range  $|\eta| < 2.7$ . It provides precision tracking for muons which are able to pass through the calorimeters with little interaction due to their minimum-ionizing nature. The MS is embedded in a magnetic field of 0.5 T in the barrel and 1 T in the end-caps, generated by toroid magnets bending muon trajectories in the  $\eta$ -direction. In the barrel region, three layers of rectangular tracking chambers are mounted on and between the eight toroid coils, giving in total 16  $\phi$ -sectors with partial overlaps. Three wheels with increasing radii, made of trapezoidal-shaped tracking chambers, are mounted perpendicular to the beam axis behind the forward calorimeters in each of the end-caps. Figure 3.5 gives a schematic side-view of the MS and its subsystems, which are explained in the following.

Monitored Drift Tube (MDT) chambers are the basic element of all three layers. They are made of layered arrays of gas-filled drift tubes aligned tangentially to circles around the  $z$ -axis, yielding a measurement of  $\eta$ . Muons traversing a MDT ionize the gas, and the drift time of the released electrons (and ions) to the wire anode in the center of the tube is measured, resulting in an average resolution of 80  $\mu\text{m}$  in the bending direction.

The measurement is complemented by Resistive Plate Chambers (RPCs) and Thin Gap Chambers (TGCs) mounted on the MDT chambers in the barrel and end-caps, respectively. RPCs are installed in the middle and outer layer of the MS and each module consists of two independent detector layers, each measuring  $\eta$  and  $\phi$ . The radially aligned readout strips on the outside of the TGCs, installed in the inner and middle layers of the MS end-caps, provide a measurement of the  $\phi$ -coordinate. Due to their fast readout time, signals provided by both the RPCs and TGCs are used in the trigger system, discussed in Section 3.2.3.

Lastly, Cathode Strip Chambers (CSCs) instead of MDT chambers are used for the

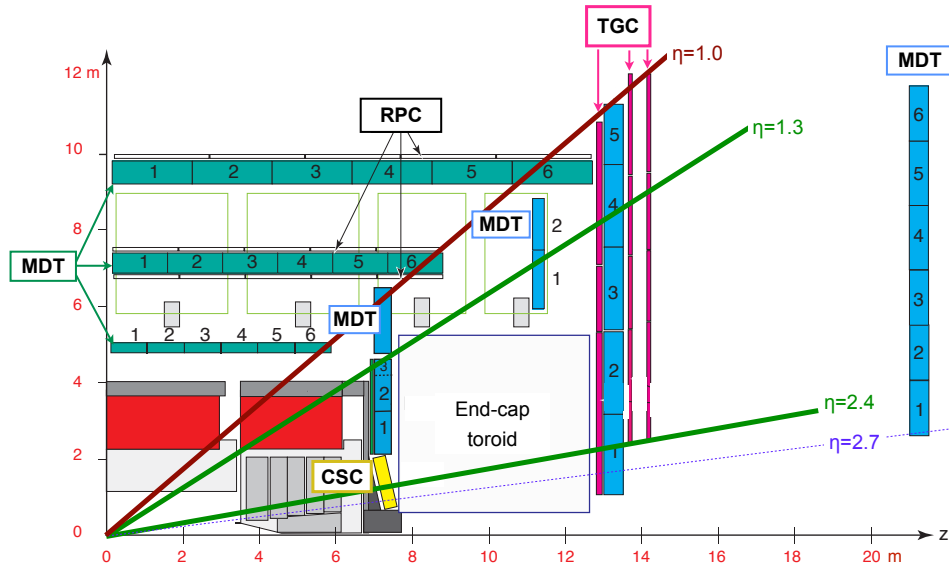


**Figure 3.5:** Schematic view showing a quarter-section of the Muon Spectrometer and its subsystems in the  $y$ - $z$  plane containing the beam axis. Figure adapted from Ref. [110].

precision tracking in the innermost layer of the end-cap region at pseudorapidities  $2.0 < |\eta| < 2.7$ . They are capable of withstanding the high particle rates in the forward region and provide measurements of  $\eta$  and  $\phi$ .

### 3.2.3 Trigger system

The bunch-crossing frequency of around 40 MHz and the average event size of 1 MB–2 MB does by far exceed the available computing and storage capabilities. As most of the scatter events do not contain particularly interesting physics, a two-level trigger system is employed to reduce the recorded event rate to about 1 kHz [111]. Various triggers search for interesting event topologies, such as events with specific, highly energetic particles or with a large missing transverse momentum [112–115].

The level-1 (L1) trigger is implemented in hardware and uses information with reduced granularity from the calorimeters as well as signals from the trigger chambers of the MS to identify regions-of-interest (RoIs) [116]. It accepts events at a rate of about 100 kHz which are then processed by a software-based high-level trigger (HLT) [117]. The HLT uses more sophisticated algorithms and information from all detector components to refine the reconstruction in the RoIs which it receives as input from the L1 trigger. The precision of the energy resolution and particle identification is therefore significantly improved and the HLT accepts events with a higher efficiency. Events that pass the selection criteria of the L1+HLT chain are then written to permanent storage.

As the total bandwidth is shared by all triggers, a prescale can be applied to reduce the rate of specific triggers. With a prescale factor of  $n$ , only every  $n$ -th event selected by the trigger is then actually recorded.

### 3.2.4 Luminosity and pile-up

Besides the center-of-mass energy  $\sqrt{s}$ , the instantaneous luminosity  $\mathcal{L}$  is another main characteristic of a particle collider and describes the particle flow density at the interaction point. For a circular proton collider it can be written as

$$\mathcal{L} = \frac{N_b^2 n_b}{4\pi\sigma_x\sigma_y} f, \quad (3.4)$$

where  $n_b$  is the number of bunches per beam,  $N_b$  is the number of protons per bunch,  $f$  is the revolution frequency and  $\sigma_{x(y)}$  is the transverse beam spread at the interaction point, assuming head-on collisions and a Gaussian beam profile [118]. The LHC was designed to have an instantaneous luminosity of  $10^{34} \text{ cm}^{-2} \text{ s}^{-1}$ , which was exceeded by a factor of two over the course of Run 2 [119].

The luminosity measurement for ATLAS in Run 2 was primarily performed by the Luminosity Cherenkov Integrating Detector 2 (LUCID-2) [120]. It consists of two modules of photomultiplier tubes around the beam pipe located 17 m away from the IP in each direction. Hits in the detectors are used to determine the visible mean number of interactions per bunch crossing. The visible cross section for inelastic  $pp$  scattering is measured by so-called *van der Meer* scans in special runs of the LHC [121]. The measurement is then extrapolated to the beam conditions in the nominal runs to determine the absolute luminosity scale for the  $pp$  interactions per bunch crossing.

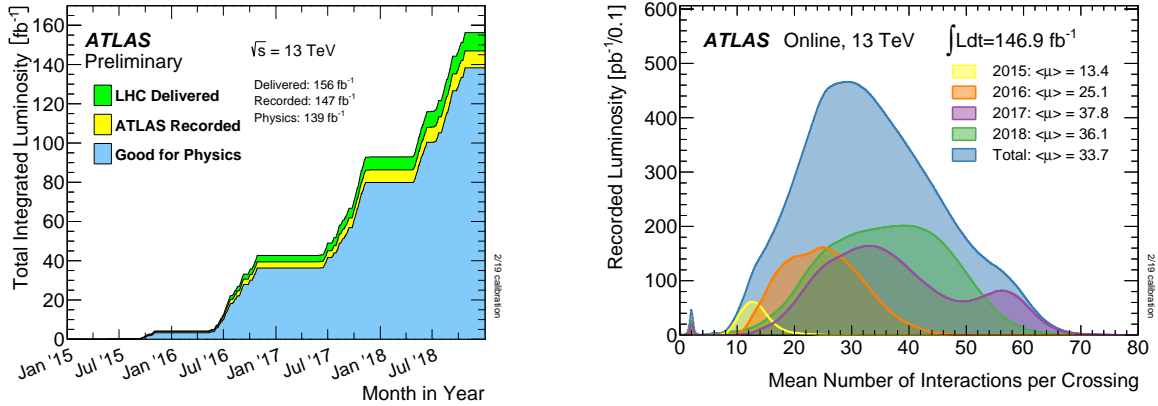
The size of the dataset produced in a given time period  $T$  is quantified by integrating the instantaneous luminosity:

$$L = \int_T \mathcal{L} dt. \quad (3.5)$$

Values for  $L$  are typically given in units of  $1 \text{ fb}^{-1} = 10^{24} \text{ cm}^{-2}$ . Figure 3.6a shows the integrated luminosity delivered by the LHC and recorded by ATLAS in Run 2. In total,  $147 \text{ fb}^{-1}$  of data were recorded of which  $139 \text{ fb}^{-1}$  passed the main quality criteria [122].

An increased mean number of  $pp$  interactions per bunch crossing, denoted as  $\mu$ , corresponds to a higher instantaneous luminosity. In the recording of a collision event, additional contributions can arise from the preceding or following bunch crossing that enter the read-out window of the detector. These effects are referred to as in-time or out-of-time pile-up, respectively. The average value of  $\mu$  is shown in Figure 3.6b as recorded by ATLAS for each year in Run 2.

The number of events of a certain process with cross section  $\sigma$  produced in the  $pp$



(a) Integrated luminosity as a function of time (b) Mean number of interactions per bunch crossing

**Figure 3.6:** Integrated luminosity as a function of time (a) and the distribution of the mean number of interaction per bunch crossing (b) for each year of data taking in Run 2 of the LHC. Figures adapted from Ref. [122].

collisions is then calculated as

$$N = \sigma \times L. \quad (3.6)$$

The rare beyond-SM processes studied in this thesis are expected to have a cross section of the order of pico to femto barns (cf. Sections 4.3.2 and 4.3.3).

# 4 Analysis overview

The purpose of this chapter is to give an overview of the analysis strategy. Recorded and simulated event samples are described and the reconstructed physics objects are defined. From these objects, variables that are effective in discriminating between signal and background events or between different background processes are introduced. Lastly, a minimal event selection is defined on which further selections of the analysis are based on.

## 4.1 Analysis strategy outline

Previous results, discussed in Section 2.4.1, showed that final states with two hadronically decaying tau leptons provide the highest potential to find a SUSY signature related to the stop-stau model. The primary reason for this is that for certain signal-sensitive variables, such as  $m_{T2}$  which will be introduced in Section 4.5, the discrimination power is degraded: Compared to the hadronic decay mode, an additional electron or muon neutrino from the leptonic tau-lepton decay contributes to the missing transverse momentum and thereby blurs the signature of other invisible particles in the signal. Therefore, only events with hadronically decaying tau leptons are considered in the analysis presented in this thesis. However, two event categories are defined, targeting different parts of the stop-stau parameter space, while also contributing to the search for pair-produced leptoquarks decaying into third-generation fermions.

The so-called *di-tau channel* selects events with at least two hadronically decaying tau leptons but no electrons or muons, at least one  $b$ -jet and large missing transverse momentum  $E_T^{\text{miss}}$ . The search in this channel is optimized for stop-stau signals with low to medium mass splitting  $\Delta m = m(\tilde{t}_1) - m(\tilde{\tau}_1)$ . For such signals, relatively hard tau leptons and soft  $b$ -jets are expected from the decays of the tau slepton and top squark, respectively.

The second, so-called *single-tau channel* selects events with exactly one hadronically decaying tau lepton, no lighter leptons, at least two  $b$ -jets and large  $E_T^{\text{miss}}$ . This selection targets stop-stau signals with large mass splitting  $\Delta m$ , where relatively soft tau leptons and hard  $b$ -jets are expected. Furthermore, it provides good sensitivity to events with  $LQ_3^{u/d}$  pair-production, where predominantly only one tau lepton is produced in the subsequent decays.

Signal regions (SRs) are defined, in which the expected number of signal events is

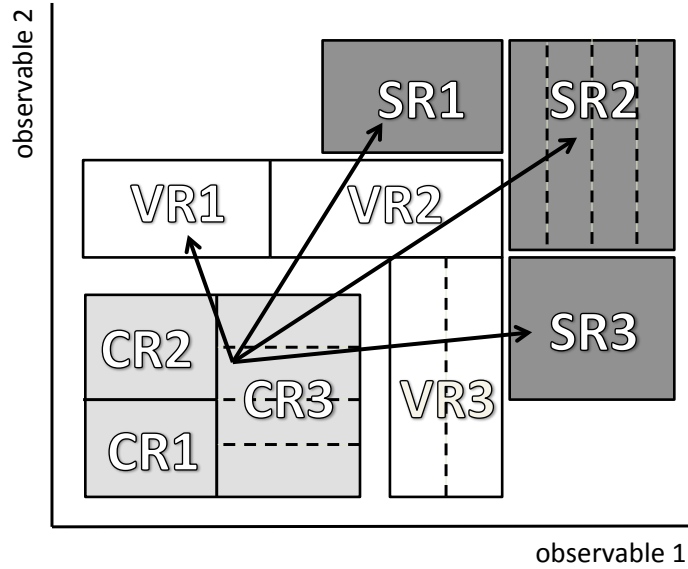


**Figure 4.1:** Schematic view of a generic analysis setup with control, validation and signal regions (CR, VR, SR). Regions can have one or multiple bins, as illustrated by the dashed lines. Figure adapted from Ref. [124].

significantly higher than the contribution from SM background processes. These event selections are optimized without knowledge of the actual event count observed in data. This is referred to as a *blind analysis* [123]. By not knowing the outcome beforehand, an analysis strategy is designed without unintentionally being biased towards a particular direction. Simulated data is used to predict the event yields of the signal and the various background processes in the event selections of the analysis. The contribution of the dominant SM backgrounds in the SR is constrained in dedicated selections. In these so-called control regions (CRs), their individual overall normalizations are derived in a simultaneous fit to the observed data. This can help to improve the modelling of the background in the extreme phase space probed by the SRs. The validity of the normalized background prediction is tested in validation regions (VRs). To ensure that the extrapolation of the background estimate to the SRs is sensible, the VRs are located kinematically close to the SRs.

The layout of control, validation and signal regions is visualized in Figure 4.1 for a generic analysis setup. The boundaries of these selections are defined by placing cuts, i. e. upper and/or lower bounds, on observables in the event. Note that all regions included in the statistical evaluation are designed to be orthogonal, i. e. pair-wise disjoint, to ensure their statistical independence.

After validating the background estimate, the SRs are unblinded and the compatibility of the observation with the signal-plus-background or the background-only hypothesis is assessed. In the absence of an excess over the SM background expectation, the result

can be interpreted in terms of exclusion limits.

The statistical models and evaluation procedures are described in Chapter 5. The design of the SRs and the estimation of the background is discussed in Chapters 6 and 7, respectively.

## 4.2 Collision data

The  $pp$  collision data at a center-of-mass energy of  $\sqrt{s} = 13$  TeV recorded with the ATLAS detector in 2015 through 2018 amounts to an integrated luminosity of  $147 \text{ fb}^{-1}$ , following the measurements described in Section 3.2.4. Events with poor beam or detector conditions are filtered out using a centrally provided list. The surviving events are flagged as ‘good for physics’, amounting to an integrated luminosity of  $139 \text{ fb}^{-1}$  [122]. Furthermore, additional quality requirements are applied, which are discussed in Section 4.7.

## 4.3 Simulation

The theoretical modelling of a hypothetical signal and most SM background processes is encoded in simulation. Monte-Carlo (MC) techniques are used to generate event samples. These so-called MC samples are crucial for the interpretation of the real data and aid in understanding how potential signals and backgrounds manifest in the experiment, thereby allowing to design selections sensitive to characteristic signatures. A comprehensive review of MC event generators for the simulation of proton–proton collisions at the LHC is given in Ref. [125].

The full ATLAS simulation chain [126] can be summarized in two main steps:

**Event generation:** First, the matrix element (ME) for a given process is calculated at the parton level to generate the so-called *hard-scattering* event. The *parton showering*, i. e. the fragmentation and subsequent hadronization of the particles produced in the interaction, is then simulated with dedicated algorithms.

**Detector simulation and digitization:** The detector response is modelled taking into account the geometry of the ATLAS detector and the interaction of the generated particles with the detector material. In the output, the hits in the individual subdetectors are converted into voltages and currents in the readout channels.

The factorization theorem allows to split the description of the hard-scattering process and parton showering [127]. The QCD interactions in the highly energetic hard-scattering process are calculated perturbatively in  $\alpha_s$  up to a selected order. Either initial or emerging color-charged partons can emit gluons, giving rise to additional quark-antiquark pairs in the event. This is called initial or final-state radiation (ISR,

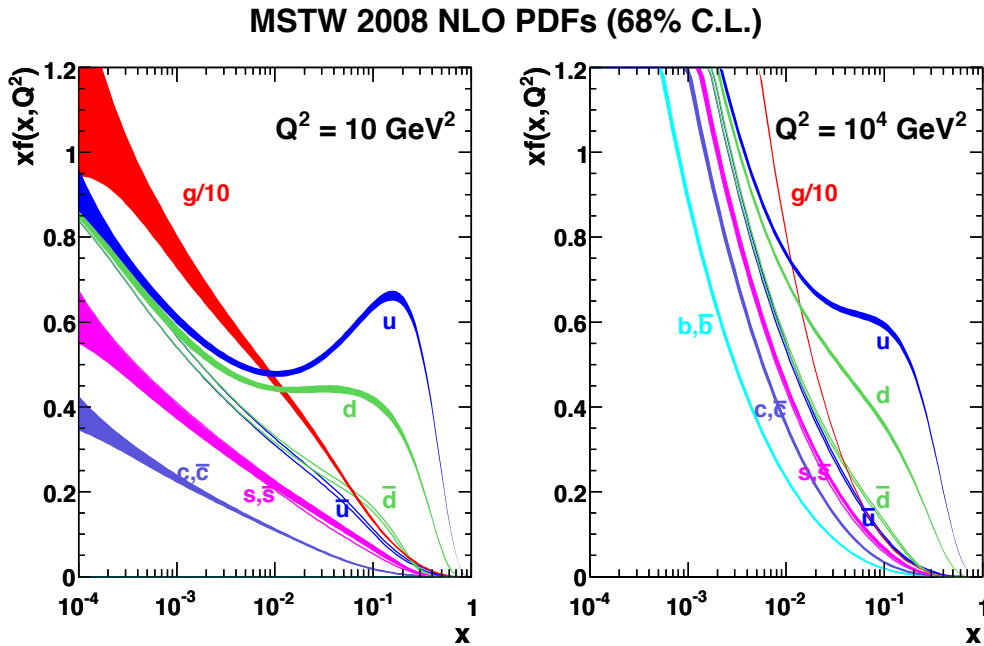


**Figure 4.2:** Example for parton density functions of the proton at low (left) and large (right) momentum transfers  $Q^2$ . Figure adapted from Ref. [129].

FSR), respectively, and leads to a cascade of partons. The showering is simulated step by step for each parton down to low energy scales, where they recombine to hadrons. At this scale,  $\alpha_S$  becomes large and perturbation theory breaks down. The hadronization is therefore described using phenomenological models [128]. As partons added by higher-order ME calculations and by the parton-showering simulation can lead to a double counting, different matching and merging methods exist to correctly combine the two outcomes.

As protons are composite particles, the momentum distribution of the individual partons within the proton has to be considered in the simulation of the hard interaction and the ISR. The ME calculation is convolved with the parton distribution functions (PDFs), which describe the probability of finding a certain parton with the momentum fraction  $x$  of the proton for a given momentum transfer  $Q^2$  in the collision. They are extracted from data from various collision experiments and can be computed for other values of  $Q^2$  using evolution equations [129]. An example for the proton PDFs at different scales is shown in Figure 4.2.

The so-called *underlying event* (UE) represent interactions of remaining partons in the collision, not associated with the original hard process or its ISR and FSR activity. These processes are described by phenomenological models and – like the parton-shower simulation – require free parameters to be tuned [130]. The usually rather soft contributions of the UE are overlaid with the final state of the hard-scattering process.

In order to compare simulated events with real data, the detector response is simulated

for the generated events. The GEANT4 simulation toolkit [131] is used to precisely model the detector geometry and materials as well as the magnetic fields. However, this approach, referred to as *full simulation*, is computationally very expensive. The ATLFAST-II program significantly lowers the processing time by using a parameterized simulation of the calorimeter showers [132]. It is used in applications which are less sensitive to the precise simulation of the detector response.

Detector hits from additional proton–proton interactions in the bunch-crossing are added to emulate the effects of pile-up. These so-called *minimum bias* events are generated with PYTHIA 8.186 [133] using the NNPDF2.3LO set of PDFs [134] and the A3 tune [135]. The tune fixes the free parameters of the simulation to give an optimal description of measured observables.

After the digitization step, MC events are processed by the same triggers, reconstruction and identification algorithms as the data and are weighted to exactly match the pile-up distribution observed in data. Besides the reconstructed event, MC samples retain the information on the originally generated event, referred to as *truth record*, giving insight into the simulated physics of the scattering process.

MC samples are generated with a varying amount of events and filters can be employed during the generation, selecting only certain event topologies and thereby increasing the computational efficiency. In order to compare the prediction with the data, MC samples need to be normalized to the total cross section  $\sigma$  of the given processes and scaled to the integrated luminosity  $\int L dt$  of the data. Furthermore, MC generators may assign weights  $\omega_i$  to events, requiring an overall normalization to the sum of weights of all generated events in the sample. A correction factor  $k$  can arise from higher order calculations of the cross section. The predicted MC event yield in a given selection is then given by

$$N_{\text{pred.}} = \frac{\int L dt \cdot k \epsilon_{\text{filter}} \sigma}{\sum_{i \in \text{generated}} \omega_i} \cdot \sum_{i \in \text{selected}} \omega_i, \quad (4.1)$$

where  $\epsilon_{\text{filter}}$  is the efficiency of the generator-level filter. The statistical uncertainty on the event yield, due to the limited size of the simulated event sample, is estimated via the sum of the squares of weights [136].

### 4.3.1 Background

A detailed summary of the generation of the different MC samples used in the analysis is given in Table 4.1. It lists the generators, the order of the cross-section computation, the PDF sets used in the ME calculation as well as the parameter tunes for the parton-shower and UE simulation.

The full GEANT4 [131] simulation of the ATLAS detector is used for all backgrounds. Except for samples produced with SHERPA [149], which uses a dedicated parton-shower

## 4 Analysis overview

| Physics process                 | Generator                     | Parton shower         | Tune           | Cross section      | PDF (ME)           |
|---------------------------------|-------------------------------|-----------------------|----------------|--------------------|--------------------|
| $t\bar{t}$                      | POWHEG-BOX v2 [137–140]       | PYTHIA 8.230 [141]    | A14 [130]      | NNLO+NNLL [142]    | NNPDF3.0NLO [143]  |
| Single top                      | POWHEG-BOX v2 [138–140, 144]  | PYTHIA 8.230          | A14            | NLO+NNLL [145–148] | NNPDF3.0NLO        |
| $V$ + jets                      | SHERPA 2.2.1 [149]            | SHERPA 2.2.1          | SHERPA default | NNLO [150]         | NNPDF3.0NNLO [143] |
| Diboson ( $VV$ )                | SHERPA 2.2.1 or 2.2.2 [149]   | SHERPA 2.2.1 or 2.2.2 | SHERPA default | NLO [151–153]      | NNPDF3.0NNLO       |
| Triboson ( $VVV$ )              | SHERPA 2.2.1                  | SHERPA 2.2.1          | SHERPA default | NLO [151–153]      | NNPDF3.0NNLO       |
| $t\bar{t} + V$                  | MADGRAPH5_aMC@NLO 2.3.3 [154] | PYTHIA 8.210 [141]    | A14            | NLO [154, 155]     | NNPDF3.0NLO        |
| $t\bar{t} + H$                  | POWHEG-BOX v2 [139, 140, 156] | PYTHIA 8.230          | A14            | NLO [154, 155]     | NNPDF3.0NLO        |
| $t\bar{t} + WW$                 | MADGRAPH5_aMC@NLO 2.2.2 [154] | PYTHIA 8.186 [141]    | A14            | NLO [154]          | NNPDF2.3LO [134]   |
| $t\bar{t} + WZ$                 | MADGRAPH5_aMC@NLO 2.3.3       | PYTHIA 8.212 [141]    | A14            | NLO [154]          | NNPDF3.0NLO        |
| $tWZ$                           | MADGRAPH5_aMC@NLO 2.3.3       | PYTHIA 8.212          | A14            | NLO [154]          | NNPDF3.0NLO        |
| $tZ, t\bar{t}, t\bar{t}\bar{t}$ | MADGRAPH5_aMC@NLO 2.3.3       | PYTHIA 8.230          | A14            | NLO [154]          | NNPDF3.1NLO [143]  |

**Table 4.1:** Simulated background samples with the corresponding matrix element (ME) and parton-shower generators. Also, the cross-section order in  $\alpha_S$  used to normalize the event yield and the PDF sets used in the ME calculation are given.

modelling and parameter tune developed by the SHERPA authors, all samples use the A14 tune [130] for the fragmentation and hadronization simulation, and the EVTGEN program [157] to model the decays of  $b$ - and  $c$ -hadrons.

Production of top-quark pairs, with or without an associated Higgs boson, and of single top quarks in the  $s$ - and  $t$ -channel or associated with  $W$  bosons is simulated with POWHEG-BOX [137–140]. Associated production of top-quark pairs with a vector boson  $V = W, Z$ , as well as top-related processes with smaller contributions ( $t\bar{t} + WW$ ,  $t\bar{t} + WZ$ ,  $tWZ$ ,  $tZ$ ,  $t\bar{t}\bar{t}$  and  $t\bar{t}\bar{t}\bar{t}$ ), in the following referred to as ‘other top’ processes, are simulated with MADGRAPH5\_aMC@NLO [154]. The hard-scatter events are interfaced to PYTHIA [141] to model the fragmentation and hadronization as well as the UE, using the NNPDF2.3LO PDF set [134]. The production of single vector bosons, diboson ( $VV$ ) and triboson ( $VVV$ ) events is simulated with SHERPA using the NNPDF3.0NNLO set of PDFs [143].

As  $t\bar{t}$  and single-top ( $Wt$ ) production are a major source of background in the analysis, additional samples filtered in  $E_T^{\text{miss}}$  at generator level are used. Thereby, the available MC statistic is significantly enhanced, allowing for a sufficiently precise background estimation in extreme phase-spaces sensitive to the signal.

The independent simulation of the single-top and  $t\bar{t}$  processes leads to a caveat: There are NLO  $Wt$  diagrams overlapping with LO  $t\bar{t}$  diagrams, which would lead to a double-counting. An example for such diagrams is shown in Figure 4.3. There are primarily two different methods to address this problem, the so-called *diagram-removal* (DR) and the *diagram-subtraction* (DS) scheme [158, 159]. The approach, followed in this analysis, is to use the DR method, where duplicate Feynman diagrams are simply removed in the ME calculation of the  $Wt$  process. However, this also eliminates effects arising from the interference of these diagrams. It is possible that certain regions of the phase-space become sensitive to the interference between these processes [160]. The alternative set of  $Wt$  samples using the DS scheme instead introduces an arbitrary subtraction term to the ME calculation, which cancels the overlap at the cross-section level and keeps the interference in the prediction. In regions of phase space enriched with  $Wt$  events, it has been observed that there are  $\mathcal{O}(100\%)$  differences between the two



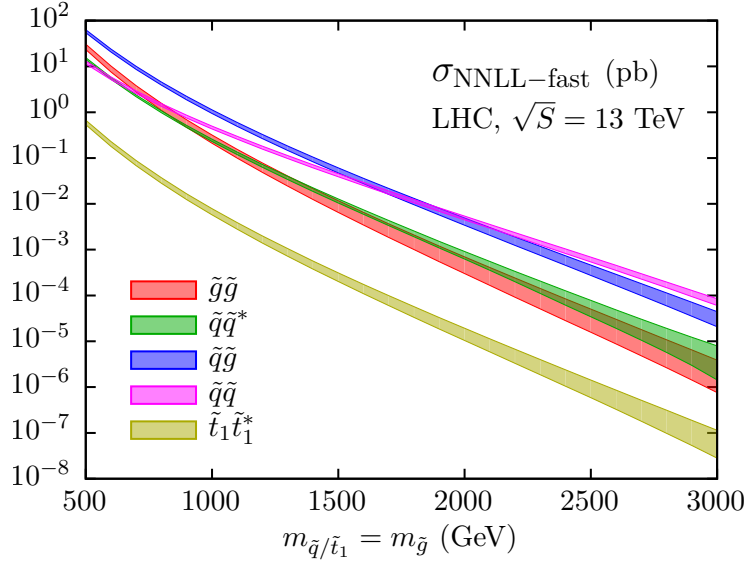


**Figure 4.4:** Cross section predictions for squark and gluino production at the LHC with  $\sqrt{s} = 13$  TeV, calculated at NNLO<sub>approx</sub>+NNLL accuracy. The top-squark pair-production cross-section is shown in yellow. Figure adapted from Ref. [165].

leading (NNLO<sub>approx</sub>) order in supersymmetric QCD, with the resummation of soft gluon emission at next-to-next-to-leading-logarithmic (NNLL) accuracy [165–168]. The nominal values and uncertainties as a function of  $m(\tilde{t}_1)$  can be found in Ref. [169] and are compared to other squark and gluino production cross-sections in Figure 4.4.

### 4.3.3 Third-generation scalar leptoquarks

Pair-production of scalar third-generation up or down-type leptoquarks,  $LQ_3^{u/d}$ , is simulated at NLO in QCD with MADGRAPH5\_aMC@NLO 2.3.3 according to the simplified model introduced in Section 2.4.2. The prompt  $LQ_3^{u/d}$  decay into quark-lepton pairs of the third generation is simulated with MADSPIN, preserving spin correlations, and  $b$ - and  $c$ -hadron decays are modelled with EVTGEN [157]. Subsequent fragmentation and hadronization as well as the UE are simulated in PYTHIA 8.230 [141] using the A14 tune [130]. The NNPDF3.0NLO [143] and NNPDF2.3LO PDF sets [134] are used for the ME and parton shower generation, respectively, and the detector response is simulated with ATLFAST-II.

All samples are generated with a coupling to charged leptons of  $\beta = 0.5$ , which corresponds to the regime targeted by this analysis. In total, 52 samples, 26 for each  $LQ_3$  type, are generated with leptoquark masses  $m(LQ_3^{u/d})$  ranging from 300 GeV to 2 TeV with varying step sizes of 50–100 GeV. In order to interpret the results of the analysis in the plane of leptoquark mass  $m(LQ_3^{u/d})$  versus branching ratio into charged leptons, events can be reweighted to any new branching ratio  $B_{cl} \in [0, 1]$ . The reweighting

factor is computed as

$$w(B_{\text{cl}}) = \left( \frac{B_{\text{cl}}}{\hat{B}_{\text{cl}}} \right)^{n_{\text{cl}}} \times \left( \frac{1 - B_{\text{cl}}}{1 - \hat{B}_{\text{cl}}} \right)^{(2 - n_{\text{cl}})} \quad (4.2)$$

where  $n_{\text{cl}} \in \{0, 1, 2\}$  is the number of charged leptons produced in the decay of the  $\text{LQ}_3^{\text{u/d}}$  pair and  $\hat{B}_{\text{cl}}$  corresponds to the branching ratio in the given sample, as determined by  $\beta$  and  $m(\text{LQ}_3^{\text{u/d}})$  according to Equations (2.13) to (2.16) discussed in Section 2.4.2.

The same cross sections as for direct top-squark pair production, discussed in the previous Section 4.3.2, are used for scalar  $\text{LQ}_3^{\text{u/d}}$  pair-production as both involve massive, scalar and color-charged particles and the production modes are the same. However, lepton  $t$ -channel contributions to the cross sections are neglected in the reference model [86] and may lead to corrections at the percent level [91].

## 4.4 Object definitions

In the following the reconstruction and identification of the various physics objects is briefly reviewed and their definitions are summarized. These objects are used to compute kinematic observables and object multiplicities in the event.

For the identification of particles, working points, developed by dedicated combined performance groups at ATLAS, are used, which correspond to a set of quality criteria or a minimal score of some multivariate discriminator. These working points are inclusive, meaning that objects passing a tight working point are also included in the selection defined by a looser working point. Corrections accounting for differences in the reconstruction and identification efficiencies of objects between simulation and data are also provided centrally and applied multiplicatively as additional event-wise weights in the computation of the MC event yield, cf. Equation (4.1). Additionally, reconstructed objects in MC samples can be matched to the truth record. This way, reconstructed objects can be labelled as *real* or *fake*, depending on whether they have been correctly identified or not.

All objects of the same type are ordered with respect to the magnitude of their transverse momentum, i. e. the term ‘leading’ or ‘subleading’ object then refers to the object with highest and second highest  $p_{\text{T}}$ , respectively. In mathematical expressions, this is reflected by indices. Note, however, that for SUSY particles the indices still represent the mass hierarchy, as introduced in Section 2.2.

### 4.4.1 Tracks and vertices

Tracks describe the trajectories of charged particles and serve as a basis for the reconstruction of physics objects. Clusters of hits in the Pixel Detector and in the SCT are used to build a track seed [170]. The track candidates are associated with hits further away from the interaction point by a combinatorial Kalman filter [171] and ambiguities are resolved by a neural network [172]. The surviving candidates are then extrapolated to hits in the TRT and the measurements from all three ID subsystems are refitted for the final tracks.

Collections of reconstructed tracks are used to find interaction vertices by extrapolating them to common origins [173, 174]. Tracks that are significantly displaced from the estimated vertex position are disassociated from that vertex and serve as seeds in the reconstruction of further vertices. The primary vertex (PV) is defined as the one with the highest  $\sum p_{\text{T}}^2$  of all associated tracks, and is assumed to be the location of the hard-scatter process in analysis.

### 4.4.2 Jets

The particle showers originating from fragmenting and eventually hadronizing colored particles, i. e. quarks and gluons, are reconstructed as cones. The lateral and longitudinal segmentation of the calorimeters allows for a three-dimensional reconstruction of the showers.

A topological clustering algorithm [175] is seeded by cells with a significant energy deposit and then merges both laterally and longitudinally adjacent cells to form a so-called *topo-cluster*. The energy entries are calibrated at the electromagnetic (EM) scale. A particle-flow algorithm [176] matches ID tracks to EM topo-clusters in order to remove overlaps between momentum and energy measurements made in the ID and calorimeter, respectively. The energy of the matched track is subtracted from the topo-cluster, taking into account the possibility that one particle contributes to multiple clusters or that multiple particles contribute to a single cluster. The resulting collection of selected tracks, matched to the PV, and positive energy topo-clusters surviving the energy subtraction step are then used as an input for the jet reconstruction. For this, the anti- $k_t$  algorithm [177] is employed using a radius parameter of  $R = 0.4$ , which defines the size of the jet cones. Finally, the jet-energy scale (JES) is calibrated in a procedure with multiple steps and relying heavily on MC simulation, as described in Ref. [176]. A jet-vertex tagger (JVT) provides a multivariate discriminant to suppress jets originating from pile-up activity [178]. Compared to the previous iteration of the search [82], the addition of the particle-flow reconstruction as input to jet-finding algorithm improves the momentum and angular resolution as well as the pile-up suppression [176].

The selected jets are required to have  $p_{\text{T}} > 20 \text{ GeV}$  and  $|\eta| < 2.8$ . Jets with  $p_{\text{T}} <$

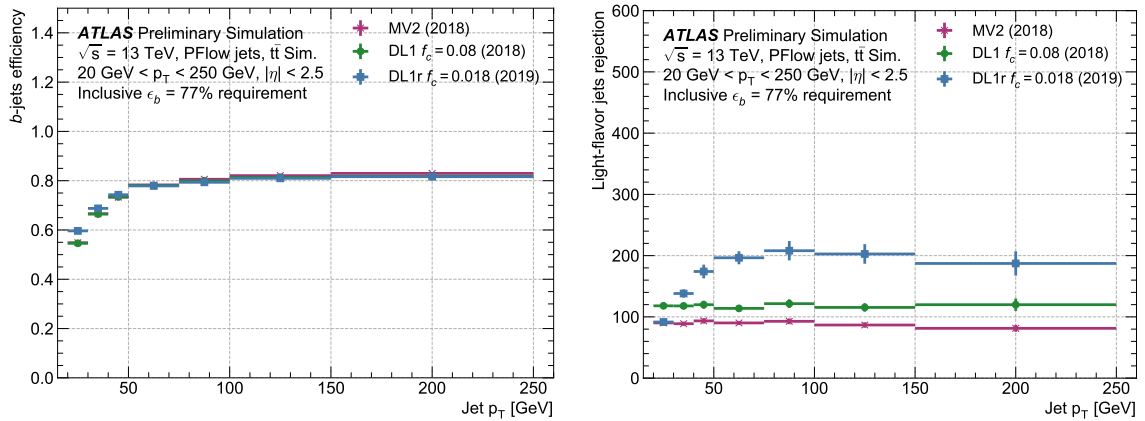


**Figure 4.5:** Identification efficiency and light-flavor rejection as a function of the jet  $p_T$  for the 77% working point. The performance is evaluated using anti- $k_t$   $R = 0.4$  particle-flow jets in simulated  $t\bar{t}$  events. Figures adapted from Ref. [182].

60 GeV and  $|\eta| < 2.4$  that have a JVT score less than 0.5 are removed.

### 4.4.3 $b$ -tagging

Jets originating from  $b$ -quarks can contain hadrons with a relatively long lifetime and high decay multiplicity. The relatively long lifetime of  $b$ -hadrons of the order of 1.5 ps ( $c\tau \sim 450 \mu\text{m}$ ) can lead to a vertex displaced from the associated PV that can be resolved by the ID [179]. The DL1R  $b$ -tagger [180, 181], a multivariate algorithm which uses tracking information and jet properties as an input, is used to discriminate jets initiated by a  $b$ -quark from those originating from gluons or other light quarks. The  $b$ -tagging algorithm uses a working point with an efficiency of 77% measured in simulated  $t\bar{t}$  events.

Figure 4.5 compares the  $b$ -tagging efficiency and light-flavor rejection rate to the MV2C10  $b$ -tagger [180, 181] used in the previous iteration of the search [82]. The efficiency decreases for smaller jet  $p_T$  as the decay vertices of  $b$ -hadrons are less displaced from the PV. Overall, a significant improvement in the rejection of fakes is observed [182].

### 4.4.4 Electrons

Electrons leave tracks in the ID and deposit their energy in the electromagnetic calorimeter. They are reconstructed by matching ID tracks to EM topo-clusters [183]. Clusters without matching tracks are considered photon candidates, which are, however, not further considered in this analysis. To account for bremsstrahlung effects, loosely matched tracks are refitted and nearby clusters may be added to the seed cluster. A multivariate

algorithm, exploiting properties of the shower development in the EM calorimeter, is employed to optimize the energy resolution, while the absolute energy scale is calibrated using measurements from  $Z \rightarrow ee$  decays [183]. A likelihood discriminant is used to identify prompt electrons and reject energy deposits from hadronic jets or converted photons and non-prompt electrons from the decays of heavy-flavour hadrons [183]. It is constructed from properties of the primary electron track, its spatial compatibility with the reconstructed cluster as well as the shape of the electromagnetic shower in the EM calorimeter.

Selected electrons are required to have  $p_T > 10 \text{ GeV}$  and  $|\eta| < 2.47$  and must fulfill the *LooseAndBLayerLLH* identification requirement [183], which takes the tracking information from the IBL into account. The longitudinal impact parameter  $|z_0 \sin \theta|$  is restricted to less than 0.5 mm in order to reject contamination from pile-up interactions.

#### 4.4.5 Muons

The muons in the  $p_T$  regime considered in this analysis usually traverse the whole detector due to their properties as minimum-ionizing particles. Hence, they leave tracks in the ID and MS, giving rise to a unique signature. Tracks in the MS are formed in a fit to the segments, which are straight-line tracks fitted to the hits in the MDT or CSC chamber, from the different MS layers taking into account the deflection of the muon by the magnetic field. Different methods to reconstruct muon candidates exist and are performed independently and in parallel. A comprehensive description is given in Ref. [184], which is summarized in the following. Combined muons, the most common type, are reconstructed by extrapolating MS to ID tracks or vice versa in a complementary approach, and taking into account the energy loss in the calorimeters. Extrapolated muons correspond to candidates outside the ID coverage and are reconstructed from MS segments extrapolated to the PV. Lastly, there are two approaches to extend the coverage to low- $p_T$  muons and those traversing regions of the detector with reduced acceptance. Segment-tagged muons are reconstructed by extrapolating ID tracks to single segments in the innermost layer of the MS, which helps to recover muons that only reach the first stations of the MS. Calo-tagged muons are built from an ID track which is matched to energy deposits in the calorimeter compatible with a minimum-ionizing particle. Corrections to the momentum calibration are derived from resonant  $Z \rightarrow \mu\mu$  and  $J/\psi \rightarrow \mu\mu$  events and are applied to the muons in simulation [185].

Muon candidates must fulfill the *Medium* identification working point [184] and are required to have  $p_T > 10 \text{ GeV}$  and lie within  $|\eta| < 2.7$ . Furthermore, the impact parameter must satisfy  $|z_0 \sin \theta| < 0.5 \text{ mm}$ .

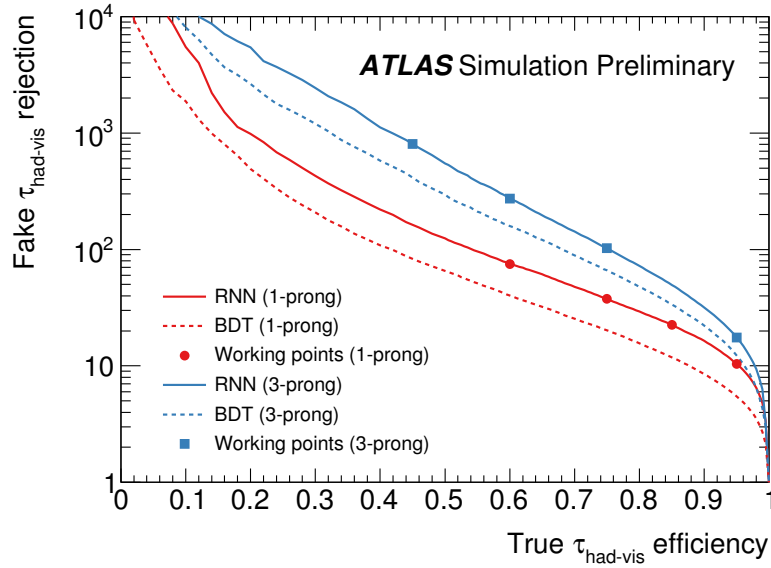


**Figure 4.6:** Rejection power for quark and gluon jets misidentified as taus as a function of identification efficiency. Shown are the curves for 1-prong (red) and 3-prong (blue) tau candidates using the RNN-based (full line) and the BDT-based (dashed line) identification algorithms. The markers indicate the four defined working points *Tight*, *Medium*, *Loose* and *Very Loose* with increasing signal selection efficiencies [186]. Figure adapted from Ref. [186].

#### 4.4.6 Hadronically decaying tau leptons

Due to the short decay length of  $87\ \mu\text{m}$  tau leptons typically decay within the beam pipe before reaching the innermost layer of the pixel detector. Tau leptons decay into a tau neutrino and, via the exchange of a  $W$ -boson, into either a pair of light quarks or a light lepton and a neutrino. Thus only their electromagnetically interacting or hadronic decay products can be observed, and a fraction of their initial momentum, carried by the neutrino(s), contributes instead to the total missing transverse momentum. The leptonic decay mode cannot be reconstructed, as the leptons cannot be reliably distinguished from those produced in electroweak boson decays. The produced electron or muon can be selected in the analysis by the aforementioned criteria. With about 65%, the most likely decay mode is the hadronic one, where the tau lepton predominantly decays into one (72%) or three (22%) charged pions, and is often (68%) accompanied by one or more neutral pions. Therefore, the *tau* objects referred to in this thesis are defined as the visible decay products of its hadronic decay mode. That means, that tau is an abbreviation for the reconstructed visible decay products of a hadronically decaying tau lepton. Note, that when referring to the undecayed SM particle, the expression tau lepton is used instead.

The tau reconstruction algorithm is seeded by anti- $k_t$  jets built from locally calibrated [187] topo-clusters, using a distance parameter  $R = 0.4$  and requiring  $p_T >$

10 GeV and  $|\eta| < 2.5$  [188–190]. A tau-vertex-association algorithm [189] determines the production vertex of the tau lepton. The BDT-based energy calibration applies a pile-up subtraction and a correction to the detector response and also factors in tau particle-flow information [189–191]. In order to identify jets originating from hadronically decaying tau leptons a multi-variate approach via a recurrent neural network (RNN) is used [186]. It exploits characteristic input variables related to the shower shape in the calorimeter, the internal jet structure and track impact parameters. The RNN provides a discriminant against gluon- or quark-initiated jets resulting in a similar signature. This novel classifier supersedes the former BDT-based tau identification method, which was used for the previous iteration of the stop-stau search [82], and provides a largely improved fake rejection as shown in Figure 4.6.

Taus are selected if they have a  $p_T$  larger than 20 GeV and lie outside the transition region,  $1.37 < |\eta| < 1.52$ , of the detector where the overlap of different subdetectors makes the tau identification and reconstruction challenging. Furthermore, they must have either one or three charged tracks, also called *prongs*, with a charge sum of  $\pm 1$ . Tau candidates are required to pass the *Medium* RNN identification working point [186], which has shown to strike an optimal balance between signal acceptance and the rejection of fake-tau backgrounds. This results in an identification efficiency of 75 % for one-prong and 60 % for three-prong taus. Additionally, a dedicated algorithm is used to reject electrons faking taus based on a *Medium* working point [189].

#### 4.4.7 Overlap removal

The various physics objects are reconstructed independently, which can lead to ambiguities when one physical object is reconstructed by multiple different algorithms. Therefore, an overlap removal procedure is applied to all events after reconstruction, resulting in the final object selection. The procedure follows the prescription recommended by the SUSY working group of the ATLAS collaboration. The overlap removal is performed sequentially and a summary of all consecutive steps and their conditions is given in Table 4.2. Here,  $\Delta R_y \equiv \sqrt{(\Delta y)^2 + (\Delta\phi)^2}$ , with the rapidity  $y$ , is used to measure the distance of two objects.

First, for two electrons sharing an ID track, the one with lower transverse momentum is discarded. Taus overlapping with an electron or a muon within  $\Delta R_y = 0.2$  are removed. If an electron shares an ID track with a muon, the electron is discarded unless the muon is tagged as a minimum-ionising particle in the calorimeter without associated MS tracks, in which case the muon is discarded. Next, jets within  $\Delta R_y = 0.2$  of an electron are removed, otherwise the electron is removed if within  $\Delta R_y = 0.4$ , in order to suppress electrons from semileptonic heavy-flavor decays. Any jet with less than three associated tracks is discarded if a muon is within  $\Delta R_y = 0.2$  or if a muon can be matched to a track associated with the jet. For the same reason as for electrons, muons within  $\Delta R_y = 0.4$  of a jet are removed. Lastly, jets within  $\Delta R_y = 0.2$  of a tau are removed.

|     | Object<br>discarded | Object<br>compared against | Condition   |
|-----|---------------------|----------------------------|---|
| 1.  | Electron            | Electron                   | Shared track, $p_T(e_1) < p_T(e_2)$   |
| 2.  | Tau                 | Electron                   | $\Delta R_y < 0.2$  |
| 3.  | Tau                 | Muon <sup>2</sup>          | $\Delta R_y < 0.2$  |
| 4.  | Muon                | Electron                   | Muon is calo-tagged<br>and shared ID track  |
| 5.  | Electron            | Muon                       | Shared ID track   |
| 6.  | Jet                 | Electron                   | $\Delta R_y < 0.2$  |
| 7.  | Electron            | Jet                        | $\Delta R_y < 0.4$  |
| 8.  | Jet                 | Muon                       | $N_{\text{tracks}} < 3$ and either<br>ghost-associated <sup>3</sup> or $\Delta R_y < 0.2$ |
| 9.  | Muon                | Jet                        | $\Delta R_y < 0.4$  |
| 10. | Jet                 | Tau                        | $\Delta R_y < 0.2$  |

**Table 4.2:** Consecutive steps of the overlap-removal procedure performed for all physics objects defined in Section 4.4. Here  $\Delta R_y$  is calculated using the rapidity instead of the pseudorapidity used for  $\Delta R$ .

#### 4.4.8 Missing transverse momentum

Momentum conservation in the transverse plane dictates that the transverse momenta of all particles produced in the interaction should sum up to zero. The presence of detector-invisible particles can thus be inferred from a momentum imbalance, unless their momenta happen to cancel each other. For the investigated signal models, which are expected to produce highly energetic neutrinos and LSPs, this imbalance can be significant.

The missing transverse momentum  $\mathbf{E}_T^{\text{miss}}$  is defined as the negative vector sum of the transverse momenta of all the identified and calibrated physics objects, after the overlap removal described above, photons and an additional soft term. The soft term is constructed from all tracks that are not associated with any physics object, and that are associated to the PV. In this way, the missing transverse momentum is adjusted for the best calibration of the jets and the other identified physics objects above, while maintaining pile-up independence in the soft term. The *Tight* working point for the jet selection entering the  $E_T^{\text{miss}}$  computation is used [193].

The objects-based  $E_T^{\text{miss}}$  significance  $\mathcal{S}(E_T^{\text{miss}})$  is used to discriminate events with genuine  $E_T^{\text{miss}}$ , generated by invisible particles, from events in which  $E_T^{\text{miss}}$  is caused by mis-measurements. It takes into account the expected resolutions of all the objects that enter the  $E_T^{\text{miss}}$  reconstruction and their directional correlations as described in Ref. [194].

<sup>2</sup>If  $p_T(\tau) > 50$  GeV, taus are only compared to combined muons.

<sup>3</sup>Ghost association is a method to associate particles to jets by giving them negligible momentum and clustering them within the jets [192].

## 4.5 Kinematic observables

Besides the directly observable object multiplicities and their properties such as their energy and direction, additional kinematic quantities can be constructed in order to target the signature of certain processes more efficiently. This section describes these so-called *high-level* variables that are valuable in the design of signal, control and validation regions. Kinematic distributions of signal and background processes for these variables are shown and discussed in Chapters 6 and 7.

**Invariant mass:** The invariant mass  $m(a, b)$  of two visible particles  $a$  and  $b$  is defined as the absolute value of the sum of their four-momenta  $p^\mu(a)$  and  $p^\mu(b)$ .

**Transverse mass:** The transverse mass  $m_T(a)$  is used to reconstruct the mass  $M$  of a mother particle decaying into a visible particle  $a$  and an invisible one. The invisible particle's momentum manifests as  $\mathbf{E}_T^{\text{miss}}$  in the event. Due to the unknown longitudinal momentum  $m_T(a)$  is bound from above by  $M$ . The square of the transverse mass can be written as

$$m_T(a)^2 = 2p_T(a)E_T^{\text{miss}}(1 - \cos \Delta\phi(a, \mathbf{E}_T^{\text{miss}})), \quad (4.3)$$

where a  $\Delta\phi(a, \mathbf{E}_T^{\text{miss}})$  is the angular separation of  $a$  and the invisible transverse momentum  $\mathbf{E}_T^{\text{miss}}$  in the transverse plane. Here, the masses of the daughter particles are assumed to be negligible.

A prominent application of this variable is the measurement of the  $W$ -boson mass  $m(W)$ : For leptonic decays the transverse mass  $m_T(\ell)$  of the lepton  $\ell$  features a cut-off in its distribution at  $m(W)$ . Due to detector effects and additional invisible particles entering  $E_T^{\text{miss}}$ , this distribution is smeared out.

**Stransverse mass:** The stransverse mass  $m_{T2}(a, b)$  of two visible particles  $a$  and  $b$  can be viewed as a generalization of the transverse mass for scenarios with two symmetric decays of a mother particle into a visible and an invisible particle [195, 196]. As in this case it is unknown how the measured  $E_T^{\text{miss}}$  is distributed among the invisible particles, all possibilities to calculate  $m_T(a)$  and  $m_T(b)$  have to be considered. The combination which leads to the smallest value of the maximal  $m_T$  is defined as  $m_{T2}(a, b)$ :

$$m_{T2}(a, b)^2 = \min_{\mathbf{q}_a + \mathbf{q}_b = \mathbf{E}_T^{\text{miss}}} (\max\{m_T(a)^2, m_T(b)^2\}), \quad (4.4)$$

where the three-momenta  $\mathbf{q}_a$  and  $\mathbf{q}_b$  of the invisible particle associated to  $a$  and  $b$ , respectively, enter the calculation of  $m_T(a)$  and  $m_T(b)$ , respectively, instead of  $\mathbf{E}_T^{\text{miss}}$ . Again the masses of the visible and invisible particles are assumed to be negligible. The stransverse mass has an upper bound given by the mass  $M$  of the mother particle.

This variable can therefore be used to discriminate the signal from background in the di-tau channel: The production of a  $t\bar{t}$  pair can yield the same observable particle content in the final state as the stop-stau signal. However the  $m_{T2}(\tau_1, \tau_2)$  distribution for the two leading taus features a cut-off at the  $W$ -boson mass in the case of  $t\bar{t}$  production, while, depending on the mass of the tau slepton, the cut-off in the case of the stop-stau process can be much higher. Thus  $m_{T2}(\tau_1, \tau_2)$  shows a strong discrimination power for stop-stau models with low to medium mass-splitting, i.e. high  $m(\tilde{\tau}_1)$  and a small contribution to  $E_T^{\text{miss}}$  by neutrinos produced in the top-squark decay.

**Scalar sum of leading hadronic transverse momenta:** This variable is defined as the scalar sum of transverse momenta of the up to two leading jets and up to two leading taus:

$$s_T = \sum_{i=1,2} p_T(j_i) + \sum_{j=1,2} p_T(\tau_j). \quad (4.5)$$

It gives a measure for the overall energy scale carried by hadronically decaying particles in the event.

**Opposite-sign flag:** This flag distinguishes whether two particles,  $a$  and  $b$ , carry electric charges with the same sign or not. It is defined as

$$OS(a, b) = \begin{cases} 1 & \text{if the el. charges of } a \text{ and } b \text{ have the same sign,} \\ 0 & \text{if the el. charges of } a \text{ and } b \text{ have opposite signs,} \end{cases} \quad (4.6)$$

and is typically used to discriminate between particles originating from a pair-production process and those without a preferred charge configuration.

## 4.6 Trigger

The necessity and working principle of triggers used in the data collection has been explained in Section 3.2.3. All triggers considered for this analysis are unprescaled, meaning that all events selected by the trigger are then written to storage. Due to increasing pile-up, the thresholds required by the triggers have also been raised over the course of Run 2 in order to assure a manageable stream of data. The discrepancies between the online and offline reconstruction, that lead to an inefficiency of the trigger, are bypassed by applying additional so-called *plateau cuts* to ensure that the trigger is to a good approximation fully efficient.

The following types of triggers were initially considered in the design of the analysis:

**$E_T^{\text{miss}}$  trigger:** This trigger selects events with a large amount of missing transverse momentum  $E_T^{\text{miss}}$  in the event. Muons do not enter the online  $E_T^{\text{miss}}$  calculation.

| Trigger                      | Trigger leg                | Year        | Online | Offline |
|------------------------------|----------------------------|-------------|--------|---------|
| Di-tau+met<br>trigger        | Leading tau $p_T$ [GeV]    | 2015 – 2017 | 35     | 50      |
|                              |                            | 2018        | 60     | 75      |
|                              | Subleading tau $p_T$ [GeV] | 2015 – 2018 | 25     | 40      |
|                              | $E_T^{\text{miss}}$ [GeV]  | 2015 – 2018 | 50     | 150     |
| Asymmetric<br>di-tau trigger | Leading tau $p_T$ [GeV]    | 2015 – 2018 | 80     | 95      |
|                              | Subleading tau $p_T$ [GeV] | 2015 – 2017 | 50     | 60      |
|                              |                            | 2018        | 60     | 75      |

**Table 4.3:** Online thresholds and associated plateau cuts that ensure that the selected events are selected with full efficiency by the corresponding legs of the given di-tau triggers.

**Asymmetric di-tau trigger:** Only events with two or more taus are selected, with the  $p_T$  threshold for the leading tau being significantly higher than for the subleading tau. In addition these two taus must pass the *Medium* online identification working point, which has a higher efficiency and fake-acceptance than the corresponding offline RNN-based working point [197].

**Di-tau+ $E_T^{\text{miss}}$  trigger:** In addition to a requirement of at least two taus passing the *Medium* online identification, a relatively high amount of  $E_T^{\text{miss}}$  is required. The  $p_T$  threshold for the tau candidates are lower and closer to one another compared to the asymmetric di-tau trigger and the  $E_T^{\text{miss}}$  threshold is lower than the one required by the  $E_T^{\text{miss}}$  trigger.

**Single-tau trigger:** Events with one or more taus are selected, with the leading tau required to pass a high  $p_T$  threshold as well as the *Medium* online identification working point.

The fully reconstructed taus are matched to the objects selected by the tau triggers. This means the leading tau must have fired the single-tau trigger, while the leading and subleading tau must have fired the first and second leg of the di-tau triggers, respectively. Correction factors accounting for potential trigger-efficiency differences between data and MC simulation are applied to the matched objects.

The turn-on behavior of the triggers has been studied by multiple other analyses across ATLAS. For the  $E_T^{\text{miss}}$  trigger an offline threshold is placed at 250 GeV. While lower values would have been possible for the individual  $E_T^{\text{miss}}$  triggers used in earlier phases of Run 2, the analysis does not profit from the additional statistics in a significant way. Similarly for the single-tau trigger the plateau cut is set to 180 GeV for all years. For the two di-tau triggers the associated plateau cuts are listed in Table 4.3.

Over the course of the optimization studies that will be discussed in Chapter 6, the  $E_T^{\text{miss}}$  trigger turned out to be the best choice for either of the channels. For the di-

tau SR, targeting low to medium stop-stau mass splittings, this is due to the high  $E_T^{\text{miss}}$  generated by the gravitinos in the tau-slepton decay. On the other hand, for the single-tau SR, targeting stop-stau with high mass splitting as well as  $LQ_3^{u/d}$  signals, either the neutrinos from the top-squark decay or those produced in the  $LQ_3^{u/d}$  decay, respectively, lead to high  $E_T^{\text{miss}}$  in the event.

## 4.7 Event preselection

All reconstructed events are subjected to the standard ATLAS event cleaning procedure [122]. As described in Section 4.2, collision events are only selected if they were recorded under fully operational detector conditions. If an error status is reported for the tile or LAr calorimeters or the SCT, the event is rejected. Incompletely recorded events are removed. Further requirements are applied for both data and MC events. Events need to have at one least reconstructed PV as defined in Section 4.4.1. Furthermore, events with cosmic muons in the vicinity of the PV ( $|z_0| < 1.0$  mm or  $d_0 < 0.2$  mm) as well as events with badly reconstructed muons, which have a poor momentum resolution, are rejected. Jets originating from non-collision background can affect observables such as  $E_T^{\text{miss}}$ . Therefore, a series of criteria is applied to each jet, removing the event if any one of the jets does not satisfy a *loose* cleaning working point [198].

On top of the event-cleaning criteria, a common preselection for regions defined in the analysis is applied. The set of cuts is given in Table 4.4 for the di-tau and single-tau channel. The requirements on the multiplicities of taus ensure that there is no overlap in terms of selected events between the channels.

Both channels veto events that have electrons or muons and focus on final states with only hadronically decaying tau leptons and  $b$ -jets. Due to the large amount of  $E_T^{\text{miss}}$  expected from both signal models in either of the signal region the  $E_T^{\text{miss}}$  trigger is used to select events. This choice was made following the SR optimization studies, which will

| Di-tau preselection   | Single-tau preselection                          |
|---|--|
| $E_T^{\text{miss}}$ -trigger fired and $E_T^{\text{miss}} > 250$ GeV<br>No light leptons ( $e/\mu$ )<br>At least two jets<br>At least one $b$ -tagged jet |  |
| At least two taus   | Exactly one tau<br>At least two $b$ -tagged jets |

**Table 4.4:** Preselection cuts for the di-tau and single-tau channel. The cuts above the line are common to both channels and referred to as *common preselection*.

be presented in Chapter 6. The plateau cut at 250 GeV also leaves enough headroom for control and validation regions with sufficient statistics. Since both signals feature two  $b$ -quarks in the final state, all selected events must have at least two jets with at least one of them being  $b$ -tagged. In the di-tau channel the available statistics is quite limited and the  $b$ -jets produced by the targeted class of stop-stau signals are relatively soft, which is why a requirement of two or more  $b$ -tagged jets is not beneficial. On the other hand, as the single-tau selection targets stop-stau signals with large mass splitting as well as high-mass  $LQ_3^{u/d}$  signals — both leading to high- $p_T$   $b$ -jets— the  $b$ -tag multiplicity is tightened in that channel by requiring at least two.

Due to the presence of  $b$ -jets in the selected events in both channels, the background, as predicted by the simulation, is dominated by top-related processes, in particular  $t\bar{t}$  or single-top production. By comparing the reconstructed taus against their truth record in MC the  $t\bar{t}$  background is further differentiated with respect to the multiplicity of fake taus:

**$t\bar{t}$  (2 real  $\tau$ ):** Both the leading and the subleading tau are real, i. e. truth-matched, which corresponds to a fully tauonic decay of the  $t\bar{t}$  pair. This background is of course only relevant in the di-tau channel.

**$t\bar{t}$  (1 real  $\tau$ ):** In a di-tau selection either the leading or the subleading tau is real while the other is fake. In the single-tau channel the one selected tau is required to be real. This process corresponds to a semi-tauonic decay of the  $t\bar{t}$  pair, i. e. one  $W$ -boson decaying into a (hadronically decaying) tau and the other decaying into quarks, yielding one to two jets. To a lesser extent also fully tauonic  $t\bar{t}$  decays, where only one tau is reconstructed, are picked up by this definition (cf. Section 4.4.6).

**$t\bar{t}$ -fake:** The up to two leading taus cannot be truth-matched, corresponding to events with a fully hadronic decay of the  $t\bar{t}$  pair or a leptonic decay with missed leptons.

Due to its lower cross-section  $t\bar{t}$  production in association with a vector boson contributes significantly less. The single-top background is dominated by  $Wt$  production. Other backgrounds such as  $W$ +jets,  $Z$ +jets and multiboson production are suppressed by the tau and  $b$ -tag requirements and thus play a lesser role in the event selections.

Data-driven studies have been performed to assess the contribution of multijet events in the analysis, i. e. QCD interactions creating final states containing only jets. Such events yield neither real taus nor invisible particles leading to  $E_T^{\text{miss}}$  in the event and can only enter the selection through fake taus and mis-measured jet energies. As multijet processes have a very large cross section, there are no MC samples with sufficient statistics to reliably describe this background. The contribution was therefore estimated from the difference in yields between the observed data and simulated other backgrounds in multijet-enriched event selections, and then extrapolated to the selections used in the analysis. For the di-tau channel the contribution in a selection with

opposite-sign taus is directly estimated from the corresponding same-sign selection, as both charge combinations are produced with approximately equal probability in multijet events. For the single-tau channel the contribution was extrapolated from an orthogonal selection with exactly one  $b$ -jet and the extrapolation factor was derived in statistically independent selections. With  $(1.2 \pm 3.1) \%$  in the di-tau and  $(0.2 \pm 0.3) \%$  in the single-tau preselection, the multijet contribution was found to be negligible. The main reason for that is the quick decline of the multijet contribution with increasing  $E_T^{\text{miss}}$  as well as the tau and  $b$ -jet requirements. The multijet background is thus not considered in the following.



# 5 Statistical methods

In order to give a quantitative interpretation of the outcome of an experiment, a probabilistic model is required. The frequentist approach to statistical inference is adopted, in which the given experiment is considered as one of an infinite sequence of possible repetitions of the same experiment, each producing statistically independent results [199]. In this chapter, the statistical concepts and methods used for the interpretation of the results as well as the treatment of systematic uncertainties is reviewed. The mathematical description follows Ref. [200].

The technical implementation is done in the HISTFITTER framework [124], which is based on the HISTFACTORY, ROOFIT and ROOSTATS packages [201–203].

## 5.1 Likelihood

The probability to observe  $n$  events in a selection is given by the Poisson distribution

$$P(n|\lambda) = \frac{\lambda^n e^{-\lambda}}{n!}, \quad (5.1)$$

if these events occur with a expected mean rate  $\lambda$  and independently from one another. The mean can be parameterized as

$$\lambda = \mu s + b, \quad (5.2)$$

where  $s$  is the expected signal yield, scaled by  $\mu$ , and  $b$  corresponds to the expected total background expectation. The parameter  $\mu$  is called *signal strength*, with  $\mu = 0$  corresponding to the background-only hypothesis and  $\mu = 1$  to the signal-plus-background hypothesis, with the signal expectation at the predicted cross section.

The expected event rate can depend on a set of parameters  $\boldsymbol{\theta} = (\boldsymbol{\omega}, \boldsymbol{\alpha})$ : The signal and background expectations are subject to systematic effects, originating from experimental or theoretical uncertainties and are parameterized by nuisance parameters  $\boldsymbol{\alpha}$ . The nuisance parameters  $\boldsymbol{\alpha}$  are constrained by auxiliary measurements, usually performed externally, and projected onto standard Gaussian distributions,

$$G(\alpha) = \frac{1}{\sqrt{2\pi}} e^{-\frac{\alpha^2}{2}}. \quad (5.3)$$

Additional free parameters  $\omega$  can be introduced to normalize the contributions from certain background processes. They are constrained by observations in dedicated selections (CRs), described by the Poisson distributions. Therefore, at least one CR is required for each normalization factor used in the analysis in order to have a sufficiently determined system of equations.

Schematically, the likelihood then takes the general form

$$L(\mu, \theta) = \prod_{i \in \mathbf{S}} P(n_i | \lambda_i(\mu, \theta)) \prod_{\alpha_j \in \alpha} G(\alpha_j), \quad (5.4)$$

where the index  $i$  runs over the set of statistically independent selections  $\mathbf{S}$  included in the fit setup, discussed in Section 5.3. The  $\pm 1\sigma$  variations of the event counts are represented by  $\alpha_j = \pm 1$  for the given systematic variation  $j$ . As described in Refs. [124, 201], methods to interpolate and extrapolate values of  $\alpha_j$  are used, and additional terms are included, e.g. to model the uncertainties on the luminosity or due to limited MC sample size. The best-fit values for the free parameters are computed using a maximum likelihood (ML) approach. Correlation between the nuisance parameters can arise since their variations can affect the predicted event yields in multiple selections at once and the final uncertainties are derived by error propagation from the covariance matrix.

## 5.2 Hypothesis tests

Hypothesis tests are a method of statistical inference to evaluate whether a hypothesis is compatible with the data or not. In order to assess the discovery of a signal, an alternative hypothesis  $H_1$ , which includes both signal ( $\mu = 1$ ) and background in the statistical model of the data, is compared to the null hypothesis  $H_0$  that describes only known processes ( $\mu = 0$ ), designated as background. When setting exclusion limits on the presence of a signal, the roles are reversed and the signal-plus-background hypotheses acts as  $H_0$ , which is tested against the alternative background-only hypothesis  $H_1$ .

In order to test the competing hypotheses, the profile likelihood ratio is defined as [200]:

$$\Lambda(\mu) = \frac{L(\mu, \hat{\theta})}{L(\hat{\mu}, \hat{\theta})}, \quad (5.5)$$

where  $\hat{\theta}$  in the numerator denotes the value of the nuisance parameters  $\theta$  that maximizes the likelihood  $L$  for a given value of signal strength  $\mu$  and is referred to as conditional ML estimator of  $\theta$ . For the likelihood in the denominator,  $\hat{\mu}$  and  $\hat{\theta}$  are the unconditional ML estimators of  $\mu$  and  $\theta$ , respectively. Thus, by definition  $\Lambda(\mu)$  takes values between 0 and 1. While  $\hat{\mu}$  can in principle also take negative value, it is assumed that  $\mu \geq 0$ , i. e. the signal is assumed to contribute only non-negatively.

A test statistic is defined by taking the negative logarithm of the profile likelihood ratio. Therefore, large value of the test statistic corresponds to a increasing incompatibility of the tested hypothesis with the observed data.

To test the discovery of a signal, the compatibility with the background-only hypothesis, i. e.  $\mu = 0$ , is evaluated as

$$t_{\mu=0} = \begin{cases} -2 \ln \Lambda(0) & \text{if } \hat{\mu} \geq 0, \\ 0 & \text{if } \hat{\mu} < 0, \end{cases} \quad (5.6)$$

where the truncation to zero for  $\hat{\mu} < 0$  ensures that a downward fluctuation of the data is not counted as evidence against the background-only hypothesis.

In the absence of a significant excess over the SM expectation, the agreement of the data with a signal of strength  $\mu$  is evaluated as

$$t_{\mu} = \begin{cases} -2 \ln \Lambda(\mu) & \text{if } \hat{\mu} \leq \mu, \\ 0 & \text{if } \hat{\mu} > \mu. \end{cases} \quad (5.7)$$

Different modifications of  $t_{\mu}$  can come into use as discussed in Ref. [200], but they yield qualitatively equivalent descriptions. By setting  $t_{\mu} = 0$  for values of  $\hat{\mu}$  larger than  $\mu$  an upward fluctuation of the data beyond the signal-plus-background prediction does not result in a false rejection of the hypothesis.

The  $p$ -value can be used to put the degree of incompatibility of a given hypothesis with the data into context. It describes the probability of obtaining a result at least as extreme as the one observed, under the assumption that the null hypothesis  $H_0$  is correct:

$$p_{H_0} = \int_{t_{\mu}^{obs.}}^{\infty} f(t_{\mu}|\mu) dt_{\mu}, \quad (5.8)$$

where  $t_{\mu}^{obs.}$  is the measured value of the test statistics given the observation and  $f(t_{\mu}|\mu)$  is the probability density function of  $t_{\mu}$  given the value  $\mu$  defined by  $H_0$ . The distribution of the test statistic is evaluated either by sampling pseudo-data for the given hypothesis or using the asymptotic formulae described in Ref. [200]. Hence, to compute the  $p$ -value for the signal-plus-background hypothesis,  $p_{s+b}$ , the test statistics  $t_{\mu}$  in Equation (5.7) is used. The  $p$ -value  $p_b$ , which measures the incompatibility with the background-only hypothesis, instead uses the test statistics  $t_{\mu=0}$  in Equation (5.6).

In high-energy physics, an observation of new physics is claimed if the excess in data above the SM expectation exceeds the significance threshold of  $5\sigma$ , expressed in terms of Gaussian standard deviations. The  $p$ -value for the rejection of the background-only hypothesis,  $p_b$ , is therefore converted into the significance  $Z$  via

$$Z = \Phi^{-1}(1 - p), \quad (5.9)$$

where  $\Phi^{-1}$  is the quantile (inverse of the cumulative distribution) of the unit Gaussian. Evidence for the presence of a new phenomena would be claimed if  $Z \geq 3$ .

The exclusion of a signal-plus-background hypothesis is expressed in terms of a confidence level (CL). To avoid false rejection of the hypothesis in case the signal expectation is small due to low sensitivity of the analysis, the  $\text{CL}_s$  technique [204] is used, which suppresses  $p_{s+b}$  by  $p_b$ :

$$\text{CL}_s = \frac{p_{s+b}}{p_b}, \quad (5.10)$$

where both  $p$ -values are computed using the exclusion test statistics  $t_\mu$ . A signal is excluded at 95 % CL if the  $\text{CL}_s$  value is below 0.05.

### 5.3 Fit setups

Depending on the problem, different ML fits to the data, implemented using the HIST-FITTER framework [124], are employed to fix the free parameters in the statistical model.

**Background-only fit:** Before the SRs can be unblinded, the background estimation strategy needs to be verified. Normalization factors  $\omega$  for the main background processes are extracted from a simultaneous fit in all CRs, which are designed to be approximately free of any signal contribution. The fit setup thus only includes the CRs and no signal ( $\mu = 0$ ), such that the total background in the CRs is determined by the observed data count. The resulting fitted background prediction is therefore independent of the observation in the VRs and SRs. The estimation strategy can be tested by comparing the fitted prediction to the observation in the VRs, while keeping the SRs blinded. The extrapolation of the fitted prediction of some background process  $p$  can be described via a transfer factor, which is equivalent to the normalization factor approach:

$$n_p^{\text{fit}}(\text{SR}) = \omega_p \times n_p^{\text{MC}}(\text{SR}) = \underbrace{\left[ \frac{n_p^{\text{MC}}(\text{SR})}{n_p^{\text{MC}}(\text{CR})} \right]}_{\text{Transfer factor}} \times n_p^{\text{fit}}(\text{CR}), \quad (5.11)$$

where  $n_p^{\text{fit}}$  and  $n_p^{\text{MC}}$  are the fitted and nominal MC event yields for a given selection. Systematic uncertainties affecting the overall normalization of a background process cancel as these effects are common in all regions. The complexity increases as more background processes, constrained in dedicated CRs which can also be binned, as well as contribution directly taken from MC without a normalization factor are added.

**Model-dependent signal fit:** In case no significant excess over the prediction of the background-only hypothesis is observed in the unblinded SRs, exclusion limits on a specific signal model are derived. CRs as well as SRs are used in this fit and potential signal contributions are taken into account in all the regions as predicted by the tested model, i. e. one fit is performed for each signal point with  $\mu = 1$ . Multiple SRs and/or a SR binned in a signal-sensitive observable can be used, which generally yields a better sensitivity. This way, the fit effectively gains separation power as the signals will generally feature a different shape over multiple bins or multiple SRs compared to the background.

**Model-independent signal fit:** To evaluate the significance of an excess over the background-only prediction ( $\mu = 0$ ) in a SR or to set model-independent limits on the number of beyond-SM events, a third fit strategy is employed. To ensure independence of the signal on a specific model, no assumption can be made on the modelling of the signal. The CRs are thus assumed to be free of any signal contamination and each SR is considered independently and can only have one single bin. The signal strength  $\mu$  can be scanned in discrete steps to derive upper limits on the number of potential signal events.



## 6 Signal regions

Signal regions (SRs) are constructed by placing cuts on several signal discriminating variables. The goal is to select as many potential signal events as possible while reducing the contribution from background processes with similar signatures.

Besides the available statistics, the maximal sensitivity of a selection to any signal is first and foremost limited by the cross section of the investigated signal process. For top-squark and  $LQ_3^{u/d}$  pair-production the cross sections fall off quickly with the mass of the particles produced in the  $pp$  collisions, as discussed in Sections 4.3.2 and 4.3.3. Furthermore, the decay products of the produced particles dictate the kinematics and multiplicities of reconstructed objects in the final state. For the stop-stau signal, for example, one could ideally cover all values of  $m(\tilde{\tau}_1)$  up to a certain  $m(\tilde{t}_1)$ . In the highly compressed scenario, where the mass-splitting  $\Delta m = m(\tilde{t}_1) - m(\tilde{\tau}_1)$  is close to zero, the difficulty in identifying the low- $p_T$   $b$ -jet makes it extremely challenging to distinguish signal from background, as early studies have shown. Thus two signal regions are designed, one targeting the low to medium, the other the high mass-splitting region.

This chapter describes the general optimization procedure and motivates the various discriminating variables used in the definition of the SRs.

### 6.1 General optimization strategy

Designing the SRs is one of the first steps in an analysis, as it is a prerequisite for the background estimation strategy. Thus, several approximations are necessary to estimate the sensitivity of any given SR candidate. A good measure for the sensitivity is given by the so-called Asimov significance [200, 205]:

$$Z_A = \left[ 2 \left( (s + b) \ln \left[ \frac{(s + b)(b + \sigma_b^2)}{b^2 + (s + b)\sigma_b^2} \right] - \frac{b^2}{\sigma_b^2} \ln \left[ 1 + \frac{\sigma_b^2 s}{b(b + \sigma_b^2)} \right] \right) \right]^{1/2}, \quad (6.1)$$

with the number of expected signal and background events  $s$  and  $b$  and the total background uncertainty  $\sigma_b$ . It is derived from a simplified likelihood describing a one-bin counting experiment with an uncertain background prediction using the principles described in Section 5.2. In addition to the statistical MC uncertainty, a flat uncorrelated systematic uncertainty of 30% is assumed for all background processes. This value is motivated by the total systematic uncertainty computed in the previous iteration of the stop-stau analysis [82].

Besides using N-1 plots, which show the effect of each individual cut in a given selection, a semi-automated scan of the signal-rich phase-space is conducted to identify SR candidates. A brute-force algorithm [206], based on the NUMPY package [207], is configured to scan a multitude of cut combinations for the highest Asimov significance. These combinations are generated from a list of variables and their associated list of lower or upper bounds as defined by the user. In order to retain a reliable MC background prediction in the SR, candidates are required to contain at least five raw events per background process. The scan is performed in multiple iterations and each time the discrimination power of the tested variables is studied, e.g. via N-1 plots. Those with weaker performance are neglected in the next run, while for those with a strong discrimination power, the granularity of the cuts is optimized, i.e. by adjusting the range of the cut values or decreasing the step size. Each time of the order of ten million combinations are tested and the set of variables is reduced if possible. The procedure is repeated until a SR candidate is found that yields the highest  $Z_A$ -value using as few cuts as possible.

In the following Section 6.2 and Section 6.3 the optimization procedure is described in detail for the SRs in the di-tau and single-tau channel, respectively. The performance of the more fundamental choices like the trigger strategy or identification working points of certain objects is assessed by rerunning the chain of scans each time.

## 6.2 Signal region in the di-tau channel

The di-tau SR is designed with the aim to yield the highest possible sensitivity to stop-stau models with small to medium mass-splitting. The optimization studies have been performed on events selected by the di-tau preselection cuts, given in Table 4.4, with the exception of the trigger choice, where a logical *or* of the  $E_T^{\text{miss}}$ , di-tau and di-tau+ $E_T^{\text{miss}}$  trigger is used instead. Sensitivity scans take into account the following event information, object multiplicities and kinematic variables:

- Either  $E_T^{\text{miss}}$ , di-tau or di-tau+ $E_T^{\text{miss}}$  trigger (including trigger-matching and plateau cuts)
- Multiplicity  $N$  of jets and  $b$ -tags
- An additional *Tight* identification requirement for the leading or subleading tau or both
- Transverse momentum  $p_T$  and transverse mass  $m_T$  of taus, jets and  $b$ -tagged jets
- The  $b$ -tagging identification score
- Angular ( $\Delta\phi/\Delta\eta$ ) and spatial separations ( $\Delta R$ ) between taus, jets and  $b$ -tagged jets
- The charge product of the two leading taus, described by  $OS(\tau_1, \tau_2)$

- $E_T^{\text{miss}}$ , its significance  $\mathcal{S}(E_T^{\text{miss}})$  and its angular and spatial separation to taus, jets and  $b$ -tagged jets
- Other high-level variables:  $m_{T2}(\tau_1, \tau_2)$ ,  $m(\tau_1, \tau_2)$ ,  $\Sigma m_T(\tau_1, \tau_2)$ ,  $m_{T2}(b_1, b_2)$ ,  $m(b_1, b_2)$ ,  $\Sigma m_T(b_1, b_2)$ ,  $\min_{i,j=1,2} m(\tau_i, b_j)$ ,  $s_T$  and  $\min_i \Delta\phi(j_i, E_T^{\text{miss}})$

Together with a list of appropriate cut values (lower and/or upper bounds) all possible cut combinations are scanned. For the computation of the  $Z_A$ -value the stop-stau signal point with  $m_{\tilde{t}_1} = 1250$  GeV and  $m_{\tilde{\tau}_1} = 790$  GeV is chosen as the benchmark point. The scan is repeated as described in Section 6.1 until a minimal set of cut combinations yielding the best overall sensitivity is found. Regarding the choice of trigger the best results have been achieved using the  $E_T^{\text{miss}}$  trigger. As will be discussed in Section 7.2, it is also well suited for the use in the control and validation regions, which is why it is included in the di-tau preselection shown in Table 4.4.

| Variable                 | Cut         |
|--------------------------|-------------|
| $OS(\tau_1, \tau_2)$     | $= 1$       |
| $E_T^{\text{miss}}$      | $> 280$ GeV |
| $m_{T2}(\tau_1, \tau_2)$ | $> 70$ GeV  |

**Table 6.1:** Definition of the di-tau SR. These cuts follow after the di-tau preselection cuts given in Table 4.4.

The full definition of the di-tau SR is given in Table 6.1. The separation power stems almost exclusively from the lower bound on  $m_{T2}(\tau_1, \tau_2)$  at 70 GeV. Raising the lower bound on  $E_T^{\text{miss}}$  to 280 GeV helps in selecting events with multiple highly energetic invisible particles. Since top squarks are only produced in pairs, tau pairs with opposite charges  $OS(\tau_1, \tau_2) = 1$  are expected for the signal.

Tightening the identification working point for one or both taus to *Tight* turned out to be counterproductive, as it limits the available statistics even further. On the other hand, loosening the  $b$ -tagging identification to a working point with 85% efficiency would in principle allow to tighten the cuts on other variables like  $m_{T2}(\tau_1, \tau_2)$ . However, compared to the nominal approach using the 77% efficiency working point, no significant sensitivity improvement was found.

In Table 6.2 the expected event yields for the individual backgrounds and the signal benchmark point are given. Here, the background normalization is taken directly from theory. The dominant source of background stems from top-quark pair-production.

The associated N-1 plots for the di-tau SR cuts are shown in Figure 6.1, demonstrating the signal separation power of each cut. In particular, the  $m_{T2}(\tau_1, \tau_2)$  distribution demonstrates nicely the desired background rejection, with top-related background processes bound from above approximately by the  $W$ -boson mass. Additional sources of  $E_T^{\text{miss}}$ , such as the neutrinos produced in the tau lepton decay, can lead to a shift or smearing of the end point. Note, that while these N-1 plots might suggest that even

|                                       |                 |
|---------------------------------------|-----------------|
| Total bkg.                            | $4.3 \pm 0.5$   |
| $t\bar{t}$ (1 real $\tau$ )           | $0.9 \pm 0.3$   |
| $t\bar{t}$ (2 real $\tau$ )           | $0.8 \pm 0.2$   |
| $t\bar{t} + V$                        | $0.61 \pm 0.09$ |
| Multiboson                            | $0.49 \pm 0.07$ |
| $t\bar{t}$ -fake                      | $0.5 \pm 0.3$   |
| $Z + \text{jets}$                     | $0.35 \pm 0.08$ |
| $t\bar{t} + H$                        | $0.28 \pm 0.02$ |
| Single top                            | $0.17 \pm 0.05$ |
| Other top                             | $0.12 \pm 0.05$ |
| $W + \text{jets}$                     | $0.1 \pm 0.2$   |
| $m(\tilde{t}_1) = 1250 \text{ GeV}$   | } $7.2 \pm 0.2$ |
| $m(\tilde{\tau}_1) = 790 \text{ GeV}$ |                 |

**Table 6.2:** Breakdown of the expected event yields in the di-tau SR with MC scaled to the integrated luminosity of  $139 \text{ fb}^{-1}$  measured in data. The uncertainties are statistical only and the normalization of the background yields is taken directly from theory.

tighter cuts can lead to a higher sensitivity, the consequent loss of MC statistics would make the background prediction much less reliable.

Signal-region candidates which employ a multi-binned approach have been studied, too. Due to the sharp cut-off in the  $m_{T2}(\tau_1, \tau_2)$  distribution of the background it is not possible to define a SR, binned in  $m_{T2}(\tau_1, \tau_2)$ , with sufficient background statistics in the highest bins. When choosing a different variable for the binning, the cut on  $m_{T2}(\tau_1, \tau_2)$  must be loosened, which significantly reduces the sensitivity, thereby negating any potential sensitivity gain obtained by a multi-bin approach.

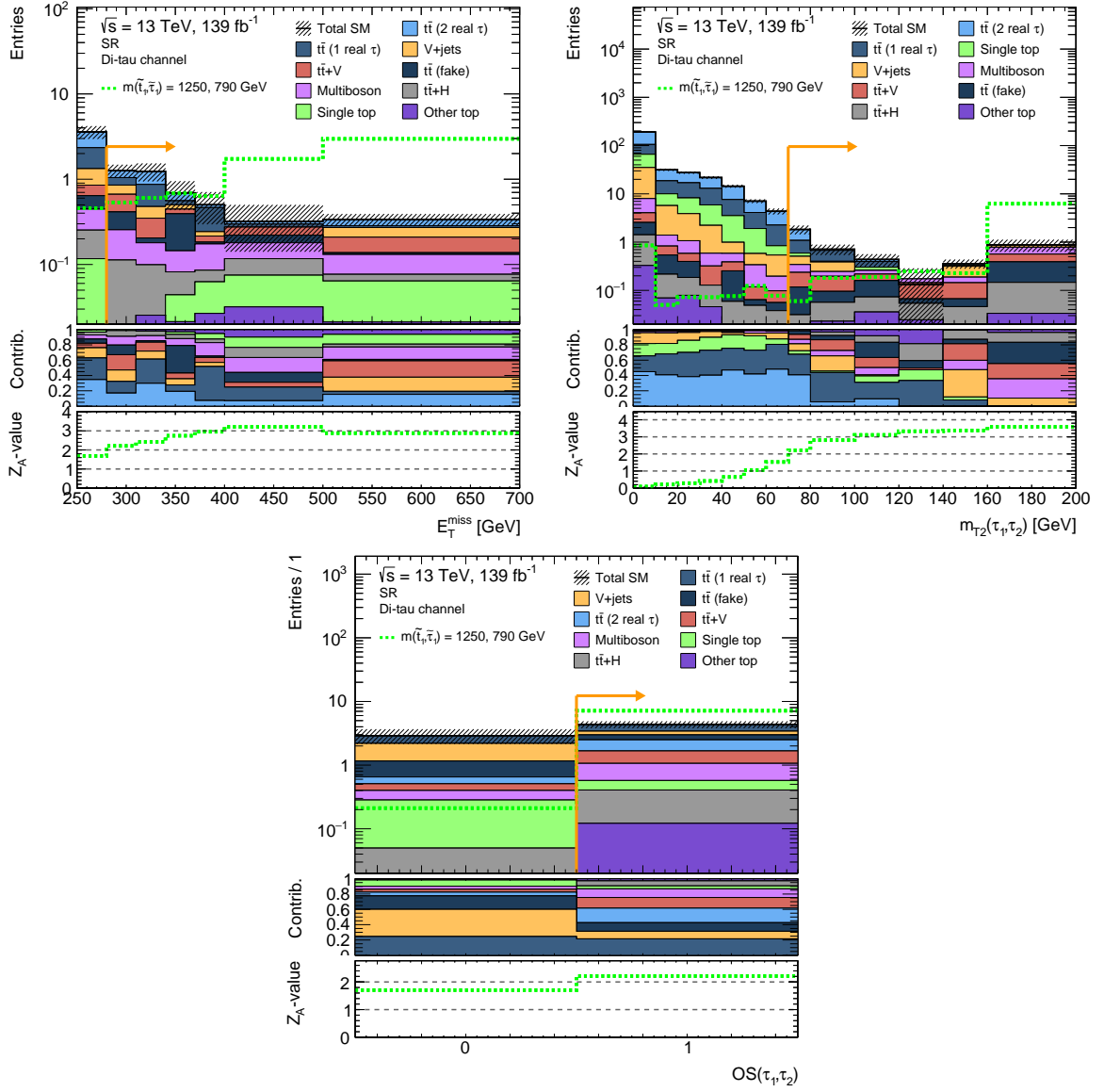


**Figure 6.1:** N-1 plots comparing the signal and background distributions for several kinematic variables after applying the di-tau SR cuts listed in Table 6.1 with the exception of the one shown on the plot. The orange vertical line shows the position of the cut used in the SR, where an arrow to the right denotes a lower bound. All MC yields are scaled to the integrated luminosity of  $139\text{fb}^{-1}$  measured in data. The lower pad in each plot shows the  $Z_A$ -significance for a lower bound placed at the lower edge of the given bin. The uncertainties are statistical only and the normalization of the background yields is taken directly from theory. The rightmost bin includes the overflowed events.

### 6.3 Signal regions in the single-tau channel

The aim of the single-tau SR is to extend the coverage of the stop-stau parameter space by targeting the region with high mass splitting. Together with the di-tau SR this allows for a maximal sensitivity across a wide range of  $m(\tilde{\tau}_1)$ . For higher mass splittings, more energy is distributed to the  $b$ -quark produced in the three-body decay of the stop, while the tau produced in the subsequent tau-slepton decay is expected to be softer, which lowers its probability to be correctly identified. On the other hand for  $LQ_3^{u/d}$  pair-production with  $\beta \sim 0.5$  the final state does look very similar to that of the high- $\Delta m$  stop-stau signal: Two high- $p_T$   $b$ -quarks are produced in all events and most commonly accompanied by exactly one tau. These similar final states present the opportunity to design a single-tau SR with high sensitivity to both the stop-stau and the  $LQ_3^{u/d}$  signal.

The optimization is performed for a SR with one bin. Again, scans are performed testing the separation power of the following quantities and subsets thereof:

- Either  $E_T^{\text{miss}}$  or single-tau trigger (including trigger-matching and plateau cuts)
- Multiplicity  $N$  of jets and  $b$ -tags
- An additional *Tight* identification requirement for the tau
- Transverse momentum  $p_T$  and transverse mass  $m_T$  of the tau, jets and  $b$ -tagged jets
- The  $b$ -tagging identification score
- Angular ( $\Delta\phi/\Delta\eta$ ) and spatial separations ( $\Delta R$ ) between the tau, jets and  $b$ -tagged jets
- $E_T^{\text{miss}}$ , its significance  $\mathcal{S}(E_T^{\text{miss}})$  and its angular ( $\Delta\phi/\Delta\eta$ ) and spatial separation ( $\Delta R$ ) to the tau, jets and  $b$ -tagged jets
- Other high-level variables:  $m_{T2}(b_1, b_2)$ ,  $m(b_1, b_2)$ ,  $\Sigma m_T(b_1, b_2)$ ,  $\min_{i=1,2} m(\tau, b_i)$   $s_T$  and  $\min_i \Delta\phi(j_i, E_T^{\text{miss}})$

The individual lists of cut values for each variable are refined after every iteration of the scan and variables with subpar discrimination power are discarded. For the stop-stau signal, the parameters  $m_{\tilde{t}_1} = 1050$  GeV and  $m_{\tilde{\tau}_1} = 190$  GeV are chosen as the benchmark. This yields a relatively large set of potential SR candidates with significances close to the maximum. From this, the one which maximizes the sensitivity to the  $LQ_3^{u/d}$  signal with  $m(LQ_3^{u/d}) = 1000$  GeV and  $\beta = 0.5$  is chosen and given in Table 6.3.

The  $N_{b\text{-tag}} \geq 2$  requirement, which has been incorporated into the single-tau preselection definition given in Table 4.4, together with the lower bounds on  $\Sigma m_T(b_1, b_2)$  and  $s_T$  are very efficient in selecting the high- $p_T$  hadronic objects in the signal events, predominantly originating from the two  $b$ -quarks. For both the high- $\Delta m$  stop-stau and the  $LQ_3^{u/d}$  signal the dominant source of  $E_T^{\text{miss}}$  does not originate from the decay the

| Variable               | One-bin SR          | Multi-bin SR                                   |
|------------------------|---------------------|--|
| $E_T^{\text{miss}}$    | $> 280 \text{ GeV}$ | $> 280 \text{ GeV}$                            |
| $\Sigma m_T(b_1, b_2)$ | $> 700 \text{ GeV}$ | $> 700 \text{ GeV}$                            |
| $m_T(\tau)$            | $> 300 \text{ GeV}$ | $> 150 \text{ GeV}$                            |
| $s_T$                  | $> 800 \text{ GeV}$ | $> 600 \text{ GeV}$                            |
| $p_T(\tau)$ bins       |                     | [50, 100] GeV,<br>[100, 200] GeV,<br>> 200 GeV |

**Table 6.3:** Definition of the one-bin and multi-bin SR in the single-tau channel. For the model-dependent signal fit, a multi-bin approach in  $p_T(\tau)$  is used. These cuts follow after the single-tau preselection cuts given in Table 4.4. Note that the tighter cuts on  $m_T(\tau)$ ,  $s_T$  and  $E_T^{\text{miss}}$  mean that the one-bin SR is a subset of the multi-bin SR.

tau is produced in. Thus a fairly high lower bound on  $m_T(\tau)$  at 300 GeV can be used to efficiently reduce the contribution from background processes where the opposite is the case, i. e. those involving  $W$ -boson decays.

The expected event yields for the simulated backgrounds and signal benchmark points in the one-bin SR are given in Table 6.4. Again, the background normalization is taken directly from theory. The signal separation power of each cut is shown Figure 6.2, also highlighting the similarities of the high- $\Delta m$  stop-stau and  $\text{LQ}_3^{\text{u/d}}$  signal kinematics.

While the stop-stau and  $\text{LQ}_3^{\text{u/d}}$  benchmark points feature a very similar shape in the jet and  $b$ -jet related kinematic distributions, they differ with respect to the tau's transverse momentum: Stop-stau signals with high mass-splitting yield relatively soft taus, while in comparison the taus produced in  $\text{LQ}_3^{\text{u/d}}$  decays, with  $m(\text{LQ}_3^{\text{u/d}}) \sim 1 \text{ TeV}$ , are much harder. Therefore, a multi-bin fit in  $p_T(\tau)$  can be used to increase the potential exclusion reach. In order to ensure sufficient background statistics in the individual bins of this multi-bin SR the cuts on  $m_T(\tau)$  and  $s_T$  need to be lowered with respect to the ones used in the one-bin SR as shown in Table 6.3. The first and second bin in  $p_T(\tau)$  ranges from 50 to 100 GeV and 100 to 200 GeV, respectively, while the last bin includes events with  $p_T(\tau) > 200 \text{ GeV}$ . The loosened cuts, the variable used for the binning and the individual bin ranges have been optimized following the same procedure as before, i. e. maximizing the  $Z_A$ -value per bin while retaining sufficient background MC statistics.

The expected event yields for the simulated backgrounds and signal benchmark points in each of the three  $p_T(\tau)$  bins are given in Table 6.4. Overall, the background composition is very similar to the one-bin SR given in Table 6.4. The signal separation power of the loosened cuts in the multi-bin SR is shown in Figure 6.3, also highlighting the different  $p_T(\tau)$  shapes of the high- $\Delta m$  stop-stau and  $\text{LQ}_3^{\text{u/d}}$  signals. Note that the position of the cuts in the N-1 plots appear to be too loose, as the plots include all three  $p_T(\tau)$  bins.

|                               | Single-tau SR<br>(one-bin) | Single-tau SR<br>(binned in $p_T(\tau)$ ) |                |               |
|-------------------------------|----------------------------|---|----------------|---------------|
|                               |                            | [50, 100] GeV                             | [100, 200] GeV | > 200 GeV     |
| Total bkg.                    | 5.2 ± 0.4                  | 14.7 ± 0.9                                | 8.1 ± 0.6      | 4.7 ± 0.5     |
| Single top                    | 2.2 ± 0.3                  | 4.7 ± 0.6                                 | 3.0 ± 0.4      | 3.2 ± 0.4     |
| $t\bar{t}$ (1 real $\tau$ )   | 1.4 ± 0.2                  | 5.6 ± 0.6                                 | 3.1 ± 0.4      | 0.8 ± 0.2     |
| $t\bar{t}$ -fake              | 0.7 ± 0.1                  | 2.8 ± 0.3                                 | 0.6 ± 0.1      | 0.18 ± 0.06   |
| $W$ +jets                     | 0.3 ± 0.1                  | 0.3 ± 0.1                                 | 0.6 ± 0.3      | 0.4 ± 0.2     |
| $t\bar{t} + V$                | 0.24 ± 0.07                | 0.7 ± 0.1                                 | 0.31 ± 0.09    | 0.09 ± 0.06   |
| $Z$ +jets                     | 0.19 ± 0.09                | 0.3 ± 0.1                                 | 0.04 ± 0.02    | 0.10 ± 0.09   |
| Multiboson                    | 0.08 ± 0.04                | 0.16 ± 0.07                               | 0.11 ± 0.03    | 0.03 ± 0.01   |
| Other top                     | 0.04 ± 0.02                | 0.10 ± 0.02                               | 0.09 ± 0.03    | 0.012 ± 0.008 |
| $t\bar{t} + H$                | 0.040 ± 0.008              | 0.10 ± 0.01                               | 0.06 ± 0.01    | 0.028 ± 0.008 |
| $m(\tilde{t}_1) = 1050$ GeV   | 11.0 ± 0.5                 | 8.9 ± 0.5                                 | 11.4 ± 0.5     | 6.6 ± 0.4     |
| $m(\tilde{\tau}_1) = 190$ GeV |                            |   |                |               |
| $m(\text{LQ}_3^u) = 1$ TeV    | 15.8 ± 0.4                 | 2.4 ± 0.2                                 | 6.8 ± 0.3      | 17.7 ± 0.5    |
| $m(\text{LQ}_3^d) = 1$ TeV    | 18.1 ± 0.6                 | 1.4 ± 0.2                                 | 6.5 ± 0.4      | 19.9 ± 0.7    |

**Table 6.4:** Breakdown of the expected event yields in the single-tau one-bin SR and the three  $p_T(\tau)$  bins in the single-tau multi-bin SR with MC scaled to the integrated luminosity of  $139 \text{ fb}^{-1}$  measured in data. The uncertainties are statistical only and the normalization of the background yields is taken directly from theory.

The expected exclusion reach of the one-bin and multi-bin SR has been compared using a simplified version of the fit setup described in Section 5.3, where again a flat uncorrelated systematic uncertainty of 30% is assumed for all background processes. For the  $\text{LQ}_3^{u/d}$  signal, the binned approach results in an expected gain of about 50 GeV in  $m(\text{LQ}_3^{u/d})$  for the targeted  $\beta \sim 0.5$  regime. For the high- $\Delta m$  stop-stau signal, no significant gain in the exclusion reach is found, with only a slight improvement observed for larger values of  $\Delta m$  which are, however, already well covered by the di-tau SR.

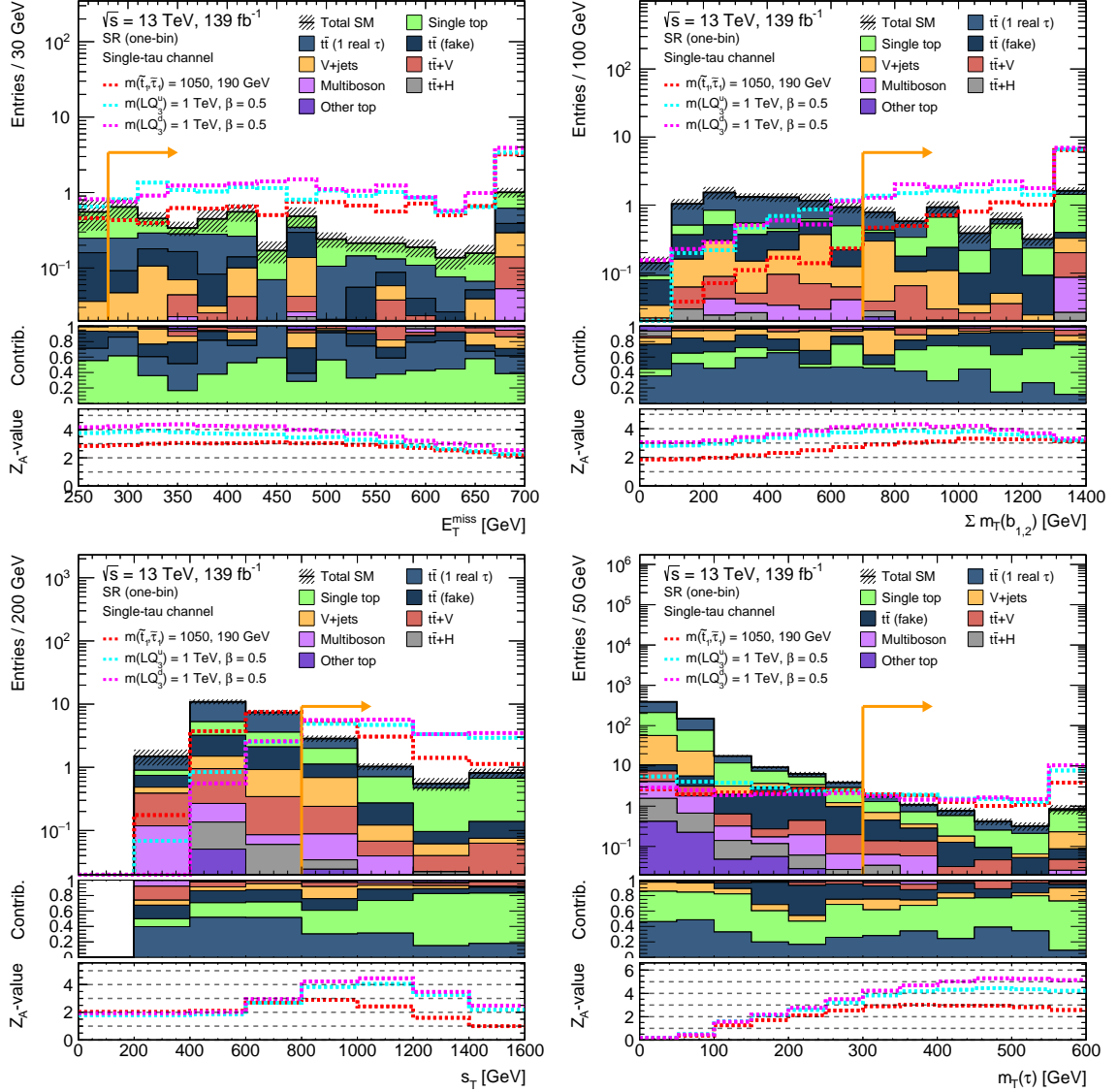


**Figure 6.2:** N-1 plots comparing the signal and background distributions for several kinematic variables after applying the single-tau one-bin SR cuts listed in Table 6.3 with the exception of the one shown on the plot. The orange vertical line shows the position of the cut used in the SR, where an arrow to the right denotes a lower bound. All MC yields are scaled to the integrated luminosity of  $139 \text{ fb}^{-1}$  measured in data. The lower pad in each plot shows the  $Z_A$ -significance for a lower bound placed at the lower edge of the given bin. The uncertainties are statistical only and the normalization of the background yields is taken directly from theory. The rightmost bin includes the overflowed events.

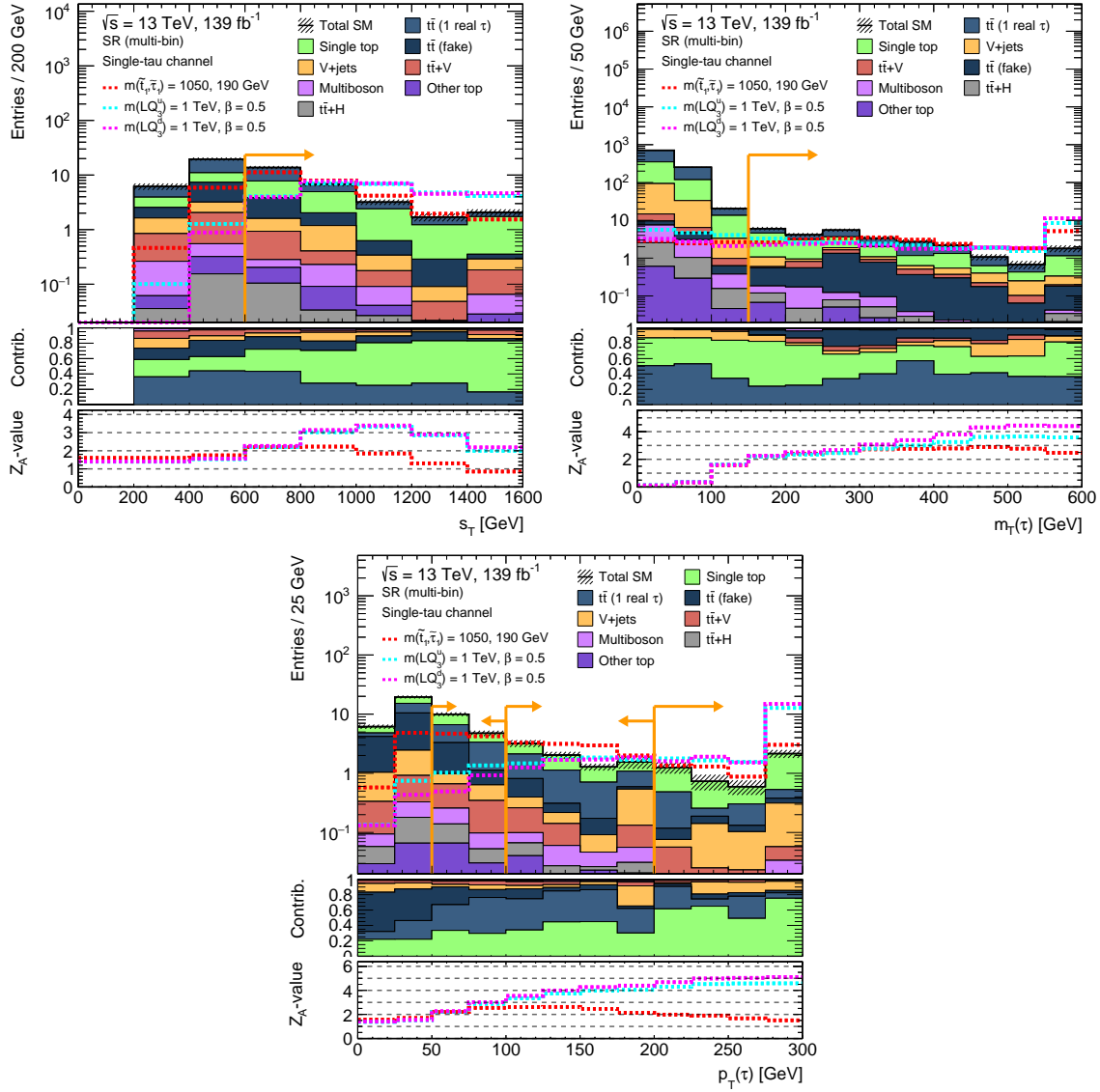


**Figure 6.3:** N-1 plots comparing the signal and background distributions for several kinematic variables after applying the single-tau multi-bin SR cuts listed in Table 6.3 with the exception of the one shown on the plot. Only the variables for which the cuts were loosened with respect to the single-tau one-bin SR are shown. The selection includes all three  $p_T(\tau)$  bins, which means that the N-1 plots for the other variables give the misleading impression, that the chosen cuts appear to be too loose. The orange vertical line shows the position of the cut used in the SR, where an arrow to the left or right denotes an upper or lower bound, respectively. All MC yields are scaled to the integrated luminosity of  $139 \text{ fb}^{-1}$  measured in data. The lower pad in each plot shows the  $Z_A$ -significance for a lower bound placed at the lower edge of the given bin. The uncertainties are statistical only and the normalization of the background yields is taken directly from theory. The rightmost bin includes the overflowed events.

# 7 Background estimation and validation

The final states targeted by the signal regions (SRs) feature one or more taus,  $b$ -jets and significant missing transverse momentum. Production of  $t\bar{t}$  pairs constitutes the dominant irreducible background in the di-tau SR and the second-most contributing background in the single-tau SRs. In the latter the production of a single top quark in association with a  $W$  boson takes the lead. Control regions (CRs) for these backgrounds are defined in order to derive normalization factors for the MC estimates by fitting them to the observed data as explained in Section 5.3. These regions are designed to be enriched with a given background process and feature a negligible signal contamination. The normalization is then compared to data in validation regions (VRs) to ensure that the extrapolation to the SRs is working. The VRs are therefore placed a phase-space between the CRs and SRs and all regions are required to be pair-wise disjoint to ensure statistical independence. In order to assess the modelling of the fully tauonic and semi-tauonic decays of the  $t\bar{t}$  pairs in MC separately, dedicated CRs and VRs are defined for the  $t\bar{t}$  (2 real  $\tau$ ) and  $t\bar{t}$  (1 real  $\tau$ ) process. Subdominant background processes are predicted from simulation only, as their contributions are too small to find suitable control and validation regions for them.

The layout of the CRs and VRs is discussed in Sections 7.1 and 7.2 for the di-tau and single-tau channel, respectively.

## 7.1 Control and validation regions in the di-tau channel

A set of two control and validation regions is defined for the di-tau channel in order to normalize the two major background processes in the di-tau SR,  $t\bar{t}$  (2 real  $\tau$ ) and  $t\bar{t}$  (1 real  $\tau$ ). As the  $m_{T2}(\tau_1, \tau_2)$  variable is used to separate SM backgrounds involving  $W$ -boson decays from the stop-stau signal, the cut is inverted for the  $t\bar{t}$  CRs and VRs. A cut at 35 GeV separates the two, allowing for sufficient statistics in any of the regions while placing the VRs close to the SR. The contribution from  $Z \rightarrow \tau\tau$  in the CRs with one or more  $b$ -tagged jets, produced by gluon-splitting, is sufficiently suppressed by placing a lower bound on the invariant mass of the leading and subleading tau at 50 GeV. In the VRs, however, the lower bound on  $m_{T2}(\tau_1, \tau_2)$  already sufficiently reduces the contribution from  $Z$ -boson production.

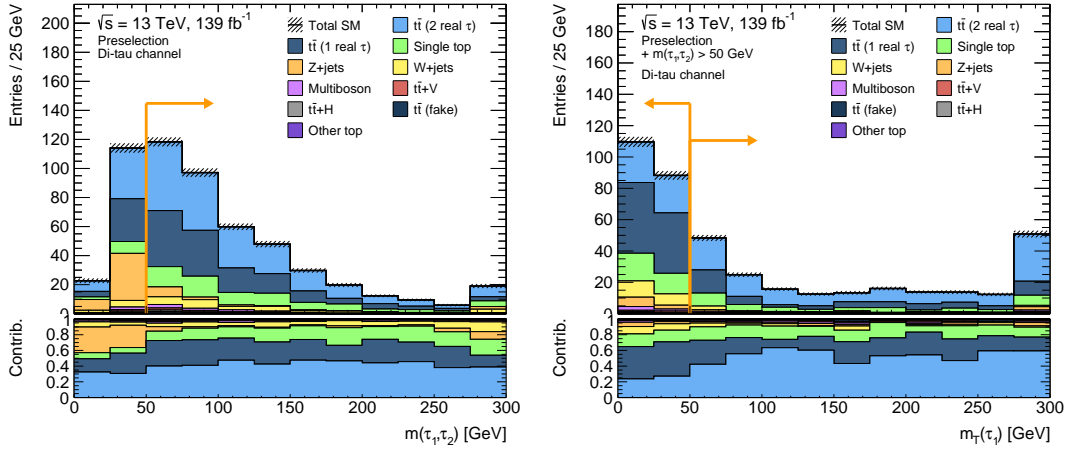


**Figure 7.1:** Distributions of  $m(\tau_1, \tau_2)$  and  $m_T(\tau_1)$  (+  $Z$ -veto) at di-tau preselection-level. The orange vertical line in the left plot at 50 GeV represents the cut used to suppress the  $Z$  + jets contribution in the di-tau CRs. The vertical line in the right plot demonstrates the separation of the  $t\bar{t}$  (1 real  $\tau$ ) and  $t\bar{t}$  (2 real  $\tau$ ) background at 50 GeV, i. e. approximately at the  $W$ -boson mass as explained in the text. The additional cuts on  $m_{T2}(\tau_1, \tau_2)$  and  $OS(\tau_1, \tau_2)$  used for the di-tau CRs and VRs (cf. Table 7.1) are not applied here. All MC yields are scaled to the integrated luminosity of  $139 \text{ fb}^{-1}$  measured in data. The uncertainties are statistical only and the normalization of the background yields is taken directly from theory.

The next step is then to separate the semi-tauonic  $t\bar{t}$  decay from the fully tauonic mode. In the former case, for about three quarters of the events at preselection level the leading tau is real. As the main source of  $E_T^{\text{miss}}$  in such an event stems from the neutrino of the  $W$ -boson decay producing the real tau, the  $m_T(\tau_1)$  variable is expected to feature a cut-off near  $m(W)$ . On the other hand, for fully tauonic  $t\bar{t}$  decays there are two neutrinos constituting  $E_T^{\text{miss}}$ . The neutrino associated to the leading tau contributes less, and due to the back-to-back topology of the  $t\bar{t}$  pair  $E_T^{\text{miss}}$  will predominantly point

| Variable                 | Control regions             |                             | Validation regions          |                             |
|--------------------------|-----------------------------|-----------------------------|-----------------------------|-----------------------------|
|                          | $t\bar{t}$ (2 real $\tau$ ) | $t\bar{t}$ (1 real $\tau$ ) | $t\bar{t}$ (2 real $\tau$ ) | $t\bar{t}$ (1 real $\tau$ ) |
| $OS(\tau_1, \tau_2)$     | = 1                         |                             | = 1                         |                             |
| $m_{T2}(\tau_1, \tau_2)$ | < 35 GeV                    | < 35 GeV                    | [35, 70] GeV                | [35, 70] GeV                |
| $m(\tau_1, \tau_2)$      | > 50 GeV                    | > 50 GeV                    |                             |                             |
| $m_T(\tau_1)$            | > 50 GeV                    | < 50 GeV                    | > 70 GeV                    | < 70 GeV                    |

**Table 7.1:** Definitions of the  $t\bar{t}$  control and validation regions in the di-tau channel. An empty cell signifies that no requirement on the given variable is applied, while brackets indicate an allowed range for the variable. These cuts follow after the di-tau preselection cuts given in Table 4.4.

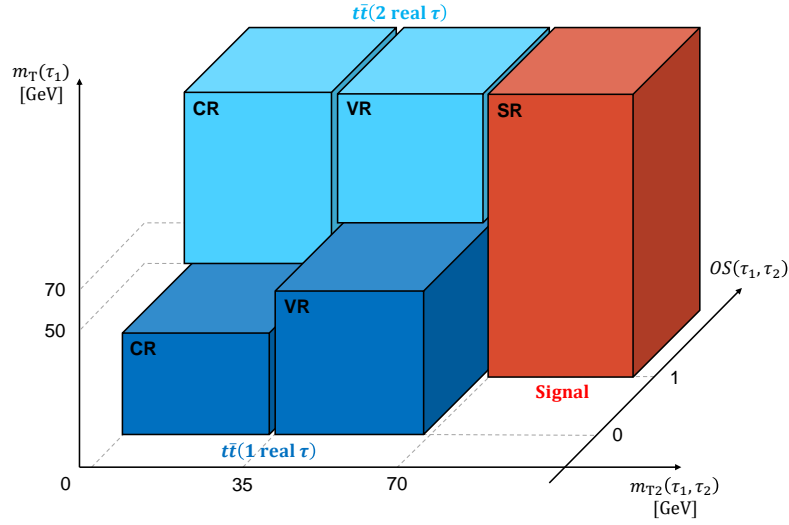


**Figure 7.2:** Layout of the control, validation and signal regions in the di-tau channel in the phase-space spanned by  $m_{T2}(\tau_1, \tau_2)$ ,  $m_T(\tau_1)$  and  $OS(\tau_1, \tau_2)$ . The additional  $E_T^{\text{miss}} > 280$  GeV requirement for the SR as well as the  $m(\tau_1, \tau_2) > 50$  GeV cut used for the CRs is not shown. The complete definition is given in Table 7.1.

in the opposite direction of the leading tau. The transverse mass  $m_T(\tau_1)$  is thus not bounded from above for  $t\bar{t}$  (2 real  $\tau$ ) events. A cut on  $m_T(\tau_1)$  at 50 GeV separates the  $t\bar{t}$  (2 real  $\tau$ ) and  $t\bar{t}$  (1 real  $\tau$ ) CRs, while for the respective VRs this value is slightly increased to 70 GeV. Additionally, an opposite-charge requirement,  $OS(\tau_1, \tau_2) = 1$ , for the leading and subleading tau is used to improve the purity of the  $t\bar{t}$  (2 real  $\tau$ ) CR and VR. The effect of the  $Z$ -veto and the separation of the  $t\bar{t}$  (2 real  $\tau$ ) and  $t\bar{t}$  (1 real  $\tau$ ) background in  $m_T(\tau_1)$  is illustrated in Figure 7.1.

A summary of the CR and VR definitions in the di-tau channel is given in Table 7.1. In Figure 7.2 the layout of all regions in the di-tau channel is depicted in the phase space spanned by  $m_{T2}(\tau_1, \tau_2)$ ,  $m_T(\tau_1)$  and  $OS(\tau_1, \tau_2)$ .

In order to avoid biasing the normalization and validation of the background prediction by accidentally selecting a significant amount of signal events in the CRs and VRs, the signal contamination is checked for both the stop-stau and  $LQ_3^{u/d}$  grid. Overall, the contribution from signal points, which have not yet been excluded, is at a negligible level.

## 7.2 Control and validation regions in the single-tau channel

The single-tau SR is dominated by  $t\bar{t}$  (1 real  $\tau$ ) and single-top contributions. While the  $t\bar{t}$  (1 real  $\tau$ ) background is already normalized in the CR in the di-tau channel,

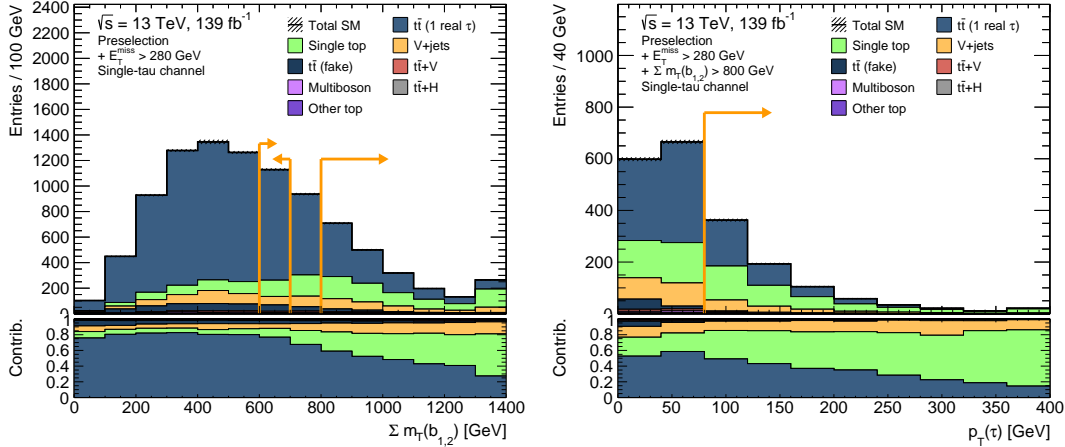


**Figure 7.3:** Distributions of  $\Sigma m_T(b_1, b_2)$  and  $p_T(\tau)$  ( $+\Sigma m_T(b_1, b_2) > 800$  GeV) at single-tau preselection-level with the lower bound on  $E_T^{\text{miss}}$  increased to 280 GeV. The first two vertical lines in the left plot represent the  $\Sigma m_T(b_1, b_2) \in [600, 700]$  GeV interval where the  $t\bar{t}$  (1 real  $\tau$ ) CR and VR of the single-tau channel are located. The third line in the  $\Sigma m_T(b_1, b_2)$ , and the line in the  $p_T(\tau)$  distribution demonstrate the lower bound at 800 GeV and 80 GeV, respectively, used in the definition of the single-top CR and VR. The additional cuts on  $s_T$  and  $m_T(\tau)$  used in the definition of the CRs and VRs (cf. Table 7.2) are not applied here. All MC yields are scaled to the integrated luminosity of  $139 \text{ fb}^{-1}$  measured in data. The uncertainties are statistical only and the normalization of the background yields is taken directly from theory.

an additional pair of control and validation regions in the single-tau channel is used to further constrain the normalization and validate the extrapolation to the single-tau SR.

The single-top control and validation regions are situated in the low- $m_T(\tau)$  regime: For

| Variable               | Control regions             |             | Validation regions          |                 |
|------------------------|-----------------------------|-------------|-----------------------------|-----------------|
|                        | $t\bar{t}$ (1 real $\tau$ ) | Single top  | $t\bar{t}$ (1 real $\tau$ ) | Single top      |
| $E_T^{\text{miss}}$    | $> 280$ GeV                 | $> 280$ GeV | $> 280$ GeV                 | $> 280$ GeV     |
| $s_T$                  | $[500, 600]$ GeV            |             | $> 600$ GeV                 |                 |
| $\Sigma m_T(b_1, b_2)$ | $[600, 700]$ GeV            | $> 800$ GeV | $[600, 700]$ GeV            | $> 800$ GeV     |
| $m_T(\tau)$            |                             | $< 50$ GeV  |                             | $[50, 150]$ GeV |
| $p_T(\tau)$            |                             | $> 80$ GeV  |                             | $> 80$ GeV      |

**Table 7.2:** Definitions of the  $t\bar{t}$  (1 real  $\tau$ ) and single-top control and validation regions in the single-tau channel. An empty cell signifies that no requirement on the given variable is applied, while brackets indicate an allowed range for the variable. These cuts follow after the single-tau preselection cuts given in Table 4.4.

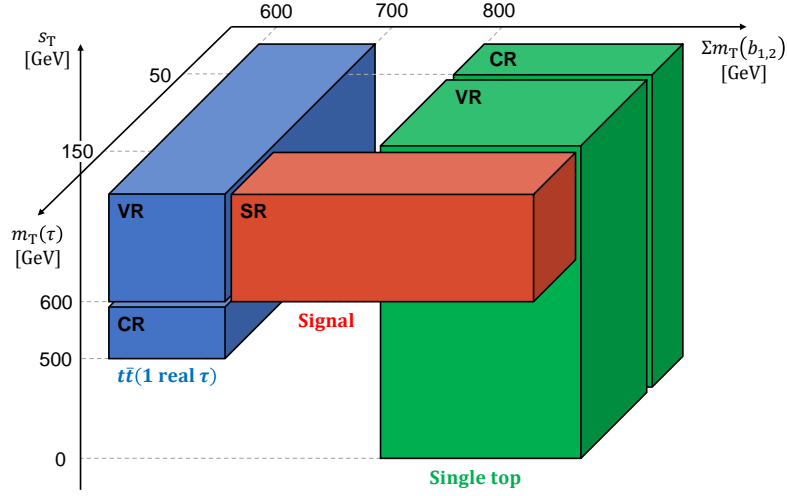


**Figure 7.4:** Layout of the control, validation and signal regions in the single-tau channel in the phase-space spanned by  $\Sigma m_T(b_1, b_2)$ ,  $m_T(\tau)$  and  $s_T$ . The additional  $E_T^{\text{miss}} > 280$  GeV requirement for all regions as well as the  $p_T(\tau) > 80$  GeV cut used for the single-top CR and VR is not shown. The complete definition is given in Table 7.2.

the CR, an upper bound on  $m_T(\tau)$  at 50 GeV is placed, while the VR is located between 50 GeV and 150 GeV. Additionally, a lower bound on  $p_T(\tau)$  is placed at 80 GeV for the CR and VR, while no requirement is made for  $s_T$ . Compared to the SR, the lower bound on  $\Sigma m_T(b_1, b_2)$  is slightly raised to 800 GeV to increase the purity.

The  $t\bar{t}$  (1 real  $\tau$ ) control and validation regions are placed in a window in  $\Sigma m_T(b_1, b_2)$  between 600 GeV and 700 GeV adjacent to the SR. The CR then covers the  $500 \text{ GeV} < s_T < 600 \text{ GeV}$  range and the VR values above 600 GeV. No constraint on  $m_T(\tau)$  is made for either of the regions.

Figure 7.3 illustrates the effects of the cuts on  $\Sigma m_T(b_1, b_2)$  and  $p_T(\tau)$ . For both variables, the single-top background contribution increases in the tail of the distribution. While a lower bound on  $\Sigma m_T(b_1, b_2)$  does not increase purity of the  $t\bar{t}$  (1 real  $\tau$ ) CR, it brings the region kinematically closer to the SR and reduces the event count such that it has similar statistics as the other CRs and therefore does not dominate in the fit. The lower bound on  $s_T$  at 500 GeV follows the same reasoning.

All control and validation regions in the single-tau channel feature the same  $E_T^{\text{miss}} > 280$  GeV requirement as the SR. A summary of the definitions is given in Table 7.2. The layout of the regions in the single-tau channel with respect to the phase space spanned by  $\Sigma m_T(b_1, b_2)$ ,  $m_T(\tau)$  and  $s_T$  is depicted in Figure 7.4.

The control and validation regions in the single-tau channel have also been checked for contamination from stop-stau and  $LQ_3^{u/d}$  signals, and the contribution from so far not excluded signal points was found to be negligible.

| Process                     | CR $t\bar{t}$ (2 real $\tau$ ) | CR $t\bar{t}$ (1 real $\tau$ ) | CR $t\bar{t}$ (1 real $\tau$ ) | CR single top  |
|-----------------------------|--------------------------------|--------------------------------|--------------------------------|----------------|
|                             | (di-tau channel)               |                                | (single-tau channel)           |                |
| $t\bar{t}$ (2 real $\tau$ ) | Fitted (56.0%)                 | Fitted (31.0%)                 | —                              | —              |
| $t\bar{t}$ (1 real $\tau$ ) | Fitted (20.6%)                 | Fitted (36.1%)                 | Fitted (81.3%)                 | Fitted (41.9%) |
| Single top                  | Fitted (15.4%)                 | Fitted (15.6%)                 | Fitted (9.4%)                  | Fitted (42.9%) |

**Table 7.3:** Overview of the fit setup used to derive the normalized background estimates. Three independent normalization factors are used. The numbers in brackets list the contribution of a given process in each CR evaluated with respect to the nominal MC prediction. For all other background processes the normalization is fixed to the nominal MC prediction.

Lastly, Table 7.3 summarizes the strategy for the background estimation. It shows the CRs used in the simultaneous fit of the three main background MC predictions to data. The relative contribution of each process in a given CR is given by the value in the brackets. For the  $t\bar{t}$  (2 real  $\tau$ ) process, only the two CRs in the di-tau channel are used in the fit, as its contribution in the single-tau channel is zero by construction. Two dedicated CRs exist for the normalization of the  $t\bar{t}$  (1 real  $\tau$ ) background, one in each channel. Since this can in principle lead to an over-constraining of fit parameters, an alternative setup with a separate normalization factor for each channel has also been studied. Compared to the nominal approach, the nominal value of the fitted background prediction remains virtually unchanged across all regions, but the total background uncertainty increases especially in the di-tau channel. As no strong over-constraining was observed in the nominal fit setup, the alternative approach is discarded.

# 8 Systematic uncertainties

Besides uncertainties originating from limited data and MC sample sizes, the analysis considers several sources of systematic uncertainties, grouped into experimental and theoretical uncertainties, described in the following. The complete set of systematic uncertainties is included as individual nuisance parameters in the background-only and exclusion fits. Their impact on the fitted background prediction in the SRs is studied in Section 8.3.

## 8.1 Experimental systematic uncertainties

Experimental uncertainties related to the detector response and event reconstruction are evaluated by the combined performance groups of the ATLAS collaboration and the variations are provided centrally for all MC samples. Uncertainties on the reconstruction and identification efficiency of physics objects are propagated to the expected yields by applying dedicated event weights. For uncertainties on the calibration and reconstruction parameters, the object and event selection is repeated for varied samples, i. e. auxiliary MC datasets where the given parameter has been varied up or down by one standard deviation compared to the nominal value. Some uncertainties depend on the fidelity of the detectors simulation. All MC background samples use the full detector simulation, while for signal samples the fast detector simulation ATLFAST-II is used.

In the statistical model, nuisance parameters related to experimental uncertainties are assumed to be correlated across all processes and regions.

### 8.1.1 Jets

Uncertainties on the jet energy scale (JES) and resolution (JER) are considered [208, 209]. They encompass uncertainties on the  $\eta$  and  $p_T$  dependence, in-situ calibrations, pile-up condition, detector noise, disparities between data and MC simulation as well as the composition of and calorimeter response to different jet flavors. A reduced set of nuisance parameters for JES and JER uncertainties is used: Components with small correlations are combined into single nuisance parameters to reduce the complexity of the analysis [210]. Additional uncertainties are provided for high- $p_T$  jets that are not fully contained in the calorimeter, referred to as punch-through jets, and on the

efficiency of the jet vertex tagger (JVT) [178].

The  $b$ -tagging performance constitutes an additional source of uncertainty [180, 211]. Dedicated nuisance parameter account for the uncertainties on the  $b$ -tagging efficiency, the rejection of charm and light-flavor jets as well as the extrapolation to high- $p_T$  regimes [212, 213].

### 8.1.2 Electrons and muons

For electrons, uncertainties on the energy scale and resolution are considered [183, 214]. Uncertainties associated with muons arise from the limited resolution of ID and MS tracks as well as charge-agnostic and charge-dependent corrections to the momentum scale [184, 215]. As light leptons are vetoed in the analysis, weight-based uncertainties on the reconstruction, isolation and identification efficiencies do not contribute.

### 8.1.3 Taus

Systematic uncertainties related to the reconstruction and identification efficiencies of taus are applied. Furthermore, tau energy scale uncertainties as well as statistical and systematic sources of uncertainty on the electron rejection are considered [186, 188, 189].

### 8.1.4 Missing transverse momentum

As  $E_T^{\text{miss}}$  is determined by the transverse momenta of the physics objects in the event, it is recalculated for all their systematic variations. Additional uncertainties on the scale and resolution of  $E_T^{\text{miss}}$  arise from the soft-term contributions [193, 216], described in Section 4.4.8.

### 8.1.5 Luminosity and pile-up reweighting

The relative uncertainty on the combined 2015–2018 integrated luminosity amounts to 1.7% [217], as determined by the primary luminosity measurements described in Section 3.2.4. This uncertainty is not assigned to the background processes that are normalized to data. An additional uncertainty is considered for the reweighting of the pile-up distribution in simulation to the one observed in data.

## 8.2 Theory uncertainties

Theory uncertainties consist of uncertainties related to the MC generator modelling and those related to the computation of the total cross section for a given process. In Section 8.2.1 the various sources of theory-related systematic uncertainties are explained and the approaches used to quantify their impact on the analysis are described. Sections 8.2.2 and 8.2.3 then summarize the theory-related uncertainties considered for the background processes and the signal models, respectively.

In the fits, the nuisance parameters for the theory uncertainties are assumed to be correlated across all regions but uncorrelated across processes.

### 8.2.1 Sources of theory uncertainties

The calculation of the matrix element (ME) and subsequent simulation of the parton-showering is implemented with a limited precision in the MC generators. By either comparing different generators or varying internal parameters, uncertainties on various aspects of the simulation are evaluated for the individual background and signal predictions and for each region of the analysis. Additionally, uncertainties on the PDF set and on the measurement of  $\alpha_S$  are considered.

In the following, the various sources of theory-related systematic uncertainty considered in the analysis are summarized:

**PDF and  $\alpha_S$  uncertainties:** Several sources of uncertainty enter the computation of the PDFs used in the MC calculation: Experimental uncertainties entering the datasets as well as the uncertainty on the functional form and flavor scheme used in the PDF fits. A set of 100 variations of the NNPDF3.0NNLO PDF set [143] is compared to the nominal value. Following the recommendations in Ref. [218], the relative PDF uncertainty  $\delta_{\text{PDF}}$  is evaluated as the root mean square of the deviations in the expected event yields:

$$\delta_{\text{PDF}} \cdot N_0 = \sqrt{\frac{1}{100} \sum_{i=1}^{100} (N_i - N_0)^2} \quad (8.1)$$

where  $N_0$  and  $N_i$  are the event yields for nominal and varied weights, respectively. Experimental errors and the fact that the renormalization group equation is truncated at a fixed order in perturbation theory additionally lead to an uncertainty on the strong coupling constant  $\alpha_S$ . By varying the nominal value  $\alpha = 0.118$  by  $\pm 0.001$ , the uncertainty is computed as

$$\delta_{\alpha_S} \cdot N_0 = \frac{N(\alpha_S^{\text{up}}) - N(\alpha_S^{\text{down}})}{2} \quad (8.2)$$

and combined with the PDF uncertainty:

$$\delta_{\text{PDF}+\alpha_S} = \sqrt{\delta_{\text{PDF}}^2 + \delta_{\alpha_S}^2} \quad (8.3)$$

This prescription is applied to all samples, with the  $\alpha_S$  variation being considered when available.

**Scale uncertainties:** The uncertainties related to missing higher orders in the perturbative expansion of the partonic cross section are estimated by varying the renormalization scale  $\mu_R$  and factorization scale  $\mu_F$  separately up or down by a factor of two giving rise to two nuisance parameters.

**Radiation uncertainties:** The upward uncertainty on the initial state radiation (ISR) is evaluated by dividing both  $\mu_R$  and  $\mu_F$  by two and using the VAR3C up-variant of the A14 showering tune. For the downward uncertainty,  $\mu_R$  and  $\mu_F$  are doubled and the down variation of the showering tune is used. The final state radiation (FSR) uncertainty is derived using the dedicated parton shower weights, which correspond to the up and down variation of  $\alpha_S$  for FSR.

**Hard-scattering uncertainty:** To evaluate the uncertainty on the ME calculation, an alternative event generator for the hard-scattering process is used while keeping the parton showering generator the same. For such a systematic, which is evaluated by comparing two independent sets of events, the relative statistical uncertainty  $\delta_{\text{alt.}}^{\text{stat.}}$  of the alternative sample's event yield  $N_{\text{alt.}}$  is added in quadrature and then symmetrized:

$$\delta_{\text{alt.}}^{\text{syst.}} = \frac{N_{\text{alt.}} - N_0}{N_0} = \frac{N_{\text{alt.}}}{N_0} - 1 \quad (8.4)$$

$$\delta_{\text{alt.}}^{\text{syst.}\oplus\text{stat.}} = \text{sign}(\delta_{\text{alt.}}^{\text{syst.}}) \cdot \sqrt{(\delta_{\text{alt.}}^{\text{syst.}})^2 + (\delta_{\text{alt.}}^{\text{stat.}})^2} \quad (8.5)$$

$$\delta_{\text{alt.}}^{\text{up/down}} = \pm \delta_{\text{alt.}}^{\text{syst.}\oplus\text{stat.}} \quad (8.6)$$

By multiplying the sum of squares with the sign of  $\delta_{\text{alt.}}^{\text{syst.}}$  and not taking the absolute value of  $\delta_{\text{alt.}}^{\text{syst.}\oplus\text{stat.}}$  in the symmetrization, the direction of the variation is preserved.

**Parton-showering uncertainty:** To evaluate the uncertainty on the simulation of the fragmentation and hadronization, an alternative generator for the parton-shower simulation is used while keeping the hard-scattering generator the same. The computation of the uncertainty follows the description given above for the hard-scattering uncertainty.

**$Wt/t\bar{t}$  interference uncertainty:** This uncertainty only affects the single-top process. As explained in Section 4.3.1, the cancellation of overlapping diagrams in the

independently produced  $Wt$  and  $t\bar{t}$  samples can affect the prediction in phase-spaces sensitive to effects from the interference of such diagrams. In order to assess the uncertainty on the  $Wt/t\bar{t}$  interference, the predictions of the nominal DR and alternative DS samples are compared. As will be discussed later in Section 9.1, the nominal prediction of the DR samples significantly overestimate the  $Wt$  background, especially in the single-tau channel. However, upon normalization, a good description of the background is observed. In order to decouple the interference uncertainty from the uncertainty of the overall normalization, the *normalized* DS and DR predictions, derived in separate simplified background-only fits, are therefore used for the comparison. The computation of the uncertainty follows the description given above for the hard-scattering and parton-showering uncertainty.

**$V + \text{jets}$  modelling uncertainties:** Additional uncertainties arise in  $V + \text{jets}$  samples simulated with SHERPA, where a simplified scale setting prescription in the multiparton ME is used to increase the event generation speed [219]. The jet modelling uncertainties are evaluated by varying the resummation scale (QSF), the scale used for the resummation of soft gluon emission, up or down by a factor of two and by studying variations of the jet merging scale (CKKW), the scale taken for the calculation of the overlap between jets from the hard-scatter event and the parton showering [220, 221]. The CKKW scale has a nominal value of 20 GeV, while the up and down variations are 30 GeV and 15 GeV, respectively. The uncertainty on the event yields is calculated using the parameterization method described in Ref. [222].

### 8.2.2 Background theory uncertainties

In addition to the sources discussed in the previous Section 8.2.1, cross-section uncertainties are applied for all backgrounds which are not normalized to data. Due to its very low contribution in the analysis a flat 20% uncertainty is used for the minor top processes, which is of the order observed in other top-related backgrounds. For the residual backgrounds, PDF+ $\alpha_S$ , renormalization and factorization scale uncertainties are evaluated.

All three  $p_T(\tau)$  bins are merged for the evaluation of the theory uncertainties in the single-tau multi-bin SR in order to increase the available statistics. Additionally, the di-tau and single-tau one-bin SR cuts are loosened in order to reduce statistical fluctuations: The cut on  $m_{T2}(\tau_1, \tau_2)$  in the di-tau SR is lowered from 70 GeV to 50 GeV. For the single-tau one-bin SR,  $m_T(\tau) > 300$  GeV is lowered to 200 GeV.

For the  $t\bar{t}$  and single-top process, the variations in the hard-scatter and parton-shower simulations are evaluated on objects before detector simulation. The event selection is run directly on the generator-level objects, where a smearing is applied to emulate reconstruction and identification inefficiencies. The predicted event yields show a good

agreement, within the statistical uncertainties, with those from the fully reconstructed samples. The modelling uncertainty of the hard-scattering event is evaluated by comparing the predictions of the nominal POWHEG-BOX ME generator against MADGRAPH5\_aMC@NLO. Uncertainties on the fragmentation and hadronization simulation are derived by comparing the nominal PYTHIA8 parton-shower generator against HERWIG7 [223, 224].

Additionally, ISR and FSR variations are considered for the  $t\bar{t}$  background, while a cross-section uncertainty of 7% [142] is only applied for  $t\bar{t}$ -fake events, as this is the only component where the normalization is not taken from a dedicated CR. Uncertainties due to the  $Wt/t\bar{t}$ -interference and ISR are considered for the single-top background. For  $V + \text{jets}$  production, the CKKW and QSF scale uncertainties are evaluated and a cross-section uncertainty of 5% [225, 226] is applied. Diboson production is associated with a cross-section uncertainty of 6% [227], while for triboson production the uncertainty is quantified with 32% in Ref. [227], based on a comparison between SHERPA and VBFNLO [228]. Production cross-sections for  $t\bar{t} + Z$ ,  $t\bar{t} + W$  and  $t\bar{t} + H$  are assigned with relative uncertainties of 14% [229], 22% [229] and 12% [230], respectively. Lastly, the lesser contributing top-related processes (multitop,  $tZ$ ,  $tWZ$ ,  $ttVV$ ) are assigned a 15% cross-section uncertainty [231].

### 8.2.3 Signal theory uncertainties

Systematic uncertainties are evaluated for the benchmark stop-stau and several  $LQ_3^{u/d}$  signal points. From these studies a conservative estimate for the theory-related systematic uncertainties covering all points of the signal grids is motivated. Due to the low signal contribution in the CRs, the signal theory uncertainties are evaluated in the SRs only.

Additional stop-stau samples are generated by reconfiguring the generator settings to evaluate factorization and renormalization-scale variations, merging-scale variations and radiation uncertainties. As for the  $t\bar{t}$  and single-top generator comparison studies, discussed in the previous Section 8.2.2, the event selection is based on generator-level objects that are smeared to emulate the reconstruction effects. With the exception of the radiation variations, internal generator weights of the fully reconstructed  $LQ_3^{u/d}$  samples are used to derive factorization and renormalization scale uncertainties as well as the PDF+ $\alpha_s$  uncertainty. For the estimation of the radiation uncertainties, new samples are generated and evaluated using again the procedure based on generator-level objects.

Overall the total signal theory uncertainties can range up to 16% for the limited set of considered signal points. Based on these estimations a conservative flat 20% uncertainty is assumed for all stop-stau and  $LQ_3^{u/d}$  signal points. This uncertainty is also applied on the respective event yields in the CRs and VRs.

By convention, the uncertainty on the signal cross-sections, discussed in Sections 4.3.2

and 4.3.3, receives a special treatment: Instead of including it in the calculation of the nominal observed model-dependent exclusion limits, two additional variations of the exclusion contour are computed in which the signal cross-sections are set to their  $\pm 1\sigma$  values.

### 8.3 Impact on signal regions

Table 8.1 breaks down the relative contributions of the various systematic uncertainties on the background estimates in the SRs. The nuisance parameters are constrained in a background-only fit in the CRs and then extrapolated to the SRs, as discussed in Section 5.3.

The total systematic uncertainty ranges between 17–25%. The largest contribution in the di-tau SR originates from uncertainties in the JER, while for the SRs in the single-tau channel, the theoretical uncertainties on the  $t\bar{t}$  FSR and interference with the  $Wt$  process take the leading role.

|                              | Di-tau SR | Single-tau SR<br>(one-bin) | Single-tau SR<br>(multi-bin) |
|------------------------------|-----------|----------------------------|------------------------------|
| Total systematic uncertainty | 25 %      | 17 %                       | 17 %                         |
| Normalization                | 8.8 %     | 15 %                       | 16 %                         |
| Jet-related                  | 19 %      | 4.2 %                      | 3.9 %                        |
| Tau-related                  | 4.7 %     | 5.5 %                      | 4.3 %                        |
| Other experimental           | 3.7 %     | 1.0 %                      | 0.84 %                       |
| Theory                       | 13 %      | 17 %                       | 19 %                         |
| MC statistics                | 12 %      | 7.5 %                      | 4.4 %                        |
| Luminosity                   | 0.80 %    | 0.50 %                     | 0.35 %                       |

**Table 8.1:** Breakdown of the relative systematic uncertainties on the background estimates in the di-tau SR as well as the one-bin and (inclusive) multi-bin SR in the single-tau channel. The individual uncertainties can be correlated, and thus do not necessarily add up quadratically to the total background uncertainty, shown in the top row.



# 9 Results

After validating the extrapolation of the background estimate in the VRs, the SRs are unblinded. The background prediction is compared to data and interpreted in terms of model-dependent and -independent limits.

## 9.1 Observations

In the following, the results of the background estimation, derived in the background-only fit in the CRs, as described in Section 4.1, is summarized and compared to the observation for the various regions of the analysis. Table 9.1 summarizes the background prediction and observed data count in the control and validation regions. While the background estimate matches the observation in the CRs by construction, a good agreement with the data is observed throughout all VRs as well.

The fitted values and uncertainties of the normalization factors are given in Table 9.2. The  $t\bar{t}$ -related normalizations are compatible with unity within their uncertainties. A relatively small factor of  $\sim 0.2$  is observed for the single-top background. This can be attributed to the nominal MC prediction of the  $Wt$  samples using the DR scheme to

|          | CR $t\bar{t}$ (2 real $\tau$ ) | CR $t\bar{t}$ (1 real $\tau$ ) | VR $t\bar{t}$ (2 real $\tau$ ) | VR $t\bar{t}$ (1 real $\tau$ ) |
|----------|--------------------------------|--------------------------------|--------------------------------|--------------------------------|
| Observed | 140                            | 156                            | 27                             | 30                             |
| Expected | $141 \pm 14$                   | $155 \pm 13$                   | $31.4 \pm 4.1$                 | $30.1 \pm 3.5$                 |

(a) Di-tau channel

|          | CR $t\bar{t}$ (1 real $\tau$ ) | CR single-top | VR $t\bar{t}$ (1 real $\tau$ ) | VR single-top |
|----------|--------------------------------|---------------|--------------------------------|---------------|
| Observed | 171                            | 339           | 150                            | 123           |
| Expected | $171 \pm 16$                   | $339 \pm 17$  | $148 \pm 14$                   | $128 \pm 14$  |

(b) Single-tau channel

**Table 9.1:** Total SM background expectation after the background-only fit and observed event yield in data for the control and validation regions in di-tau (a) and single-tau channel (b). The uncertainties include both the statistical and systematic uncertainties.

| Process                     | Normalization factor   |
|-----------------------------|------------------------|
| $t\bar{t}$ (2 real $\tau$ ) | $0.93^{+0.32}_{-0.23}$ |
| $t\bar{t}$ (1 real $\tau$ ) | $0.84^{+0.21}_{-0.17}$ |
| Single top                  | $0.18^{+0.19}_{-0.16}$ |

**Table 9.2:** Values for the normalization factors from the background-only fit using the full set of systematic uncertainties.

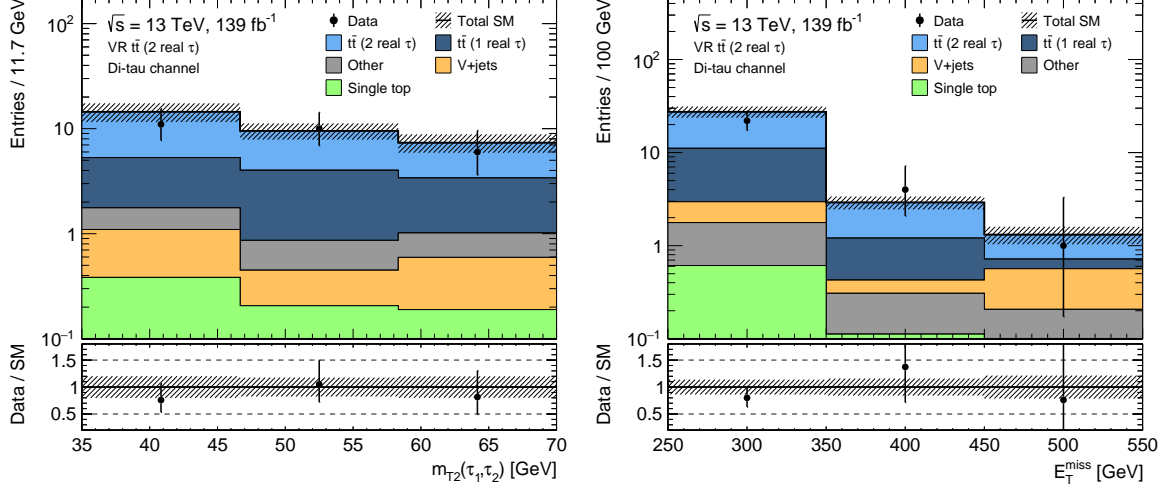
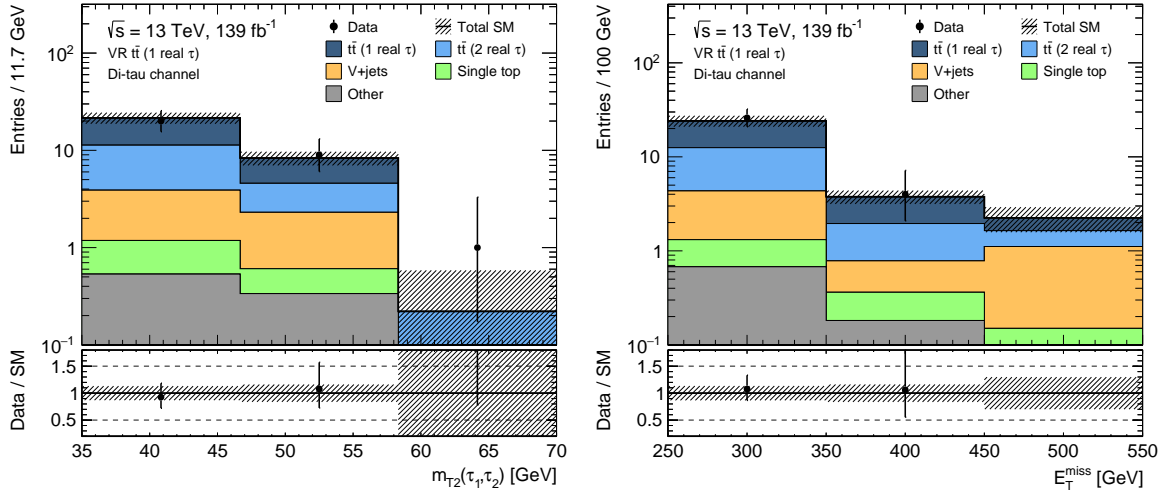
cancel the interference with the  $t\bar{t}$  process. The DS scheme yields a much lower nominal prediction, resulting in a better agreement with data before normalization. However, after normalization, the  $Wt$  (DR) samples yield a slightly higher and thus more conservative estimate in the tails of the main kinematic distributions. As discussed in Section 8.2, the difference in shapes is covered by a systematic uncertainty.

Kinematic distributions for various important variables are shown in Figures 9.1 and 9.2 for the VRs in the di-tau and single-tau channel, respectively. Again, a good description of the data can be observed within the uncertainties.

Finally, the expected and observed event yields in the SRs are shown in Table 9.3. None of them show a significant excess of data. Events with pair-produced top-quarks present the largest contribution in both channels, with additional contributions from single-top production mainly in the single-tau channel. Figures 9.3 and 9.4 show the kinematic distributions of selected variables in the di-tau and single-tau SRs, respectively. Although compatible with the SM prediction within the uncertainties, the observed data exceeds the background expectation in some bins of the distributions shown for the one-bin SR in the single-tau channel. As these small excesses vanish in the slightly loosened multi-bin selection, they can be attributed to statistical fluctuations.

Additional plots comparing kinematic distributions of the expected background against data for the various control, validation and signal regions are compiled in Appendix B.

Figure 9.5 summarizes the observed and expected event yields in all regions of the analysis. The lower panel gives the significance of the discrepancy in each bin, computed following the definition given in Equation (6.1), with the sum of signal and background yields,  $s + b$ , substituted with the observed data count.

(a) VR  $t\bar{t}$  (2 real  $\tau$ )(b) VR  $t\bar{t}$  (1 real  $\tau$ )

**Figure 9.1:** Distributions of  $m_{T2}(\tau_1, \tau_2)$  and  $E_T^{\text{miss}}$  in the  $t\bar{t}$  (2 real  $\tau$ ) (a) and  $t\bar{t}$  (1 real  $\tau$ ) VRs (b) of the di-tau channel. The stacked histograms show the various SM background contributions. The hatched band indicates the total statistical and systematic uncertainty of the background. The expected event yields are scaled with the respective normalization factors obtained from the background-only fit. Minor backgrounds are grouped together and denoted as ‘Other’. This includes  $t\bar{t}$ -fake,  $t\bar{t}+X$ , multiboson, and other top. The rightmost bin includes the overflowed events.

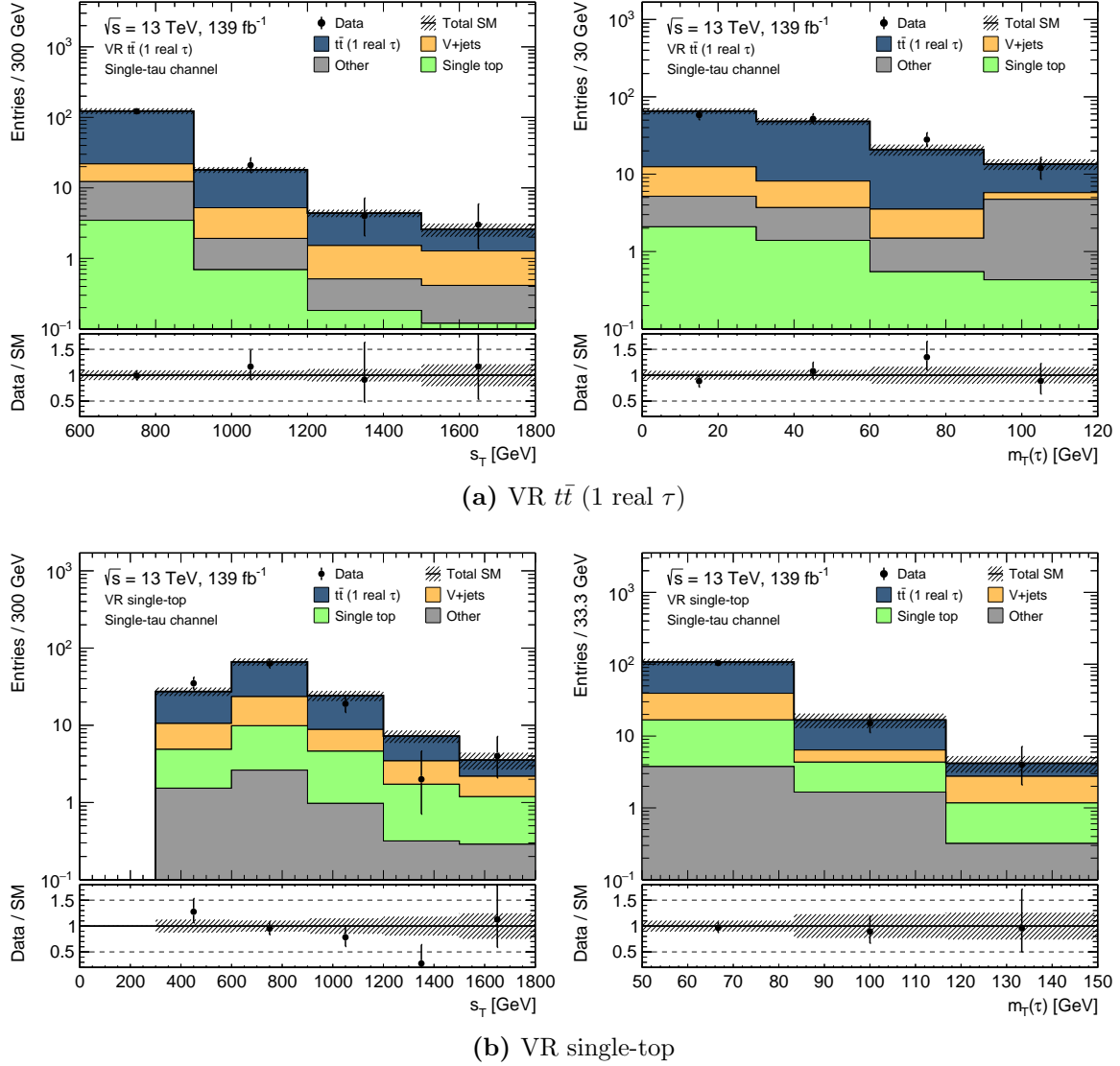


**Figure 9.2:** Distributions of  $s_T$  and  $m_T(\tau)$  in the  $t\bar{t}$  (1 real  $\tau$ ) (a) and single-top VRs (b) of the single-tau channel. The stacked histograms show the various SM background contributions. The hatched band indicates the total statistical and systematic uncertainty of the background. The expected event yields are scaled with the respective normalization factors obtained from the background-only fit. Minor backgrounds are grouped together and denoted as ‘Other’. This includes  $t\bar{t}$ -fake,  $t\bar{t} + X$ , multiboson, and other top. The rightmost bin includes the overflowed events.

|                             | Di-tau SR |                     | Single-tau SR<br>(one-bin)  | Single-tau SR<br>(binned in $p_T(\tau)$ ) |                             |                             |
|-----------------------------|-----------|---------------------|-----------------------------|---|-----------------------------|-----------------------------|
|                             |           |                     |                             | [50, 100] GeV                             | [100, 200] GeV              | > 200 GeV                   |
| Observed                    | 2         |                     | 6                           | 8   | 6                           | 2                           |
| Total bkg.                  | 4.1       | $\pm 1.0$           | 3.23 $\pm 0.55$             | 10.1 $\pm 1.8$                            | 5.1 $\pm 1.1$               | 2.05 $\pm 0.64$             |
| $t\bar{t}$ (2 real $\tau$ ) | 0.81      | $\pm 0.71$          | —                           | —   | —                           | —                           |
| $t\bar{t}$ (1 real $\tau$ ) | 0.82      | $\pm 0.27$          | 1.20 $\pm 0.30$             | 4.8 $\pm 1.2$                             | 2.69 $\pm 0.88$             | 0.64 $\pm 0.29$             |
| $t\bar{t}$ -fake            | 0.51      | $\pm 0.15$          | 0.69 $\pm 0.15$             | 2.83 $\pm 0.87$                           | 0.66 $\pm 0.17$             | 0.185 $\pm 0.072$           |
| Single top                  | 0.03      | $\pm_{0.03}^{0.10}$ | 0.39 $\pm_{0.39}^{0.45}$    | 0.85 $\pm_{0.85}^{0.86}$                  | 0.54 $\pm 0.54$             | 0.57 $\pm 0.56$             |
| $W$ + jets                  | 0.08      | $\pm_{0.08}^{0.11}$ | 0.35 $\pm 0.16$             | 0.34 $\pm 0.12$                           | 0.64 $\pm 0.24$             | 0.37 $\pm 0.12$             |
| $Z$ + jets                  | 0.35      | $\pm 0.14$          | 0.187 $\pm 0.054$           | 0.275 $\pm 0.081$                         | 0.043 $\pm 0.022$           | 0.123 $\pm 0.048$           |
| Multiboson                  | 0.48      | $\pm 0.21$          | 0.085 $\pm 0.037$           | 0.163 $\pm 0.037$                         | 0.111 $\pm 0.030$           | 0.030 $\pm_{0.030}^{0.032}$ |
| $t\bar{t} + V$              | 0.60      | $\pm 0.15$          | 0.242 $\pm 0.064$           | 0.65 $\pm 0.16$                           | 0.31 $\pm 0.12$             | 0.092 $\pm 0.035$           |
| $t\bar{t} + H$              | 0.28      | $\pm_{0.28}^{0.29}$ | 0.039 $\pm_{0.039}^{0.040}$ | 0.10 $\pm 0.10$                           | 0.060 $\pm_{0.060}^{0.061}$ | 0.028 $\pm_{0.028}^{0.029}$ |
| Other top                   | 0.122     | $\pm 0.067$         | 0.043 $\pm 0.022$           | 0.096 $\pm 0.074$                         | 0.091 $\pm 0.049$           | 0.0120 $\pm 0.0084$         |

**Table 9.3:** Expected numbers of events from the SM background processes after the background-only fit and observed event yield in data for the SRs. The uncertainties include both the statistical and systematic uncertainties, truncated at zero. Note that by construction no  $t\bar{t}$  (2 real  $\tau$ ) events enter the single-tau channel.

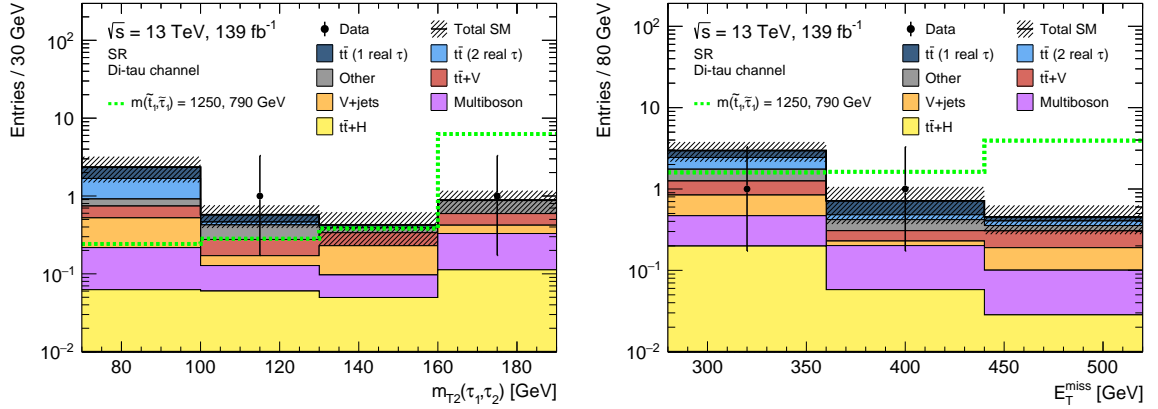


**Figure 9.3:** Distributions of  $m_{T2}(\tau_1, \tau_2)$  and  $E_T^{\text{miss}}$  in the di-tau SR. The stacked histograms show the various SM background contributions. The hatched band indicates the total statistical and systematic uncertainty of the background. The expected event yields are scaled with the respective normalization factors obtained from the background-only fit. Minor backgrounds are grouped together and denoted as ‘Other’. This includes  $t\bar{t}$ -fake, single top, and other top. The rightmost bin includes the overflowed events.

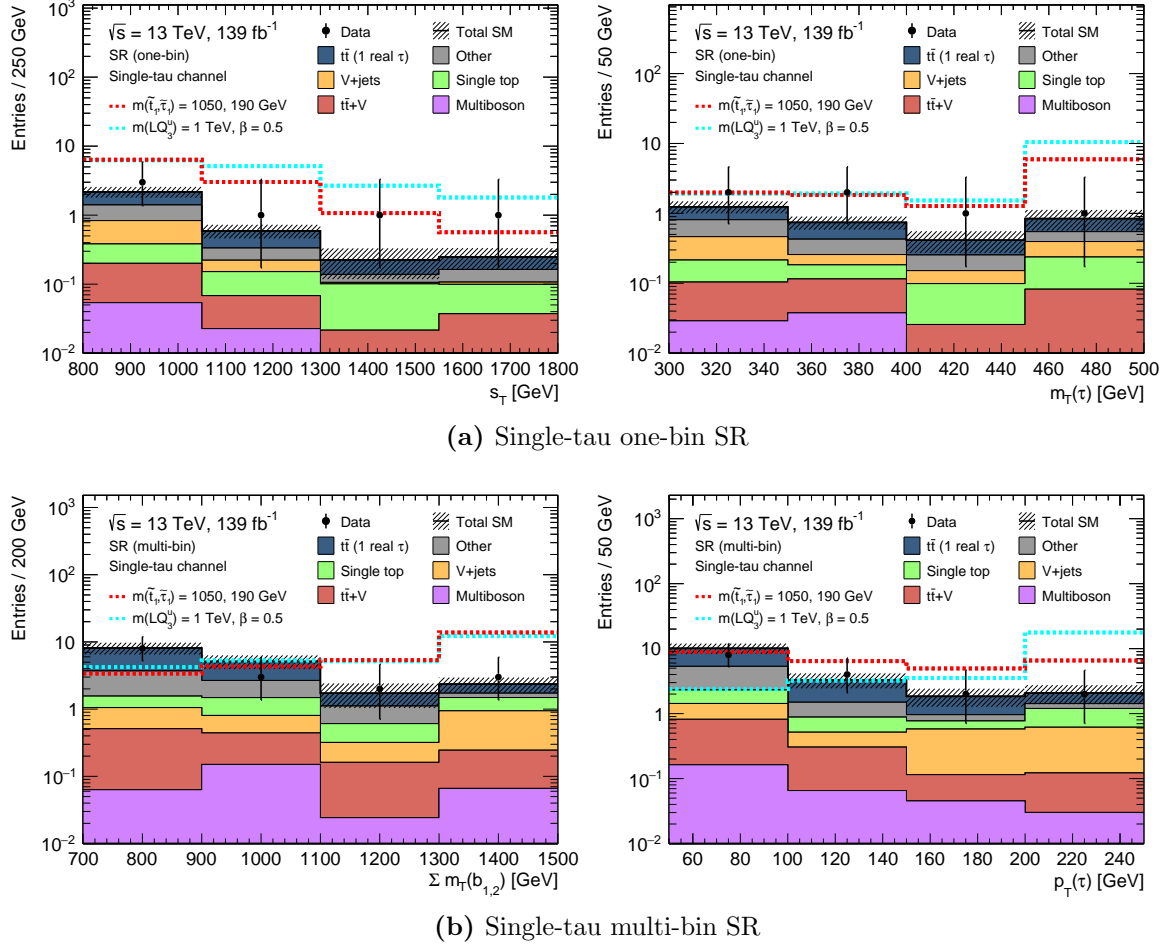


**Figure 9.4:** Distributions of  $s_T$  and  $p_T(\tau)$  in the one-bin SR (a) and of  $\Sigma m_T(b_1, b_2)$  and  $p_T(\tau)$  in the  $p_T(\tau)$ -binned SR (b) in the single-tau channel. The stacked histograms show the various SM background contributions. The hatched band indicates the total statistical and systematic uncertainty of the background. The expected event yields are scaled with the respective normalization factors obtained from the background-only fit. Minor backgrounds are grouped together and denoted as ‘Other’. This includes  $t\bar{t}$ -fake,  $t\bar{t} + H$ , and other top. The rightmost bin includes the overflowed events.

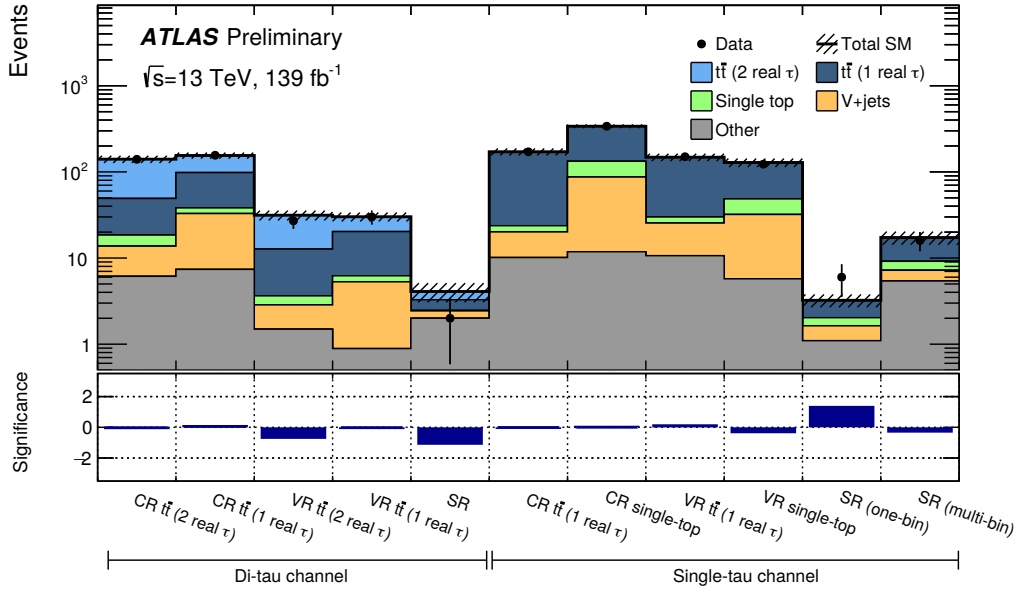


**Figure 9.5:** Comparison of expected and observed event yields (top panel) and the significance of their discrepancy (bottom panel) for all regions of the analysis. The stacked histograms show the various SM background contributions. The hatched band indicates the total statistical and systematic uncertainty of the background. The expected event yields are scaled with the respective normalization factors obtained from the background-only fit. Minor backgrounds are grouped together and denoted as ‘Other’. This includes  $t\bar{t}$ -fake,  $t\bar{t} + X$ , multiboson, and other top. Figure adapted from Ref. [232].

## 9.2 Exclusion limits

As no significant excess over the SM prediction is observed, the results are interpreted in terms of exclusion limits on the signal-model parameters. A combined fit in the control and signal regions is performed for each signal point, as described in Section 5.3. The signal contribution as predicted by the tested model is taken into account in all regions, not just the SR(s), to correctly account for signal contamination in the CRs.

Following the  $CL_s$  prescription and using the asymptotic approximation, discussed in Section 5.2, exclusion contours at 95% confidence level (CL), are shown in Figures 9.6 and 9.7 for the stop-stau and  $LQ_3^{u/d}$  signal, respectively. The signal-plus-background hypothesis is considered excluded for signal-parameter values that lie within the contour ( $CL_s < 0.05$ ). The dashed black line corresponds to the expected limit for the Asimov data set, i. e. assuming an observation identical to the prediction of the background-only hypothesis. The yellow band shows the  $\pm 1\sigma$  impact of the statistical and systematic uncertainties on the expected limit. The observed exclusion contour is depicted by a solid red line and the dashed uncertainty band is obtained by varying the signal expectation by  $\pm 1\sigma$  of the theoretical signal cross-section uncertainty separately.

For the stop-stau signal, both the di-tau and single-tau multi-bin SR are used simultaneously. Due to the slight deficit in data observed in the di-tau SR, the observed limit is slightly stronger than the expected one. Top-squark masses of up to  $\sim 1.4$  TeV are excluded at 95% CL across a wide range of  $m(\tilde{\tau}_1)$  up to 1.2 TeV. For large mass splittings, i. e. low tau-slepton masses, the limit is slightly weaker, because the fraction of  $E_T^{\text{miss}}$  originating from the neutrinos in the top-squark decay increases, and thus the discrimination power of  $m_{T2}(\tau_1, \tau_2)$  is reduced. In Appendix A the individual exclusion contours for each separate SR are shown.

As discussed in Section 4.1, only the single-tau multi-bin SR in addition to the four CRs is used to set limits on the  $LQ_3^{u/d}$  parameter space. Here, both up- and down-type  $LQ_3$  signals with masses up to  $\sim 1.25$  TeV can be excluded for intermediate values of the branching ratios into charged leptons at 95% CL. The shape of the exclusion contour is predominantly governed by the probability of the  $LQ_3^{u/d}$  pair to yield a final state with exactly one tau. For branching ratios either close to zero or one, the limit is weaker as the fraction of events with exactly one tau decreases, thus leading to a lower

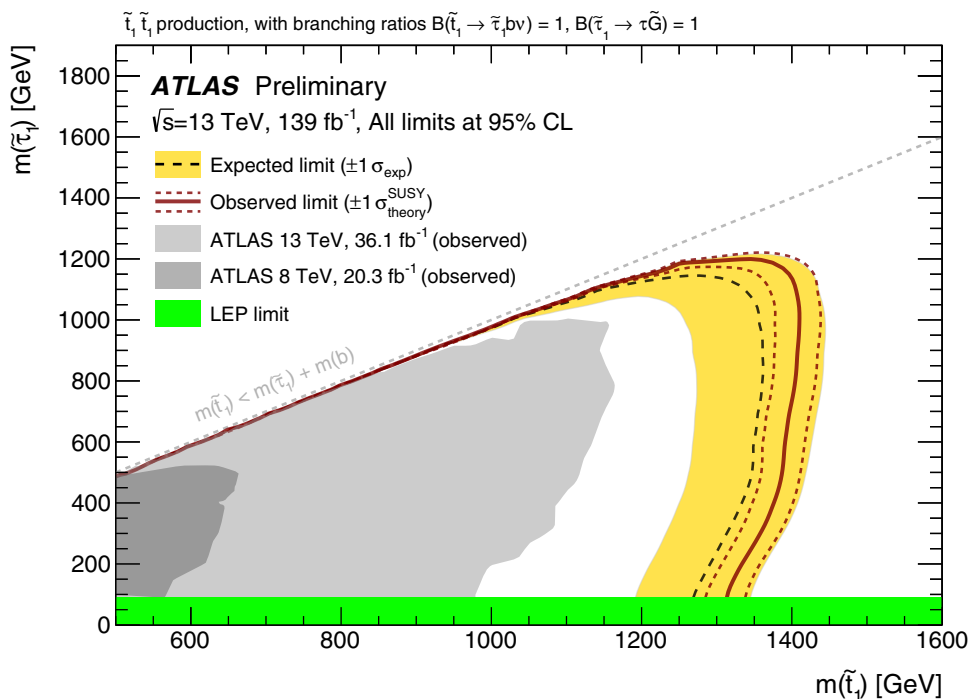


**Figure 9.6:** Exclusion contours at 95% confidence level for the stop-stau signal as a function of  $m(\tilde{t}_1)$  and  $m(\tilde{\tau}_1)$ . The observed (solid red line) and expected limits (dashed black line) are derived in a fit including all CRs and both the di-tau and single-tau multi-bin SR. For comparison, previous observed limits from ATLAS from Run 1 of the LHC at  $\sqrt{s} = 8$  TeV [83] and for a partial dataset from Run 2 at  $\sqrt{s} = 13$  TeV [82] are shown by the grey areas. The green band indicates the limit on the tau slepton mass from the LEP experiments [81]. Figure adapted from Ref. [232].

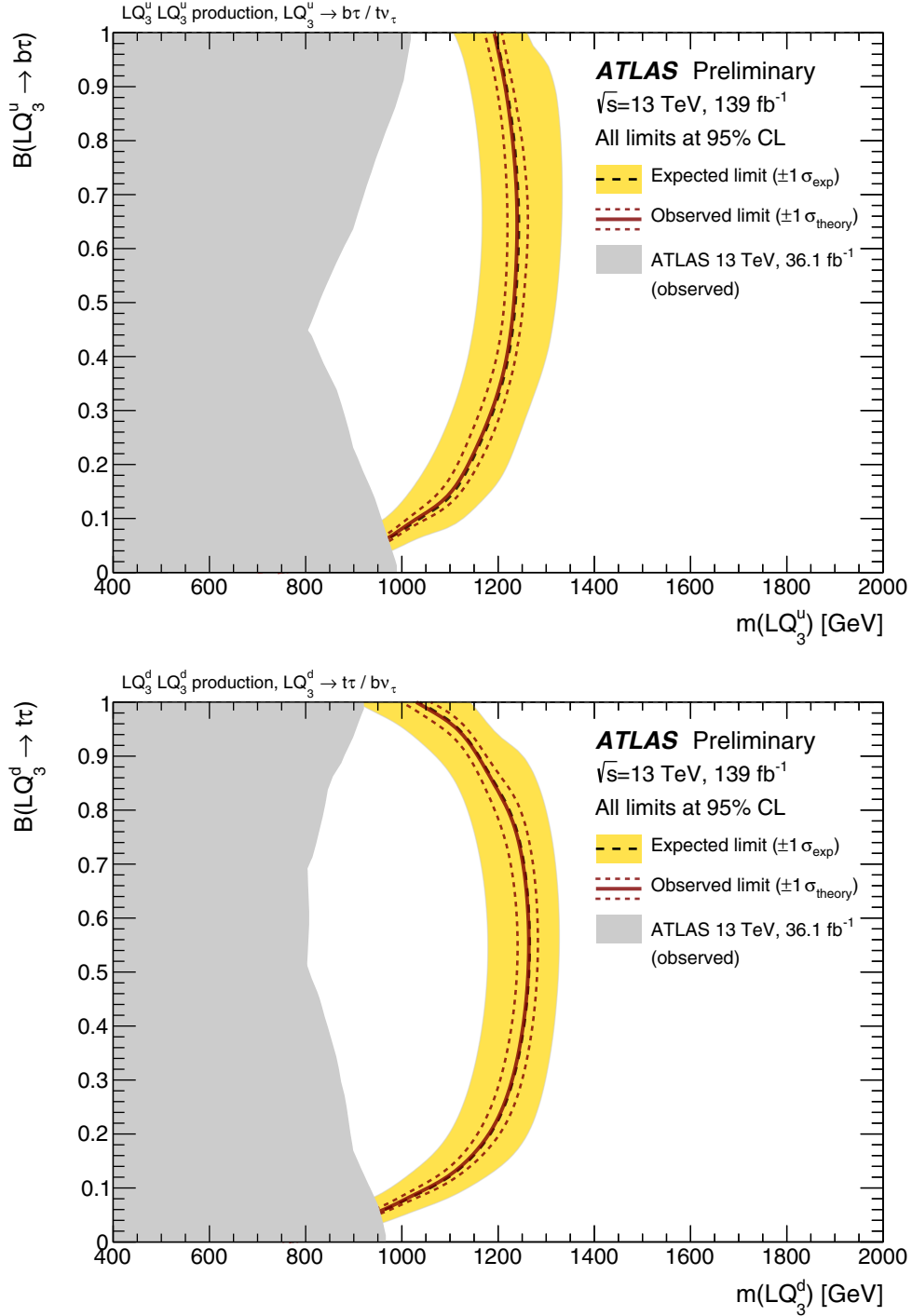


**Figure 9.7:** Exclusion contours at 95% confidence level for up- and down-type  $LQ_3$  signals as a function of  $m(LQ_3^{u/d})$  and the branching ratio into charged leptons. The observed (solid red line) and expected limits (dashed black line) are derived in a fit including all CRs and single-tau multi-bin SR. For comparison, the previous observed limit from ATLAS using the partial Run 2 dataset [92] is shown by the grey area. Figures adapted from Ref. [232].

signal acceptance. In particular for down-type  $LQ_3$  signals with  $B(LQ_3^d \rightarrow t\tau) \sim 1$ , the additional source of taus from the top-quark decay leads to a slightly lower exclusion reach compared to the corresponding up-type  $LQ_3$  signals.

### 9.3 Model-independent limits

The results can also be interpreted in terms of model-independent upper limits on the number of beyond-SM events in each SR. The limits are derived in a model-independent signal fit as described in Section 5.3. For this, a generic signal is substituted for the simplified signal model, which can give rise to additional events in the SR. In order to avoid any assumption on the signal model, SRs must be evaluated independently and cannot be binned. Consequently, the  $p_T(\tau)$ -binned SR in the single-tau channel is not used here. Since for the same reason the CRs must be assumed to be free of any signal contamination, the background prediction derived in the background-only fit, given in Table 9.3, is used for the SRs. Furthermore, neither experimental nor theoretical uncertainties are assumed for the signal.

The additional generic signal event in the given SR is scaled by the signal strength parameter  $\mu$ . Starting from  $\mu = 0$ , the signal strength is scanned in discrete steps to find the value for which the  $CL_s$  value of the signal-plus-background hypothesis falls below 0.05. This value defines the upper limit on the observed and expected number of additional signal events,  $S_{\text{obs}}^{95}$  and  $S_{\text{exp}}^{95}$ , respectively, at 95% CL. The uncertainty on  $S_{\text{exp}}^{95}$  is computed by varying the background expectation by  $\pm 1\sigma$ . By dividing  $S_{\text{obs}}^{95}$  by the integrated luminosity of the data, the result can also be expressed as an upper limit on the visible signal cross-section  $\langle \epsilon A \sigma \rangle_{\text{obs}}^{95}$ , defined as the product of acceptance  $A$ , reconstruction efficiency  $\epsilon$  and signal cross-section  $\sigma$ .

Table 9.4 shows the upper limits for the di-tau and single-tau one-bin SR. The  $\mu$  scan-range and steps-size has been optimized to guarantee a smooth behavior of the  $CL_s$  curves. The test statistic for each scan point is evaluated using toy experiments. The tables also reports the observed discovery  $p$ -value for the background-only hypothesis and the associated significance  $Z$ .

| Signal channel        | $\langle \epsilon A \sigma \rangle_{\text{obs}}^{95}$ [fb] | $S_{\text{obs}}^{95}$ | $S_{\text{exp}}^{95}$ | $p(s = 0)$ ( $Z$ ) |
|-----------------------|--|-----------------------|-----------------------|--------------------|
| Di-tau SR             | 0.03   | 4.1                   | $5.3_{-1.5}^{+2.2}$   | 0.50 (0.0)         |
| Single-tau one-bin SR | 0.06   | 8.2                   | $5.1_{-1.3}^{+2.1}$   | 0.08 (1.37)        |

**Table 9.4:** Model-independent upper limits at 95% CL on the visible cross section  $\langle \epsilon A \sigma \rangle_{\text{obs}}^{95}$  and observed (expected) number of signal events  $S_{\text{obs}}^{95}$  ( $S_{\text{exp}}^{95}$ ) in the di-tau and single-tau one-bin SR. The last column shows the observed discovery  $p$ -value and significance  $Z$  for the background-only hypothesis. In case fewer events than expected are observed, the  $p$ -value is capped at 0.5.

# 10 Conclusion

This thesis presented a search for new physics in final states with hadronically decaying tau leptons,  $b$ -jets and large missing transverse momentum. The analysis targets two simplified signal models, which consider either a supersymmetric extension of the SM or introduce new mediators between quarks and leptons, called leptoquarks. In the supersymmetric model, pair-produced top squarks are assumed to decay into a tau slepton, a  $b$ -quark and a neutrino each. The tau slepton then decays further into a tau lepton and a stable and nearly massless gravitino. The other signal model considers pair-production of scalar leptoquarks, each decaying into a quark-lepton pair of the third generation.

The full dataset of proton–proton collisions at  $\sqrt{s} = 13$  TeV recorded with the ATLAS detector in Run 2 of the LHC is used, corresponding to an integrated luminosity of  $139 \text{ fb}^{-1}$ . Two statistically independent signal selections have been developed to account for the dependence of the kinematics on the signal parameters. The di-tau channel targets final states with two or more hadronically taus, while the single-tau channel focusses on a signature with exactly one. Theoretical predictions for the signal and background contributions are derived using MC simulation. The contribution of the dominating background processes, pair- and singly-produced top-quarks, is normalized via a simultaneous fit to data in dedicated selections. The extrapolation to the signal selections has been validated in dedicated and kinematically close regions of the phase-space before the analysis was unblinded. Theoretical and experimental systematic uncertainties are accounted for in the statistical evaluation.

No significant deviation from the SM prediction is observed in any of the selections. The results are interpreted in terms of exclusion limits on the signal parameters. In case of the supersymmetric model, the limit at 95 % CL reaches top-squark masses up to 1.4 TeV across a wide range of tau-slepton masses. For both up-type and down-type scalar leptoquarks, masses of up to around 1.25 TeV are excluded. The analysis is able to significantly extend previous limits on the simplified models and provides a valuable contribution to the search for new physics at the LHC. This gain in sensitivity is due to the larger dataset, the improved identification algorithms for tau leptons and  $b$ -jets, as well as the improved analysis strategy. Expressed in terms of model-independent limits at 95 % CL, a potential signal contribution of more than 4.1 or 8.2 events in the di-tau or single-tau signal region, respectively, would be inconsistent with the observation.

Looking ahead, the LHC is currently being prepared for its high-luminosity upgrade [233]. The instantaneous luminosities are expected to increase by a factor of five compared

to the nominal Run 2 value, thereby enlarging the total size of the data sample by one order of magnitude. While analyzing such a large dataset will come with many challenges, it will enable even more precise test of the SM and shed further light on the extreme phase spaces occupied by potential new physics. Given the success story of the LHC and its predecessors, there is much reason to look forward to the future of experimental particle physics.

# Bibliography

- [1] M. Asano, H. D. Kim, R. Kitano, and Y. Shimizu, “Natural supersymmetry at the LHC”, *JHEP* **2010** no. 12, (2010) 19.  
[https://doi.org/10.1007/JHEP12\(2010\)019](https://doi.org/10.1007/JHEP12(2010)019).
- [2] M. Leurer, “Comprehensive study of leptoquark bounds”, *Phys. Rev. D* **49** (Jan, 1994) 333–342. <https://link.aps.org/doi/10.1103/PhysRevD.49.333>.
- [3] D. J. Griffiths, *Introduction to Elementary Particles*. Wiley, New York, 2008.
- [4] M. Thomson, *Modern particle physics*. Cambridge University Press, New York, 2013.
- [5] ATLAS Collaboration, “Observation of a new particle in the search for the Standard Model Higgs boson with the ATLAS detector at the LHC”, *Phys. Lett. B* **716** (2012) 1, [arXiv:1207.7214](https://arxiv.org/abs/1207.7214) [hep-ex].
- [6] CMS Collaboration, “Observation of a new boson at a mass of 125 GeV with the CMS experiment at the LHC”, *Phys. Lett. B* **716** (2012) 30, [arXiv:1207.7235](https://arxiv.org/abs/1207.7235) [hep-ex].
- [7] Wikimedia Commons, “Standard model of elementary particles”, Feb, 2021.  
[https://en.wikipedia.org/wiki/File:Standard\\_Model\\_of\\_Elementary\\_Particles.svg](https://en.wikipedia.org/wiki/File:Standard_Model_of_Elementary_Particles.svg). last visited on 2021-02-19.
- [8] S. Gariazzo, M. Archidiacono, P. de Salas, O. Mena, C. Ternes, and M. Tórtola, “Neutrino masses and their ordering: global data, priors and models”, *Journal of Cosmology and Astroparticle Physics* **2018** no. 03, (Mar, 2018) 011–011.  
<https://doi.org/10.1088/1475-7516/2018/03/011>.
- [9] B. Ishak, “Neutrino cosmology, by j. lesgourgues, g. mangano, g. miele and s. pastor”, *Contemporary Physics* **54** no. 3, (2013) 178–179,  
<https://doi.org/10.1080/00107514.2013.818063>.
- [10] F. Zwicky, “Die Rotverschiebung von extragalaktischen Nebeln”, *Helv. Phys. Acta* **6** (1933) 110–127. [Gen. Rel. Grav.41,207(2009)].
- [11] R. Massey, T. Kitching, and J. Richard, “The dark matter of gravitational lensing”, [arXiv:1001.1739](https://arxiv.org/abs/1001.1739).

- [12] P. J. E. Peebles, “Tests of Cosmological Models Constrained by Inflation”, *Astrophys. J.* **284** (1984) 439–444.
- [13] J. P. Ostriker and P. J. Steinhardt, “Cosmic concordance”, [arXiv:astro-ph/9505066](https://arxiv.org/abs/astro-ph/9505066).
- [14] H. Baer and X. Tata, *Weak Scale Supersymmetry: From Superfields to Scattering Events*. Cambridge University Press, New York, USA, 1st ed., 2006.
- [15] S. P. Martin, “A Supersymmetry Primer”, *Adv. Ser. Direct. High Energy Phys.* **18** (1998) 1, [arXiv:hep-ph/9709356](https://arxiv.org/abs/hep-ph/9709356).
- [16] Nobel Media AB 2021, “The Nobel Prize in Physics 2004 – Popular information”, Oct, 2004. <https://www.nobelprize.org/prizes/physics/2004/popular-information/>. last visited on 2021-02-19.
- [17] ALEPH, DELPHI, L3, OPAL, SLD, LEP Electroweak Working Group, SLD Electroweak Group, SLD Heavy Flavour Group, “Precision electroweak measurements on the  $Z$  resonance”, *Phys. Rept.* **427** (2006) 257–454, [arXiv:hep-ex/0509008](https://arxiv.org/abs/hep-ex/0509008).
- [18] BaBar Collaboration, “Measurement of an Excess of  $\bar{B} \rightarrow D^{(*)}\tau^{-}\bar{\nu}_{\tau}$  Decays and Implications for Charged Higgs Bosons”, *Phys. Rev. D* **88** no. 7, (2013) 072012, [arXiv:1303.0571](https://arxiv.org/abs/1303.0571) [[hep-ex](#)].
- [19] Belle Collaboration, “Measurement of  $\mathcal{R}(d)$  and  $\mathcal{R}(D^*)$  with a semileptonic tagging method”, *Phys. Rev. Lett.* **124** (Apr, 2020) 161803. <https://link.aps.org/doi/10.1103/PhysRevLett.124.161803>.
- [20] LHCb Collaboration, “Test of lepton universality with  $B^0 \rightarrow K^{*0}\ell^+\ell^-$  decays”, *JHEP* **08** (2017) 055, [arXiv:1705.05802](https://arxiv.org/abs/1705.05802) [[hep-ex](#)].
- [21] LHCb Collaboration, “Search for lepton-universality violation in  $B^+ \rightarrow K^+\ell^+\ell^-$  decays”, *Phys. Rev. Lett.* **122** no. 19, (2019) 191801, [arXiv:1903.09252](https://arxiv.org/abs/1903.09252) [[hep-ex](#)].
- [22] LHCb Collaboration, “Angular analysis of the  $B^0 \rightarrow K^{*0}\mu^+\mu^-$  decay using  $3 \text{ fb}^{-1}$  of integrated luminosity”, *JHEP* **02** (2016) 104, [arXiv:1512.04442](https://arxiv.org/abs/1512.04442) [[hep-ex](#)].
- [23] Belle Collaboration, “Lepton-Flavor-Dependent Angular Analysis of  $B \rightarrow K^*\ell^+\ell^-$ ”, *Phys. Rev. Lett.* **118** no. 11, (2017) 111801, [arXiv:1612.05014](https://arxiv.org/abs/1612.05014) [[hep-ex](#)].
- [24] LHCb Collaboration, “Measurement of  $CP$ -Averaged Observables in the  $B^0 \rightarrow K^{*0}\mu^+\mu^-$  Decay”, *Phys. Rev. Lett.* **125** (Jul, 2020) 011802. <https://link.aps.org/doi/10.1103/PhysRevLett.125.011802>.

- 
- [25] Y. Golfand and E. Likhtman, “Extension of the Algebra of Poincare Group Generators and Violation of P Invariance”, *JETP Lett.* **13** (1971) 323. [Pisma Zh. Eksp. Teor. Fiz. **13** (1971) 452].
- [26] D. Volkov and V. Akulov, “Is the neutrino a goldstone particle?”, *Phys. Lett. B* **46** (1973) 109.
- [27] J. Wess and B. Zumino, “Supergauge transformations in four dimensions”, *Nucl. Phys. B* **70** (1974) 39.
- [28] J. Wess and B. Zumino, “Supergauge invariant extension of quantum electrodynamics”, *Nucl. Phys. B* **78** (1974) 1.
- [29] S. Ferrara and B. Zumino, “Supergauge invariant Yang-Mills theories”, *Nucl. Phys. B* **79** (1974) 413.
- [30] A. Salam and J. Strathdee, “Super-symmetry and non-Abelian gauges”, *Phys. Lett. B* **51** (1974) 353.
- [31] M. Bustamante, L. Cieri, and J. Ellis, “Beyond the standard model for montaneros”, [arXiv:0911.4409](https://arxiv.org/abs/0911.4409).
- [32] P. van Nieuwenhuizen, “Supergravity”, *Physics Reports* **68** no. 4, (1981) 189–398.  
<https://www.sciencedirect.com/science/article/pii/0370157381901575>.
- [33] R. Haag, J. T. Lopuszański, and M. Sohnius, “All possible generators of supersymmetries of the s-matrix”, *Nuclear Physics B* **88** no. 2, (1975) 257 – 274.  
<http://www.sciencedirect.com/science/article/pii/0550321375902795>.
- [34] S. Coleman and J. Mandula, “All possible symmetries of the s matrix”, *Phys. Rev.* **159** no. 5, (July, 1967) 1251–1256.
- [35] S. Dimopoulos and G. Giudice, “Naturalness constraints in supersymmetric theories with non-universal soft terms”, *Physics Letters B* **357** no. 4, (1995) 573–578.  
<https://www.sciencedirect.com/science/article/pii/037026939500961J>.
- [36] Super-Kamiokande Collaboration, “Search for proton decay via  $p \rightarrow e^+ \pi^0$  and  $p \rightarrow \mu^+ \pi^0$  in 0.31 megaton · years exposure of the Super-Kamiokande water Cherenkov detector”, *Phys. Rev. D* **95** (Jan, 2017) 012004.  
<https://link.aps.org/doi/10.1103/PhysRevD.95.012004>.
- [37] G. R. Farrar and P. Fayet, “Phenomenology of the production, decay, and detection of new hadronic states associated with supersymmetry”, *Phys. Lett. B* **76** (1978) 575.

- [38] J. Ellis, J. Hagelin, D. V. Nanopoulos, K. A. Olive, and M. Srednicki, “Supersymmetric relics from the big bang”, *Nucl. Phys. B* **238** (1984) 453.
- [39] M. Pospelov, “Particle physics catalysis of thermal Big Bang Nucleosynthesis”, *Phys. Rev. Lett.* **98** (2007) 231301, [arXiv:hep-ph/0605215](https://arxiv.org/abs/hep-ph/0605215).
- [40] H. K. Dreiner, “An introduction to explicit R-parity violation”, *Adv. Ser. Direct. High Energy Phys.* **21** (2010) 565–583, [arXiv:hep-ph/9707435](https://arxiv.org/abs/hep-ph/9707435).
- [41] R. Barbier *et al.*, “R-parity violating supersymmetry”, *Phys. Rept.* **420** (2005) 1–202, [arXiv:hep-ph/0406039](https://arxiv.org/abs/hep-ph/0406039).
- [42] M. Dine and W. Fischler, “A Phenomenological Model of Particle Physics Based on Supersymmetry”, *Phys. Lett. B* **110** (1982) 227.
- [43] L. Alvarez-Gaume, M. Claudson, and M. B. Wise, “Low-Energy Supersymmetry”, *Nucl. Phys. B* **207** (1982) 96.
- [44] C. R. Nappi and B. A. Ovrut, “Supersymmetric Extension of the SU(3) x SU(2) x U(1) Model”, *Phys. Lett. B* **113** (1982) 175.
- [45] R. Casalbuoni, “High-energy equivalence theorems in spontaneously broken gauge theories”, *Nuclear Physics B - Proceedings Supplements* **16** (1990) 577–578.  
<https://www.sciencedirect.com/science/article/pii/092056329090600Y>.
- [46] A. L. Maroto and J. R. Peláez, “The equivalence theorem and the production of gravitinos after inflation”, *Phys. Rev. D* **62** (Jun, 2000) 023518.  
<https://link.aps.org/doi/10.1103/PhysRevD.62.023518>.
- [47] G. Hiller and M. Schmaltz, “ $R_K$  and future  $b \rightarrow s\ell\ell$  physics beyond the standard model opportunities”, *Phys. Rev. D* **90** (2014) 054014, [arXiv:1408.1627](https://arxiv.org/abs/1408.1627) [hep-ph].
- [48] B. Gripaios, M. Nardecchia, and S. A. Renner, “Composite leptoquarks and anomalies in  $B$ -meson decays”, *JHEP* **05** (2015) 006, [arXiv:1412.1791](https://arxiv.org/abs/1412.1791) [hep-ph].
- [49] M. Freytsis, Z. Ligeti, and J. T. Ruderman, “Flavor models for  $\bar{B} \rightarrow D^{(*)}\tau\bar{\nu}$ ”, *Phys. Rev. D* **92** no. 5, (2015) 054018, [arXiv:1506.08896](https://arxiv.org/abs/1506.08896) [hep-ph].
- [50] M. Bauer and M. Neubert, “Minimal Leptoquark Explanation for the  $R_{D^{(*)}}$ ,  $R_K$ , and  $(g-2)_\mu$  Anomalies”, *Phys. Rev. Lett.* **116** no. 14, (2016) 141802, [arXiv:1511.01900](https://arxiv.org/abs/1511.01900) [hep-ph].
- [51] L. Di Luzio and M. Nardecchia, “What is the scale of new physics behind the  $B$ -flavour anomalies?”, *Eur. Phys. J. C* **77** no. 8, (2017) 536, [arXiv:1706.01868](https://arxiv.org/abs/1706.01868) [hep-ph].

- [52] D. Buttazzo, A. Greljo, G. Isidori, and D. Marzocca, “B-physics anomalies: a guide to combined explanations”, *JHEP* **11** (2017) 044, [arXiv:1706.07808 \[hep-ph\]](#).
- [53] LHCb Collaboration, “Test of lepton universality using  $B^+ \rightarrow K^+ \ell^+ \ell^-$  decays”, *Phys. Rev. Lett.* **113** (2014) 151601, [arXiv:1406.6482 \[hep-ex\]](#).
- [54] H. Päs and E. Schumacher, “Common origin of  $R_K$  and neutrino masses”, *Phys. Rev. D* **92** no. 11, (2015) 114025, [arXiv:1510.08757 \[hep-ph\]](#).
- [55] I. Doršner, S. Fajfer, and N. Košnik, “Leptoquark mechanism of neutrino masses within the grand unification framework”, *Eur. Phys. J. C* **77** no. 6, (2017) 417, [arXiv:1701.08322 \[hep-ph\]](#).
- [56] O. Popov and G. A. White, “One Leptoquark to unify them? Neutrino masses and unification in the light of  $(g-2)_\mu$ ,  $R_{D^{(*)}}$  and  $R_K$  anomalies”, *Nucl. Phys. B* **923** (2017) 324–338, [arXiv:1611.04566 \[hep-ph\]](#).
- [57] K. S. Babu and J. Julio, “Two-Loop Neutrino Mass Generation through Leptoquarks”, *Nucl. Phys. B* **841** (2010) 130–156, [arXiv:1006.1092 \[hep-ph\]](#).
- [58] V. D. Barger and K.-m. Cheung, “Atomic parity violation, leptoquarks, and contact interactions”, *Phys. Lett. B* **480** (2000) 149–154, [arXiv:hep-ph/0002259 \[hep-ph\]](#).
- [59] P. Herczeg, “CP-violating electron-nucleon interactions from leptoquark exchange”, *Phys. Rev. D* **68** (Dec, 2003) 116004.  
<https://link.aps.org/doi/10.1103/PhysRevD.68.116004>.
- [60] H. Georgi and S. L. Glashow, “Unity of all elementary-particle forces”, *Phys. Rev. Lett.* **32** (Feb, 1974) 438–441.
- [61] J. C. Pati and A. Salam, “Lepton number as the fourth ‘colour’”, *Phys. Rev. D* **10** (1974) 275–289.
- [62] H. Fritzsch and P. Minkowski, “Unified interactions of leptons and hadrons”, *Annals of Physics* **93** no. 1, (1975) 193 – 266.
- [63] H. Georgi, “The state of the art—gauge theories”, *AIP Conference Proceedings* **23** no. 1, (1975) 575–582,  
<https://aip.scitation.org/doi/pdf/10.1063/1.2947450>.  
<https://aip.scitation.org/doi/abs/10.1063/1.2947450>.
- [64] J. L. Hewett and T. G. Rizzo, “Low-Energy Phenomenology of Superstring Inspired E(6) Models”, *Phys. Rept.* **183** (1989) 193.
- [65] C. S. Aulakh and A. Girdhar, “SO(10) a la Pati-Salam”, *Int. J. Mod. Phys. A* **20** (2005) 865–894, [arXiv:hep-ph/0204097](#).

- [66] I. A. D’Souza and C. S. Kalman, *Preons: Models of leptons, quarks and gauge bosons as composite objects*. World Scientific, Singapore, 1992.
- [67] B. Schrempp and F. Schrempp, “Light leptoquarks”, *Physics Letters B* **153** no. 1, (1985) 101–107.  
<https://www.sciencedirect.com/science/article/pii/0370269385914509>.
- [68] E. Farhi and L. Susskind, “Technicolour”, *Physics Reports* **74** no. 3, (1981) 277–321.  
<https://www.sciencedirect.com/science/article/pii/0370157381901733>.
- [69] K. Lane and M. V. Ramana, “Walking technicolor signatures at hadron colliders”, *Phys. Rev. D* **44** (Nov, 1991) 2678–2700.  
<https://link.aps.org/doi/10.1103/PhysRevD.44.2678>.
- [70] W. Buchmüller, R. Rückl, and D. Wyler *Phys. Lett. B* **448** (1999) 320.
- [71] J. L. Hewett and T. G. Rizzo, “Much ado about leptoquarks: A comprehensive analysis”, *Phys. Rev. D* **56** (Nov, 1997) 5709–5724.  
<https://link.aps.org/doi/10.1103/PhysRevD.56.5709>.
- [72] W. Buchmüller, R. Rückl, and D. Wyler, “Leptoquarks in lepton-quark collisions”, *Phys.Lett.* **B191** (1986) 442–448. *Erratum ibid.* B448:320, 1999.
- [73] J. Alwall, M.-P. Le, M. Lisanti, and J. G. Wacker, “Searching for directly decaying gluinos at the Tevatron”, *Phys. Lett. B* **666** (2008) 34, [arXiv:0803.0019](https://arxiv.org/abs/0803.0019) [hep-ph].
- [74] J. Alwall, P. Schuster, and N. Toro, “Simplified models for a first characterization of new physics at the LHC”, *Phys. Rev. D* **79** (2009) 075020, [arXiv:0810.3921](https://arxiv.org/abs/0810.3921) [hep-ph].
- [75] D. Alves *et al.*, “Simplified models for LHC new physics searches”, *J. Phys. G* **39** (2012) 105005, [arXiv:1105.2838](https://arxiv.org/abs/1105.2838) [hep-ph].
- [76] K. Inoue, A. Kakuto, H. Komatsu, and S. Takeshita, “Aspects of Grand Unified Models with Softly Broken Supersymmetry”, *Prog. Theor. Phys.* **68** (1982) 927.
- [77] J. R. Ellis and S. Rudaz, “Search for supersymmetry in toponium decays”, *Phys. Lett. B* **128** (1983) 248.
- [78] ATLAS Collaboration, “Search for a scalar partner of the top quark in the all-hadronic  $t\bar{t}$  plus missing transverse momentum final state at  $\sqrt{s} = 13$  TeV with the ATLAS detector”, *Eur. Phys. J. C* **80** (2020) 737, [arXiv:2004.14060](https://arxiv.org/abs/2004.14060) [hep-ex].

- 
- [79] ATLAS Collaboration, “Search for new phenomena with top quark pairs in final states with one lepton, jets, and missing transverse momentum in  $pp$  collisions at  $\sqrt{s} = 13$  TeV with the ATLAS detector”. ATLAS-CONF-2020-003, 2020. <https://cds.cern.ch/record/2711489>.
- [80] ATLAS Collaboration, “Search for new phenomena in events with two opposite-charge leptons, jets and missing transverse momentum in  $pp$  collisions at  $\sqrt{s} = 13$  TeV with the ATLAS detector”. ATLAS-CONF-2020-046, 2020. <https://cds.cern.ch/record/2728056>.
- [81] The LEP SUSY Working Group and ALEPH, DELPHI, L3, OPAL experiments, “Combined LEP selectron/smuon/stau results, 183-208 GeV”. [http://lepsusy.web.cern.ch/lepsusy/www/sleptons\\_summer04/slep\\_final.html](http://lepsusy.web.cern.ch/lepsusy/www/sleptons_summer04/slep_final.html), Mar, 2016. last visited on 2021-02-12.
- [82] ATLAS Collaboration, “Search for top squarks decaying to tau sleptons in  $pp$  collisions at  $\sqrt{s} = 13$  TeV with the ATLAS detector”, *Phys. Rev. D* **98** (2018) 032008, [arXiv:1803.10178](https://arxiv.org/abs/1803.10178) [hep-ex].
- [83] ATLAS Collaboration, “Search for direct top squark pair production in final states with two tau leptons in  $pp$  collisions at  $\sqrt{s} = 8$  TeV with the ATLAS detector”, *Eur. Phys. J. C* **76** (2016) 81, [arXiv:1509.04976](https://arxiv.org/abs/1509.04976) [hep-ex].
- [84] B. Schachtner, *Search for top-squark pair production with the LHC experiment ATLAS in final states with b-quarks and tau leptons*. PhD thesis, Ludwig-Maximilians-Universität München, February, 2018.
- [85] CMS Collaboration, “Search for supersymmetry in proton–proton collisions at 13 TeV in final states with jets and missing transverse momentum”, *JHEP* **10** (2019) 244, [arXiv:1908.04722](https://arxiv.org/abs/1908.04722) [hep-ex].
- [86] T. Mandal, S. Mitra, and S. Seth, “Pair production of scalar leptoquarks at the LHC to NLO parton shower accuracy”, *Phys. Rev. D* **93** no. 3, (2016) 035018, [arXiv:1506.07369](https://arxiv.org/abs/1506.07369) [hep-ph].
- [87] ATLAS Collaboration, “Search for new phenomena in final states with  $b$ -jets and missing transverse momentum in  $\sqrt{s} = 13$  TeV  $pp$  collisions with the ATLAS detector”, [arXiv:2101.12527](https://arxiv.org/abs/2101.12527) [hep-ex].
- [88] ATLAS Collaboration, “Search for pair production of third-generation scalar leptoquarks decaying into a top quark and a  $\tau$ -lepton in  $pp$  collisions at  $\sqrt{s} = 13$  TeV with the ATLAS detector”, [arXiv:2101.11582](https://arxiv.org/abs/2101.11582) [hep-ex].
- [89] I. Doršner, S. Fajfer, A. Greljo, J. Kamenik, and N. Košnik, “Physics of leptoquarks in precision experiments and at particle colliders”, *Physics Reports* **641** (Jun, 2016) 1–68. <http://dx.doi.org/10.1016/j.physrep.2016.06.001>.

- [90] A. Belyaev, C. Leroy, R. Mehdiyev, and A. Pukhov, “Leptoquark single and pair production at lhc with calchep/comphep in the complete model”, [arXiv:hep-ph/0502067](https://arxiv.org/abs/hep-ph/0502067).
- [91] C. Borschensky, B. Fuks, A. Kulesza, and D. Schwartländer, “Scalar leptoquark pair production at hadron colliders”, *Phys. Rev. D* **101** no. 11, (2020) 115017, [arXiv:2002.08971](https://arxiv.org/abs/2002.08971) [hep-ph].
- [92] ATLAS Collaboration, “Searches for third-generation scalar leptoquarks in  $\sqrt{s} = 13$  TeV  $pp$  collisions with the ATLAS detector”, *JHEP* **06** (2019) 144, [arXiv:1902.08103](https://arxiv.org/abs/1902.08103) [hep-ex].
- [93] ATLAS Collaboration, “Searches for scalar leptoquarks and differential cross-section measurements in dilepton–dijet events in proton–proton collisions at a centre-of-mass energy of  $\sqrt{s} = 13$  TeV with the ATLAS experiment”, *Eur. Phys. J. C* **79** (2019) 733, [arXiv:1902.00377](https://arxiv.org/abs/1902.00377) [hep-ex].
- [94] L. Evans and P. Bryant, “LHC Machine”, *JINST* **3** (2008) S08001.
- [95] E. Mobs, “The CERN accelerator complex - August 2018. Complexe des accélérateurs du CERN - Août 2018” . <http://cds.cern.ch/record/2636343>. General Photo.
- [96] M. Benedikt, P. Collier, V. Mertens, J. Poole, and K. Schindl, *LHC Design Report*. CERN Yellow Reports: Monographs. CERN, Geneva, 2004. <https://cds.cern.ch/record/823808>.
- [97] E. Todesco and J. Wenninger, “Large hadron collider momentum calibration and accuracy”, *Phys. Rev. Accel. Beams* **20** (2017) 081003.
- [98] ATLAS Collaboration, “The ATLAS experiment at the CERN large hadron collider”, *Journal of Instrumentation* **3** no. 08, (Aug, 2008) S08003–S08003. <https://doi.org/10.1088/1748-0221/3/08/s08003>.
- [99] ALICE Collaboration, “The ALICE experiment at the CERN LHC”, *Journal of Instrumentation* **3** no. 08, (Aug, 2008) S08002–S08002. <https://doi.org/10.1088/1748-0221/3/08/s08002>.
- [100] CMS Collaboration, “The CMS experiment at the CERN LHC”, *Journal of Instrumentation* **3** no. 08, (Aug, 2008) S08004–S08004. <https://doi.org/10.1088/1748-0221/3/08/s08004>.
- [101] LHCb Collaboration, “The LHCb detector at the LHC”, *Journal of Instrumentation* **3** no. 08, (Aug, 2008) S08005–S08005. <https://doi.org/10.1088/1748-0221/3/08/s08005>.
- [102] ATLAS Collaboration, “The ATLAS Experiment at the CERN Large Hadron Collider”, *JINST* **3** (2008) S08003.

- 
- [103] J. Pequenao, “Computer generated image of the whole ATLAS detector”, Mar, 2008. <https://cds.cern.ch/record/1095924>.
- [104] ATLAS Collaboration, “ATLAS Inner Detector: Technical Design Report, Volume 1”, 1997. <https://cds.cern.ch/record/331063>.
- [105] ATLAS Collaboration, “ATLAS Inner Detector: Technical Design Report, Volume 2”, 1997. <https://cds.cern.ch/record/331064>.
- [106] ATLAS Collaboration, “ATLAS Insertable B-Layer: Technical Design Report”, 2010. <https://cds.cern.ch/record/1291633>.
- [107] ATLAS Collaboration, “The upgraded Pixel detector and the commissioning of the Inner Detector tracking of the ATLAS experiment for Run-2 at the Large Hadron Collider”, Tech. Rep. ATL-PHYS-PROC-2016-104, CERN, Geneva, Aug, 2016. <http://cds.cern.ch/record/2209070>. 15 pages, EPS-HEP 2015 Proceedings.
- [108] A. Vogel, “ATLAS Transition Radiation Tracker (TRT): Straw Tube Gaseous Detectors at High Rates”, Tech. Rep. ATL-INDET-PROC-2013-005, CERN, Geneva, Apr, 2013. <https://cds.cern.ch/record/1537991>.
- [109] J. Pequenao, “Computer Generated image of the ATLAS calorimeter”, Mar, 2008. <https://cds.cern.ch/record/1095927>.
- [110] ATLAS Collaboration, “Performance of the ATLAS muon trigger in  $pp$  collisions at  $\sqrt{s} = 8$  TeV”, *Eur. Phys. J. C* **75** (2015) 120, [arXiv:1408.3179](https://arxiv.org/abs/1408.3179) [hep-ex].
- [111] ATLAS Collaboration, “Performance of the ATLAS trigger system in 2015”, *Eur. Phys. J. C* **77** (2017) 317, [arXiv:1611.09661](https://arxiv.org/abs/1611.09661) [hep-ex].
- [112] ATLAS Collaboration, “2015 start-up trigger menu and initial performance assessment of the ATLAS trigger using Run-2 data”. ATL-DAQ-PUB-2016-001, 2016. <https://cds.cern.ch/record/2136007>.
- [113] ATLAS Collaboration, “Trigger Menu in 2016”. ATL-DAQ-PUB-2017-001, 2017. <https://cds.cern.ch/record/2242069>.
- [114] ATLAS Collaboration, “Trigger Menu in 2017”. ATL-DAQ-PUB-2018-002, 2018. <https://cds.cern.ch/record/2625986>.
- [115] ATLAS Collaboration, “Trigger Menu in 2018”. ATL-DAQ-PUB-2019-001, 2019. <https://cds.cern.ch/record/2693402>.
- [116] ATLAS Collaboration, “ATLAS Level-1 Trigger: Technical Design Report”, 1998. <https://cds.cern.ch/record/381429>.

- [117] ATLAS Collaboration, “ATLAS High-Level Trigger, Data Acquisition and Controls: Technical Design Report”, 2003.  
<https://cds.cern.ch/record/616089>.
- [118] CERN, *CAS - CERN Accelerator School: Intermediate Accelerator Physics: Zeuthen, Germany 15 - 26 Sep 2003*. *CAS - CERN Accelerator School: Intermediate Course on Accelerator Physics*. CERN, Geneva, 2006.  
<https://cds.cern.ch/record/603056>. pp. 361–378.
- [119] C. Pralavorio, “Record luminosity: well done LHC”. <https://home.cern/news/news/accelerators/record-luminosity-well-done-lhc>. last visited on 2021-02-10.
- [120] G. Avoni *et al.*, “The new lucid-2 detector for luminosity measurement and monitoring in atlas”, *JINST* **13** no. 07, (2018) P07017.
- [121] S. van der Meer, “Calibration of the effective beam height in the ISR”, Tech. Rep. CERN-ISR-PO-68-31. ISR-PO-68-31, CERN, Geneva, 1968.  
<http://cds.cern.ch/record/296752>.
- [122] ATLAS Collaboration, “ATLAS data quality operations and performance for 2015–2018 data-taking”, *JINST* **15** (2020) P04003, [arXiv:1911.04632](https://arxiv.org/abs/1911.04632) [physics.ins-det].
- [123] A. Roodman, “Blind analysis in particle physics”, [arXiv:physics/0312102](https://arxiv.org/abs/physics/0312102).
- [124] M. Baak, G. Besjes, D. Côté, A. Koutsman, J. Lorenz, and D. Short, “HistFitter software framework for statistical data analysis”, *Eur. Phys. J. C* **75** (2015) 153, [arXiv:1410.1280](https://arxiv.org/abs/1410.1280) [hep-ex].
- [125] A. Buckley, J. Butterworth, S. Gieseke, D. Grellscheid, S. Hoche, H. Hoeth, F. Krauss, L. Lonnblad, E. Nurse, P. Richardson, S. Schumann, M. H. Seymour, T. Sjostrand, P. Skands, and B. Webber, “General-purpose event generators for LHC physics”, [arXiv:1101.2599](https://arxiv.org/abs/1101.2599).
- [126] ATLAS Collaboration, “The ATLAS Simulation Infrastructure”, *Eur. Phys. J. C* **70** (2010) 823, [arXiv:1005.4568](https://arxiv.org/abs/1005.4568) [physics.ins-det].
- [127] J. C. Collins, D. E. Soper, and G. Sterman, “Factorization of hard processes in qcd”, [arXiv:hep-ph/0409313](https://arxiv.org/abs/hep-ph/0409313).
- [128] D. Amati and G. Veneziano, “Preconfinement as a property of perturbative qcd”, *Physics Letters B* **83** no. 1, (1979) 87 – 92.  
<http://www.sciencedirect.com/science/article/pii/0370269379908967>.
- [129] A. D. Martin, W. J. Stirling, R. S. Thorne, and G. Watt, “Parton distributions for the LHC”, *Eur. Phys. J. C* **63** (2009) 189–285, [arXiv:0901.0002](https://arxiv.org/abs/0901.0002) [hep-ph].

- 
- [130] ATLAS Collaboration, “ATLAS Pythia 8 tunes to 7 TeV data”. ATL-PHYS-PUB-2014-021, 2014. <https://cds.cern.ch/record/1966419>.
- [131] S. Agostinelli *et al.*, “GEANT4 – a simulation toolkit”, *Nucl. Instrum. Meth. A* **506** (2003) 250.
- [132] ATLAS Collaboration, “Fast Simulation for ATLAS: Atfast-II and ISF”, *J. Phys. Conf. Ser.* **396** (2012) 022031.
- [133] T. Sjöstrand, S. Mrenna, and P. Skands, “A brief introduction to PYTHIA 8.1”, *Comput. Phys. Commun.* **178** (2008) 852–867, [arXiv:0710.3820](https://arxiv.org/abs/0710.3820) [hep-ph].
- [134] R. D. Ball *et al.*, “Parton distributions with LHC data”, *Nucl. Phys. B* **867** (2013) 244, [arXiv:1207.1303](https://arxiv.org/abs/1207.1303) [hep-ph].
- [135] ATLAS Collaboration, “The Pythia 8 A3 tune description of ATLAS minimum bias and inelastic measurements incorporating the Donnachie–Landshoff diffractive model”. ATL-PHYS-PUB-2016-017, 2016. <https://cds.cern.ch/record/2206965>.
- [136] G. Cowan, “Error analysis with weighted events”, tech. rep., June, 2014. [https://www.pp.rhul.ac.uk/~cowan/stat/notes/errors\\_with\\_weights.pdf](https://www.pp.rhul.ac.uk/~cowan/stat/notes/errors_with_weights.pdf).
- [137] S. Frixione, P. Nason, and G. Ridolfi, “A positive-weight next-to-leading-order Monte Carlo for heavy flavour hadroproduction”, *JHEP* **09** (2007) 126, [arXiv:0707.3088](https://arxiv.org/abs/0707.3088) [hep-ph].
- [138] P. Nason, “A new method for combining NLO QCD with shower Monte Carlo algorithms”, *JHEP* **11** (2004) 040, [arXiv:hep-ph/0409146](https://arxiv.org/abs/hep-ph/0409146).
- [139] S. Frixione, P. Nason, and C. Oleari, “Matching NLO QCD computations with parton shower simulations: the POWHEG method”, *JHEP* **11** (2007) 070, [arXiv:0709.2092](https://arxiv.org/abs/0709.2092) [hep-ph].
- [140] S. Alioli, P. Nason, C. Oleari, and E. Re, “A general framework for implementing NLO calculations in shower Monte Carlo programs: the POWHEG BOX”, *JHEP* **06** (2010) 043, [arXiv:1002.2581](https://arxiv.org/abs/1002.2581) [hep-ph].
- [141] T. Sjöstrand, S. Ask, J. R. Christiansen, R. Corke, N. Desai, P. Ilten, S. Mrenna, S. Prestel, C. O. Rasmussen, and P. Z. Skands, “An introduction to PYTHIA 8.2”, *Comput. Phys. Commun.* **191** (2015) 159, [arXiv:1410.3012](https://arxiv.org/abs/1410.3012) [hep-ph].
- [142] M. Czakon and A. Mitov, “Top++: A program for the calculation of the top-pair cross-section at hadron colliders”, *Comput. Phys. Commun.* **185** (2014) 2930, [arXiv:1112.5675](https://arxiv.org/abs/1112.5675) [hep-ph].

- [143] R. D. Ball *et al.*, “Parton distributions for the LHC run II”, *JHEP* **04** (2015) 040, [arXiv:1410.8849 \[hep-ph\]](#).
- [144] E. Re, “Single-top  $Wt$ -channel production matched with parton showers using the POWHEG method”, *Eur. Phys. J. C* **71** (2011) 1547, [arXiv:1009.2450 \[hep-ph\]](#).
- [145] M. Aliev, H. Lacker, U. Langenfeld, S. Moch, P. Uwer, and M. Wiedermann, “HATHOR – HAdronic Top and Heavy quarks crOss section calculatoR”, *Comput. Phys. Commun.* **182** (2011) 1034–1046, [arXiv:1007.1327 \[hep-ph\]](#).
- [146] P. Kant, O. M. Kind, T. Kintscher, T. Lohse, T. Martini, S. Mölbitz, P. Rieck, and P. Uwer, “HatHor for single top-quark production: Updated predictions and uncertainty estimates for single top-quark production in hadronic collisions”, *Comput. Phys. Commun.* **191** (2015) 74–89, [arXiv:1406.4403 \[hep-ph\]](#).
- [147] N. Kidonakis, “Two-loop soft anomalous dimensions for single top quark associated production with a  $W^-$  or  $H^-$ ”, *Phys. Rev. D* **82** (2010) 054018, [arXiv:1005.4451 \[hep-ph\]](#).
- [148] N. Kidonakis, “Top Quark Production”, in *Proceedings, Helmholtz International Summer School on Physics of Heavy Quarks and Hadrons (HQ 2013): JINR, Dubna, Russia, July 15-28, 2013*, pp. 139–168. 2014. [arXiv:1311.0283 \[hep-ph\]](#).
- [149] E. Bothmann *et al.*, “Event generation with Sherpa 2.2”, *SciPost Phys.* **7** no. 3, (2019) 034, [arXiv:1905.09127 \[hep-ph\]](#).
- [150] C. Anastasiou, L. J. Dixon, K. Melnikov, and F. Petriello, “High precision QCD at hadron colliders: Electroweak gauge boson rapidity distributions at next-to-next-to leading order”, *Phys. Rev. D* **69** (2004) 094008, [arXiv:hep-ph/0312266](#).
- [151] T. Gleisberg and S. Höche, “Comix, a new matrix element generator”, *JHEP* **12** (2008) 039, [arXiv:0808.3674 \[hep-ph\]](#).
- [152] S. Schumann and F. Krauss, “A parton shower algorithm based on Catani–Seymour dipole factorisation”, *JHEP* **03** (2008) 038, [arXiv:0709.1027 \[hep-ph\]](#).
- [153] ATLAS Collaboration, “Multi-Boson Simulation for 13 TeV ATLAS Analyses”. ATL-PHYS-PUB-2017-005, 2017. <https://cds.cern.ch/record/2261933>.
- [154] J. Alwall, R. Frederix, S. Frixione, V. Hirschi, F. Maltoni, O. Mattelaer, H. S. Shao, T. Stelzer, P. Torrielli, and M. Zaro, “The automated computation of tree-level and next-to-leading order differential cross sections, and their

- matching to parton shower simulations”, *JHEP* **07** (2014) 079, [arXiv:1405.0301 \[hep-ph\]](#).
- [155] ATLAS Collaboration, “Modelling of the  $t\bar{t}H$  and  $t\bar{t}V(V = W, Z)$  processes for  $\sqrt{s} = 13$  TeV ATLAS analyses”. ATL-PHYS-PUB-2016-005, 2016. <https://cds.cern.ch/record/2120826>.
- [156] H. B. Hartanto, B. Jäger, L. Reina, and D. Wackerroth, “Higgs boson production in association with top quarks in the POWHEG BOX”, *Phys. Rev. D* **91** no. 9, (2015) 094003, [arXiv:1501.04498 \[hep-ph\]](#).
- [157] D. J. Lange, “The EvtGen particle decay simulation package”, *Nucl. Instrum. Meth. A* **462** (2001) 152.
- [158] S. Frixione, E. Laenen, P. Motylinski, C. White, and B. R. Webber, “Single-top hadroproduction in association with a  $W$  boson”, *JHEP* **07** (2008) 029, [arXiv:0805.3067 \[hep-ph\]](#).
- [159] ATLAS Collaboration, “Simulation of top-quark production for the ATLAS experiment at  $\sqrt{s} = 13$  TeV”. ATL-PHYS-PUB-2016-004, 2016. <https://cds.cern.ch/record/2120417>.
- [160] ATLAS Collaboration, “Studies on top-quark Monte Carlo modelling for Top2016”. ATL-PHYS-PUB-2016-020, 2016. <https://cds.cern.ch/record/2216168>.
- [161] T. Ježo, J. M. Lindert, P. Nason, C. Oleari, and S. Pozzorini, “An NLO+PS generator for  $t\bar{t}$  and  $Wt$  production and decay including non-resonant and interference effects”, *Eur. Phys. J. C* **76** no. 12, (2016) 691, [arXiv:1607.04538 \[hep-ph\]](#).
- [162] P. Artoisenet, R. Frederix, O. Mattelaer, and R. Rietkerk, “Automatic spin-entangled decays of heavy resonances in Monte Carlo simulations”, *JHEP* **03** (2013) 015, [arXiv:1212.3460 \[hep-ph\]](#).
- [163] L. Lönnblad, “Correcting the Colour-Dipole Cascade Model with Fixed Order Matrix Elements”, *JHEP* **05** (2002) 046, [arXiv:hep-ph/0112284](#).
- [164] L. Lönnblad and S. Prestel, “Matching tree-level matrix elements with interleaved showers”, *JHEP* **03** (2012) 019, [arXiv:1109.4829 \[hep-ph\]](#).
- [165] W. Beenakker, C. Borschensky, M. Krämer, A. Kulesza, and E. Laenen, “NNLL-fast: predictions for coloured supersymmetric particle production at the LHC with threshold and Coulomb resummation”, *JHEP* **12** (2016) 133, [arXiv:1607.07741 \[hep-ph\]](#).

- [166] W. Beenakker, M. Krämer, T. Plehn, M. Spira, and P. Zerwas, “Stop production at hadron colliders”, *Nucl. Phys. B* **515** (1998) 3–14, [arXiv:hep-ph/9710451](#).
- [167] W. Beenakker, S. Brensing, M. Krämer, A. Kulesza, E. Laenen, and I. Niessen, “Supersymmetric top and bottom squark production at hadron colliders”, *JHEP* **08** (2010) 098, [arXiv:1006.4771 \[hep-ph\]](#).
- [168] W. Beenakker, C. Borschensky, R. Heger, M. Krämer, A. Kulesza, and E. Laenen, “NNLL resummation for stop pair-production at the LHC”, *JHEP* **05** (2016) 153, [arXiv:1601.02954 \[hep-ph\]](#).
- [169] LHC SUSY Cross Section Working Group, “LHC Physics Web: Stop-antistop (sbottom-antisbottom) production cross sections”. <https://twiki.cern.ch/twiki/bin/view/LHCPhysics/SUSYCrossSections13TeVstopsbottom>. last visited on 2021-01-26.
- [170] ATLAS Collaboration, “Performance of the ATLAS Inner Detector Track and Vertex Reconstruction in High Pile-Up LHC Environment”. ATLAS-CONF-2012-042, 2012. <https://cds.cern.ch/record/1435196>.
- [171] R. Frühwirth, “Application of Kalman filtering to track and vertex fitting”, *Nucl. Instrum. Meth. A* **262** (1987) 444–450.
- [172] ATLAS Collaboration, “A neural network clustering algorithm for the ATLAS silicon pixel detector”, *JINST* **9** (2014) P09009, [arXiv:1406.7690 \[hep-ex\]](#).
- [173] ATLAS Collaboration, “Vertex Reconstruction Performance of the ATLAS Detector at  $\sqrt{s} = 13$  TeV”. ATL-PHYS-PUB-2015-026, 2015. <https://cds.cern.ch/record/2037717>.
- [174] ATLAS Collaboration, “Primary vertex reconstruction at the ATLAS experiment”, *J. Phys. Conf. Ser.* **898** no. 4, (2017) 042056.
- [175] ATLAS Collaboration, “Topological cell clustering in the ATLAS calorimeters and its performance in LHC Run 1”, *Eur. Phys. J. C* **77** (2017) 490, [arXiv:1603.02934 \[hep-ex\]](#).
- [176] ATLAS Collaboration, “Jet reconstruction and performance using particle flow with the ATLAS Detector”, *Eur. Phys. J. C* **77** (2017) 466, [arXiv:1703.10485 \[hep-ex\]](#).
- [177] M. Cacciari, G. P. Salam, and G. Soyez, “The anti- $k_t$  jet clustering algorithm”, *JHEP* **04** (2008) 063, [arXiv:0802.1189 \[hep-ph\]](#).
- [178] ATLAS Collaboration, “Tagging and suppression of pileup jets with the ATLAS detector”. ATLAS-CONF-2014-018, 2014. <https://cds.cern.ch/record/1700870>.

- 
- [179] ATLAS Collaboration, “Performance of  $b$ -jet identification in the ATLAS experiment”, *JINST* **11** (2016) P04008, [arXiv:1512.01094 \[hep-ex\]](#).
- [180] ATLAS Collaboration, “ATLAS  $b$ -jet identification performance and efficiency measurement with  $t\bar{t}$  events in  $pp$  collisions at  $\sqrt{s} = 13$  TeV”, *Eur. Phys. J. C* **79** (2019) 970, [arXiv:1907.05120 \[hep-ex\]](#).
- [181] ATLAS Collaboration, “Optimisation and performance studies of the ATLAS  $b$ -tagging algorithms for the 2017-18 LHC run”. ATL-PHYS-PUB-2017-013, 2017. <https://cds.cern.ch/record/2273281>.
- [182] ATLAS Collaboration, “Expected performance of the 2019 ATLAS  $b$ -taggers”. <http://atlas.web.cern.ch/Atlas/GROUPS/PHYSICS/PLOTS/FTAG-2019-005/>. last visited on 2021-01-28.
- [183] ATLAS Collaboration, “Electron and photon performance measurements with the ATLAS detector using the 2015–2017 LHC proton–proton collision data”, *JINST* **14** (2019) P12006, [arXiv:1908.00005 \[hep-ex\]](#).
- [184] ATLAS Collaboration, “Muon reconstruction and identification efficiency in ATLAS using the full Run 2  $pp$  collision data set at  $\sqrt{s} = 13$  TeV”. ATLAS-CONF-2020-030, 2020. <https://cds.cern.ch/record/2725736>.
- [185] ATLAS Collaboration, “Muon reconstruction performance of the ATLAS detector in proton–proton collision data at  $\sqrt{s} = 13$  TeV”, *Eur. Phys. J. C* **76** no. 5, (2016) 292, [arXiv:1603.05598 \[hep-ex\]](#).
- [186] ATLAS Collaboration, “Identification of hadronic tau lepton decays using neural networks in the ATLAS experiment”. ATL-PHYS-PUB-2019-033, 2019. <https://cds.cern.ch/record/2688062>.
- [187] ATLAS Collaboration, “Local Hadronic Calibration”, tech. rep., 2008. <https://cds.cern.ch/record/1112035>.
- [188] ATLAS Collaboration, “Reconstruction of hadronic decay products of tau leptons with the ATLAS experiment”, *Eur. Phys. J. C* **76** (2016) 295, [arXiv:1512.05955 \[hep-ex\]](#).
- [189] ATLAS Collaboration, “Reconstruction, Energy Calibration, and Identification of Hadronically Decaying Tau Leptons in the ATLAS Experiment for Run-2 of the LHC”. ATL-PHYS-PUB-2015-045, 2015. <https://cds.cern.ch/record/2064383>.
- [190] ATLAS Collaboration, “Measurement of the tau lepton reconstruction and identification performance in the ATLAS experiment using  $pp$  collisions at  $\sqrt{s} = 13$  TeV”. ATLAS-CONF-2017-029, 2017. <https://cds.cern.ch/record/2261772>.

- [191] ATLAS Collaboration, “Identification and energy calibration of hadronically decaying tau leptons with the ATLAS experiment in  $pp$  collisions at  $\sqrt{s} = 8$  TeV”, *Eur. Phys. J. C* **75** (2015) 303, [arXiv:1412.7086 \[hep-ex\]](#).
- [192] M. Cacciari and G. P. Salam, “Pileup subtraction using jet areas”, [arXiv:0707.1378](#).
- [193] ATLAS Collaboration, “ $E_T^{\text{miss}}$  performance in the ATLAS detector using 2015–2016 LHC  $pp$  collisions”. ATLAS-CONF-2018-023, 2018. <https://cds.cern.ch/record/2625233>.
- [194] ATLAS Collaboration, “Object-based missing transverse momentum significance in the ATLAS Detector”. ATLAS-CONF-2018-038, 2018. <https://cds.cern.ch/record/2630948>.
- [195] C. G. Lester and D. J. Summers, “Measuring masses of semi-invisibly decaying particles pair produced at hadron colliders”, *Phys. Lett. B* **463** (1999) 99–103, [arXiv:hep-ph/9906349 \[hep-ph\]](#).
- [196] C. G. Lester and B. Nachman, “Bisection-based asymmetric  $M_{T2}$  computation: a higher precision calculator than existing symmetric methods”, *JHEP* **03** (2015) 100, [arXiv:1411.4312 \[hep-ph\]](#).
- [197] ATLAS Collaboration, “The ATLAS Tau Trigger in Run 2”. ATLAS-CONF-2017-061, 2017. <https://cds.cern.ch/record/2274201>.
- [198] ATLAS Collaboration, “Selection of jets produced in 13 TeV proton–proton collisions with the ATLAS detector”. ATLAS-CONF-2015-029, 2015. <https://cds.cern.ch/record/2037702>.
- [199] K. Cranmer, “Statistical challenges for searches for new physics at the lhc”, [arXiv:physics/0511028](#).
- [200] G. Cowan, K. Cranmer, E. Gross, and O. Vitells, “Asymptotic formulae for likelihood-based tests of new physics”, *Eur. Phys. J. C* **71** (2011) 1554, [arXiv:1007.1727 \[physics.data-an\]](#).
- [201] K. Cranmer, G. Lewis, L. Moneta, A. Shibata, and W. Verkerke, “HistFactory: A tool for creating statistical models for use with RooFit and RooStats”, Tech. Rep. CERN-OPEN-2012-016, New York U., New York, Jan, 2012. <https://cds.cern.ch/record/1456844>.
- [202] W. Verkerke and D. Kirkby, “The RooFit toolkit for data modeling”, 2003. [arXiv:physics/0306116 \[physics.data-an\]](#).
- [203] L. Moneta, K. Belasco, K. Cranmer, S. Kreiss, A. Lazzaro, D. Piparo, G. Schott, W. Verkerke, and M. Wolf, “The RooStats Project”, [arXiv:1009.1003](#).

- 
- [204] A. L. Read, “Presentation of search results: the  $CL_S$  technique”, *J. Phys. G* **28** (2002) 2693.
- [205] G. Cowan, “Discovery sensitivity for a counting experiment with background uncertainty”, tech. rep., May, 2012.  
<http://www.pp.rhul.ac.uk/~cowan/stat/medsig/medsigNote.pdf>.
- [206] N. Hartmann, “ahoi: A horrible optimization instrument”.  
<https://pypi.org/project/ahoi/>.
- [207] C. R. Harris, K. J. Millman, S. J. van der Walt, R. Gommers, P. Virtanen, D. Cournapeau, E. Wieser, J. Taylor, S. Berg, N. J. Smith, R. Kern, M. Picus, S. Hoyer, M. H. van Kerkwijk, M. Brett, A. Haldane, J. F. del R’io, M. Wiebe, P. Peterson, P. G’erard-Marchant, K. Sheppard, T. Reddy, W. Weckesser, H. Abbasi, C. Gohlke, and T. E. Oliphant, “Array programming with NumPy”, *Nature* **585** no. 7825, (Sept., 2020) 357–362.  
<https://doi.org/10.1038/s41586-020-2649-2>.
- [208] ATLAS Collaboration, “Jet Calibration and Systematic Uncertainties for Jets Reconstructed in the ATLAS Detector at  $\sqrt{s} = 13$  TeV”.  
ATL-PHYS-PUB-2015-015, 2015. <https://cds.cern.ch/record/2037613>.
- [209] ATLAS Collaboration, “Jet energy scale measurements and their systematic uncertainties in proton–proton collisions at  $\sqrt{s} = 13$  TeV with the ATLAS detector”, *Phys. Rev. D* **96** (2017) 072002, [arXiv:1703.09665](https://arxiv.org/abs/1703.09665) [hep-ex].
- [210] ATLAS Collaboration, “A method for the construction of strongly reduced representations of ATLAS experimental uncertainties and the application thereof to the jet energy scale”. ATL-PHYS-PUB-2015-014, 2015.  
<https://cds.cern.ch/record/2037436>.
- [211] ATLAS Collaboration, “Measurements of  $b$ -jet tagging efficiency with the ATLAS detector using  $t\bar{t}$  events at  $\sqrt{s} = 13$  TeV”, *JHEP* **08** (2018) 089, [arXiv:1805.01845](https://arxiv.org/abs/1805.01845) [hep-ex].
- [212] ATLAS Collaboration, “Measurement of  $b$ -tagging efficiency of  $c$ -jets in  $t\bar{t}$  events using a likelihood approach with the ATLAS detector”.  
ATLAS-CONF-2018-001, 2018. <https://cds.cern.ch/record/2306649>.
- [213] ATLAS Collaboration, “Calibration of light-flavour  $b$ -jet mistagging rates using ATLAS proton–proton collision data at  $\sqrt{s} = 13$  TeV”.  
ATLAS-CONF-2018-006, 2018. <https://cds.cern.ch/record/2314418>.
- [214] ATLAS Collaboration, “Electron and photon energy calibration with the ATLAS detector using 2015–2016 LHC proton–proton collision data”, *JINST* **14** (2019) P03017, [arXiv:1812.03848](https://arxiv.org/abs/1812.03848) [hep-ex].

- [215] ATLAS Collaboration, “Muon reconstruction performance of the ATLAS detector in proton–proton collision data at  $\sqrt{s} = 13$  TeV”, *Eur. Phys. J. C* **76** (2016) 292, [arXiv:1603.05598 \[hep-ex\]](#).
- [216] ATLAS Collaboration, “Performance of missing transverse momentum reconstruction with the ATLAS detector using proton–proton collisions at  $\sqrt{s} = 13$  TeV”, *Eur. Phys. J. C* **78** (2018) 903, [arXiv:1802.08168 \[hep-ex\]](#).
- [217] ATLAS Collaboration, “Luminosity determination in  $pp$  collisions at  $\sqrt{s} = 13$  TeV using the ATLAS detector at the LHC”. ATLAS-CONF-2019-021, 2019. <https://cds.cern.ch/record/2677054>.
- [218] J. Butterworth *et al.*, “PDF4LHC recommendations for LHC Run II”, *J. Phys. G* **43** (2016) 023001, [arXiv:1510.03865 \[hep-ph\]](#).
- [219] ATLAS Collaboration, “Monte Carlo Generators for the Production of a  $W$  or  $Z/\gamma^*$  Boson in Association with Jets at ATLAS in Run 2”. ATL-PHYS-PUB-2016-003, 2016. <https://cds.cern.ch/record/2120133>.
- [220] S. Catani, F. Krauss, R. Kuhn, and B. R. Webber, “QCD Matrix Elements + Parton Showers”, *JHEP* **11** (2001) 063, [arXiv:hep-ph/0109231](#).
- [221] S. Höche, F. Krauss, S. Schumann, and F. Siegert, “QCD matrix elements and truncated showers”, *JHEP* **05** (2009) 053, [arXiv:0903.1219 \[hep-ph\]](#).
- [222] J. K. Anders and M. D’Onofrio, “V+Jets theoretical uncertainties estimation via a parameterisation method”, Tech. Rep. ATL-COM-PHYS-2016-044, CERN, Geneva, Jan, 2016. <https://cds.cern.ch/record/2125718>.
- [223] M. Bähr *et al.*, “Herwig++ physics and manual”, *Eur. Phys. J. C* **58** (2008) 639, [arXiv:0803.0883 \[hep-ph\]](#).
- [224] J. Bellm *et al.*, “Herwig 7.0/Herwig++ 3.0 release note”, *Eur. Phys. J. C* **76** no. 4, (2016) 196, [arXiv:1512.01178 \[hep-ph\]](#).
- [225] J. Butterworth, E. Dobson, U. Klein, B. Mellado Garcia, T. Nunnemann, J. Qian, D. Rebuffi, and R. Tanaka, “Single Boson and Diboson Production Cross Sections in  $pp$  Collisions at  $\sqrt{s}=7$  TeV”, Tech. Rep. ATL-COM-PHYS-2010-695, CERN, Geneva, Aug, 2010. <https://cds.cern.ch/record/1287902>.
- [226] ATLAS Collaboration, “Measurement of  $W^\pm$  and  $Z$  Boson Production Cross Sections in  $pp$  Collisions at  $\sqrt{s} = 13$  TeV with the ATLAS Detector”. ATLAS-CONF-2015-039, 2015. <https://cds.cern.ch/record/2045487>.
- [227] ATLAS Collaboration, “Multi-boson simulation for 13 TeV ATLAS analyses”. ATL-PHYS-PUB-2016-002, 2016. <https://cds.cern.ch/record/2119986>.

- 
- [228] K. Arnold, M. Bahr, G. Bozzi, F. Campanario, C. Englert, T. Figy, N. Greiner, C. Hackstein, V. Hankele, B. Jager, G. Klamke, M. Kubocz, C. Oleari, S. Platzer, S. Prestel, M. Worek, and D. Zeppenfeld, “Vbfno: A parton level monte carlo for processes with electroweak bosons”, [arXiv:0811.4559](#).
- [229] ATLAS Collaboration, “Measurement of the  $t\bar{t}Z$  and  $t\bar{t}W$  cross sections in proton–proton collisions at  $\sqrt{s} = 13$  TeV with the ATLAS detector”, *Phys. Rev. D* **99** (2019) 072009, [arXiv:1901.03584](#) [hep-ex].
- [230] D. de Florian *et al.*, “Handbook of LHC Higgs Cross Sections: 4. Deciphering the Nature of the Higgs Sector”, [arXiv:1610.07922](#) [hep-ph].
- [231] ATLAS Collaboration, “Measurement of the production cross-section of a single top quark in association with a  $Z$  boson in proton–proton collisions at 13 TeV with the ATLAS detector”, *Phys. Lett. B* **780** (2018) 557, [arXiv:1710.03659](#) [hep-ex].
- [232] ATLAS Collaboration, “Search for new phenomena in  $pp$  collisions in final states with tau leptons,  $b$ -jets, and missing transverse momentum with the ATLAS detector”. ATLAS-CONF-2021-008, 2021. <http://cds.cern.ch/record/2759282>.
- [233] G. Apollinari, O. Brüning, T. Nakamoto, and L. Rossi, “Chapter 1: High Luminosity Large Hadron Collider HL-LHC. High Luminosity Large Hadron Collider HL-LHC”, *CERN Yellow Report* no. [arXiv:1705.08830](#). 5, (May, 2017) 1–19. <https://cds.cern.ch/record/2120673>. 21 pages, chapter in High-Luminosity Large Hadron Collider (HL-LHC) : Preliminary Design Report.
- [234] D. Adams, *The Hitchhiker’s Guide to the Galaxy*. Harmony Books, New York, 1979.



# List of abbreviations

- BRW** Buchmüller-Rückl-Wyler (model)
- CERN** Conseil européen pour la recherche nucléaire (European Organization for Nuclear Research)
- CKM** Cabibbo–Kobayashi–Maskawa (matrix)
- CL** Confidence level
- CR** Control region
- CSC** Cathode Strip Chamber
- DR** Diagram removal
- DS** Diagram subtraction
- EM** Electromagnetic
- FSR** Final state radiation
- GMSB** Gauge-mediated symmetry breaking
- GUT** Grand Unified Theory
- HLT** High-level trigger
- IBL** Insertable B-Layer
- ID** Inner Detector
- IP** Interaction point
- ISR** Initial state radiation
- JER** Jet energy resolution
- JES** Jet energy scale
- JVT** Jet vertex tagger
- L1** Level-1 (trigger)
- LAr** Liquid Argon
- LEP** Large Electron–Positron (collider)
- LHC** Large Hadron Collider
- LO** Leading order

- LSP** Lightest supersymmetric particle
- LUCID–2** Luminosity Cherenkov Integrating Detector 2
- MC** Monte Carlo
- MDT** Monitored Drift Tube
- ME** Matrix element
- ML** Maximum likelihood
- MS** Muon Spectrometer
- NLO** Next-to-leading order
- NLSP** Next-to-lightest supersymmetric particle
- NNLL** Next-to-next-to-leading logarithmic
- NNLO<sub>approx</sub>** Approximate next-to-next-to-leading order
- PDF** Parton distribution function
- PS** Proton Synchrotron
- PSB** Proton Synchrotron Booster
- PV** Primary vertex
- QCD** Quantum chromodynamics
- RoI** Region-of-interest
- RPC** Resistive Plate Chamber
- SCT** Semiconductor Tracker
- SM** Standard Model (of particle physics)
- SPS** Super Proton Synchrotron
- SR** Signal region
- SUSY** Supersymmetry
- TGC** Thin Gap Chamber
- TRT** Transition Radiation Tracker
- UE** Underlying event
- VR** Validation region
- WIMP** Weakly interacting massive particle

# Appendix

## A Stop-stau exclusion limits per signal region

Figure A.1 shows the exclusion limits at 95 % CL for each channel separately: The pink contours are derived in an exclusion fit including all CRs and the di-tau SR, while the results from a fit using all CRs and the single-tau multi-bin SR are represented by the blue contours. The simultaneous usage of both SRs in the nominal fit setup extends the exclusion reach. Due to the slight deficit in data observed in the di-tau SR (cf. Table 9.3), the observed limit is slightly stronger than the expected one.

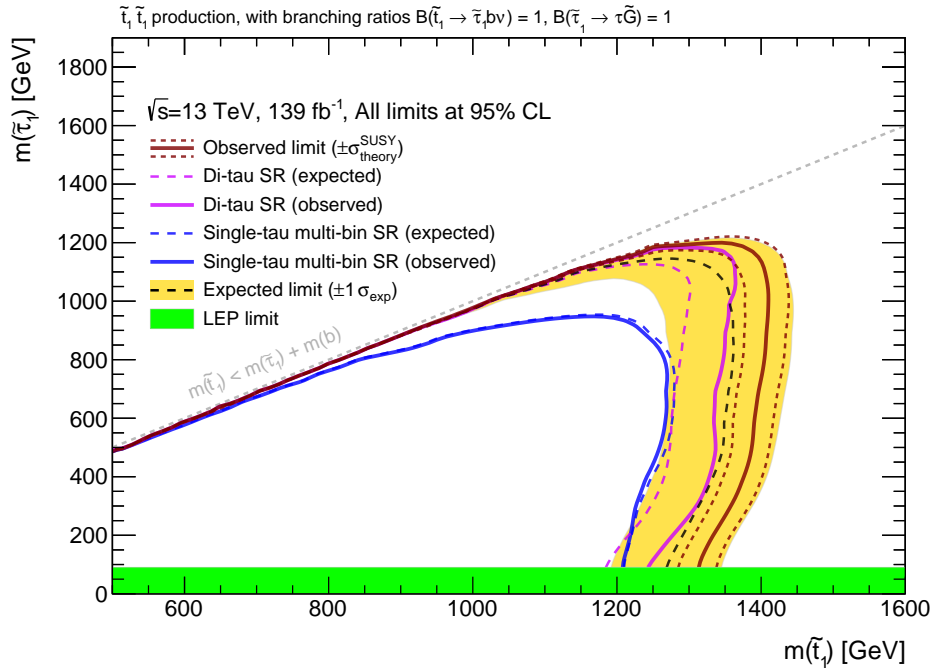


**Figure A.1:** Exclusion contours at 95 % confidence level for the stop-stau signal as a function of  $m(\tilde{t}_1)$  and  $m(\tilde{\tau}_1)$ . The pink (blue) dashed and solid lines show the expected and observed limits, respectively, derived in a fit including all CRs and only the di-tau (single-tau multi-bin) SR. The combined observed (solid red line) and expected limits (dashed black line) are derived in a fit including all CRs and both SRs simultaneously. The green band indicates the limit on the tau slepton mass from the LEP experiments [81].



## **B Additional data vs. MC comparison plots**

In the following, additional plots comparing kinematic distributions of data and MC simulation in the various selections defined in the analysis are shown. These plots supplement the ones shown in Section 9.1. The background expectation is scaled by the normalization factors obtained from the background-only fit. All statistical and systematic uncertainties are included.

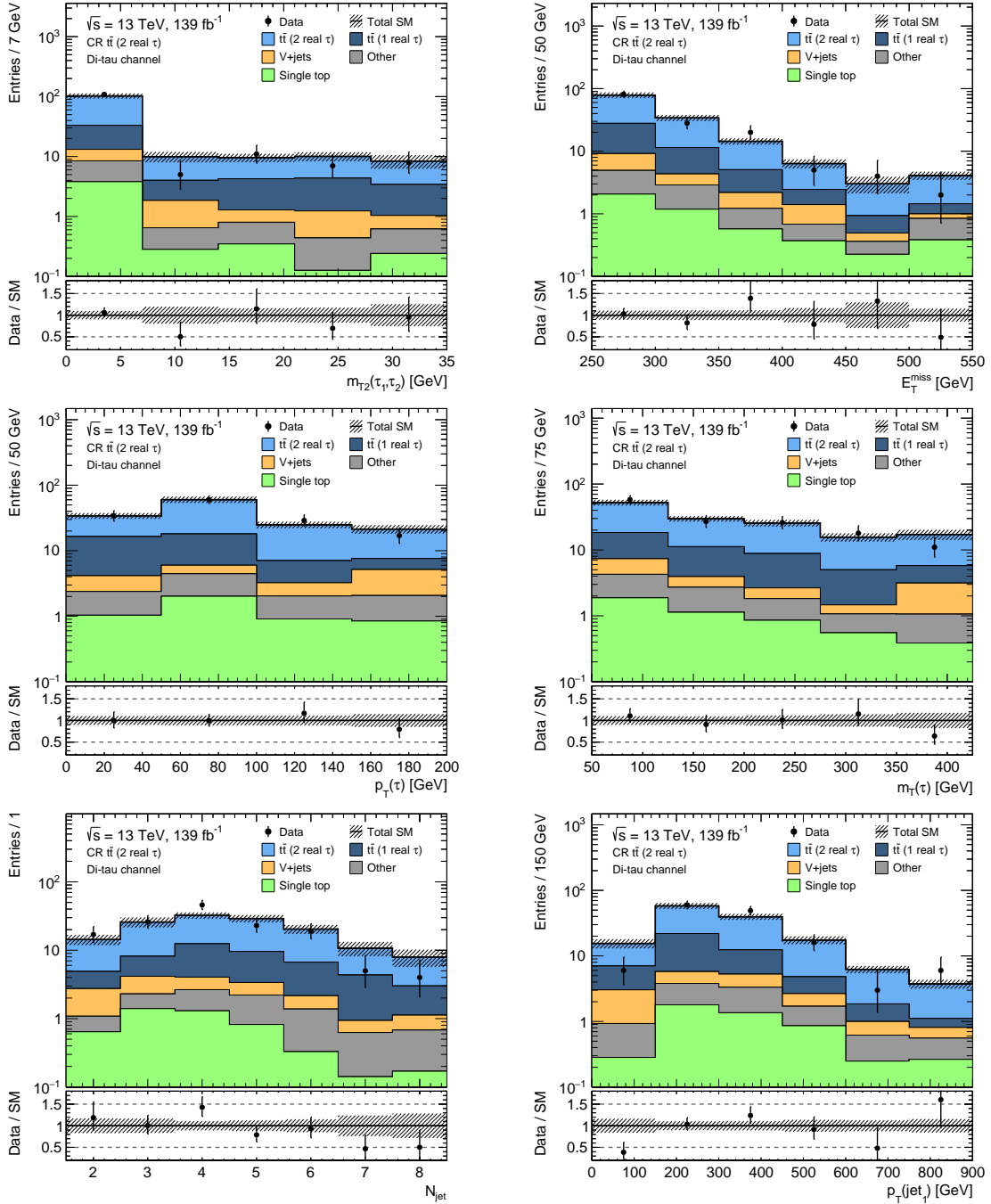


**Figure B.1:** Kinematic distributions in the  $t\bar{t}$  (2 real  $\tau$ ) CR in the di-tau channel. The stacked histograms show the various SM background contributions. The hatched band indicates the total statistical and systematic uncertainty of the background. The expected event yields are scaled with the respective normalization factors obtained from the background-only fit. Minor backgrounds are grouped together and denoted as ‘Other’. This includes  $t\bar{t}$ -fake,  $t\bar{t} + X$ , multiboson, and other top. The rightmost bin includes the overflowed events.

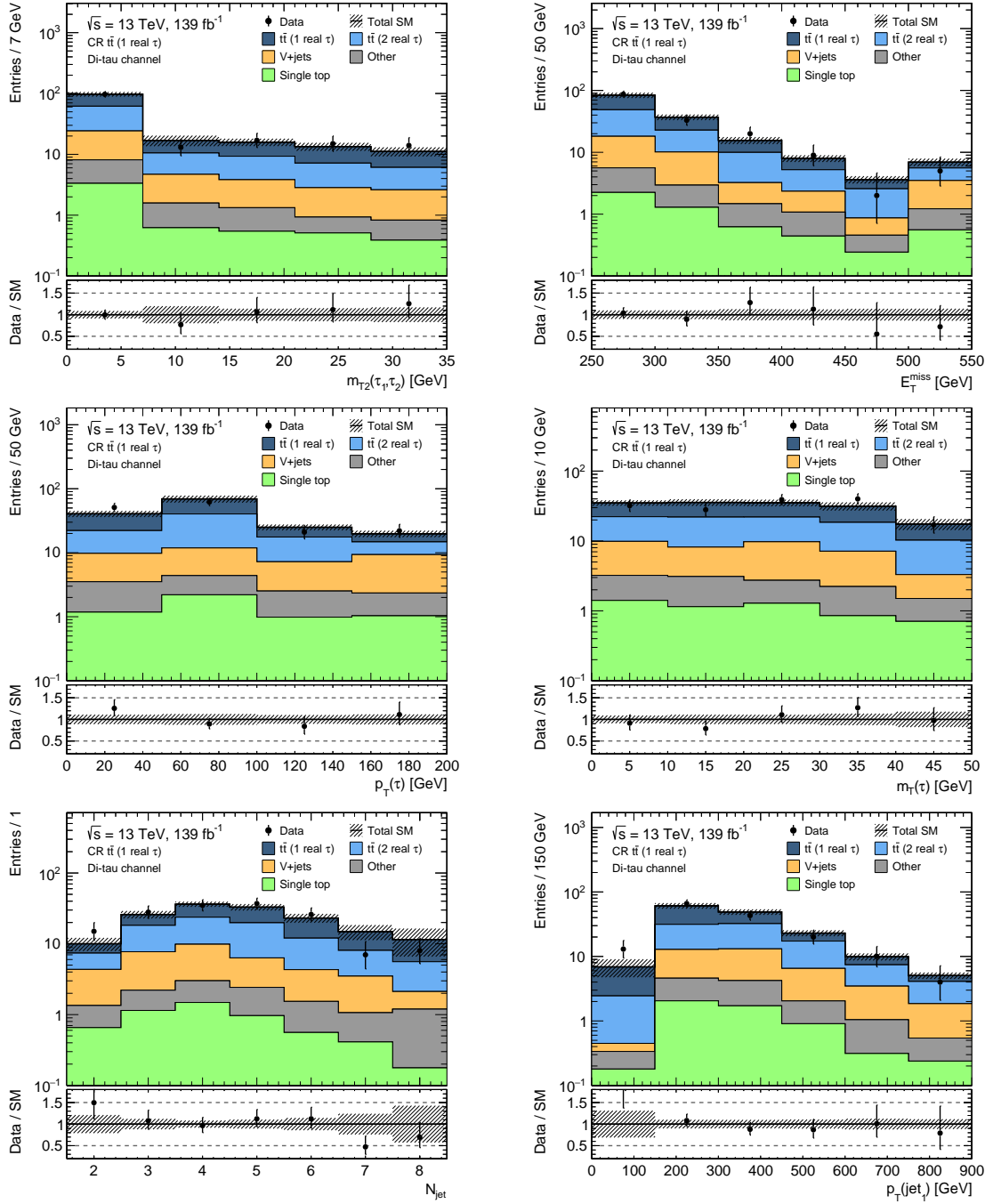


**Figure B.2:** Kinematic distributions in the  $t\bar{t}$  (1 real  $\tau$ ) CR in the di-tau channel. The stacked histograms show the various SM background contributions. The hatched band indicates the total statistical and systematic uncertainty of the background. The expected event yields are scaled with the respective normalization factors obtained from the background-only fit. Minor backgrounds are grouped together and denoted as ‘Other’. This includes  $t\bar{t}$ -fake,  $t\bar{t} + X$ , multiboson, and other top. The rightmost bin includes the overflowed events.

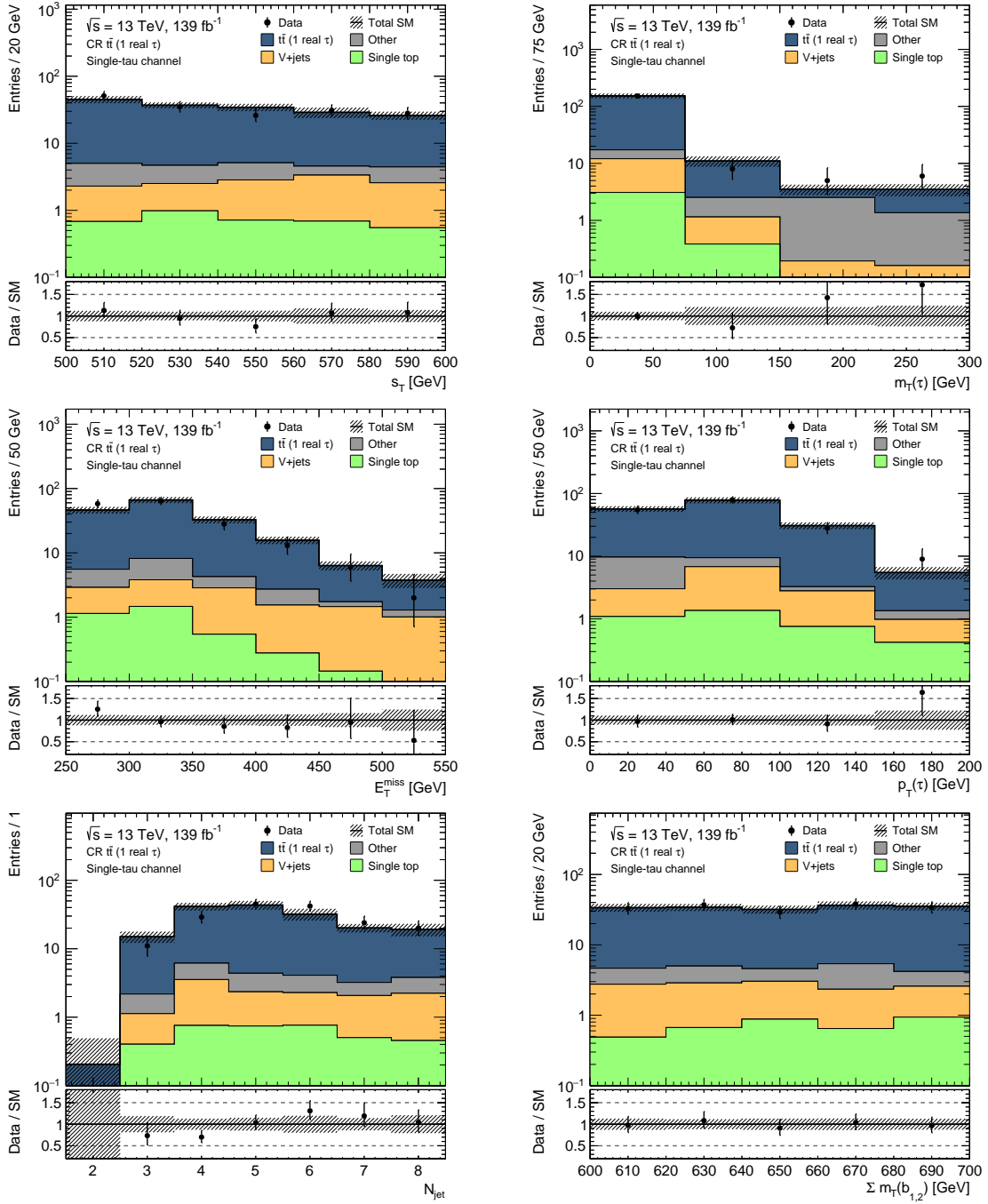


**Figure B.3:** Kinematic distributions in the  $t\bar{t}$  (1 real  $\tau$ ) CR in the single-tau channel. The stacked histograms show the various SM background contributions. The hatched band indicates the total statistical and systematic uncertainty of the background. The expected event yields are scaled with the respective normalization factors obtained from the background-only fit. Minor backgrounds are grouped together and denoted as ‘Other’. This includes  $t\bar{t}$ -fake,  $t\bar{t} + X$ , multiboson, and other top. The rightmost bin includes the overflowed events.

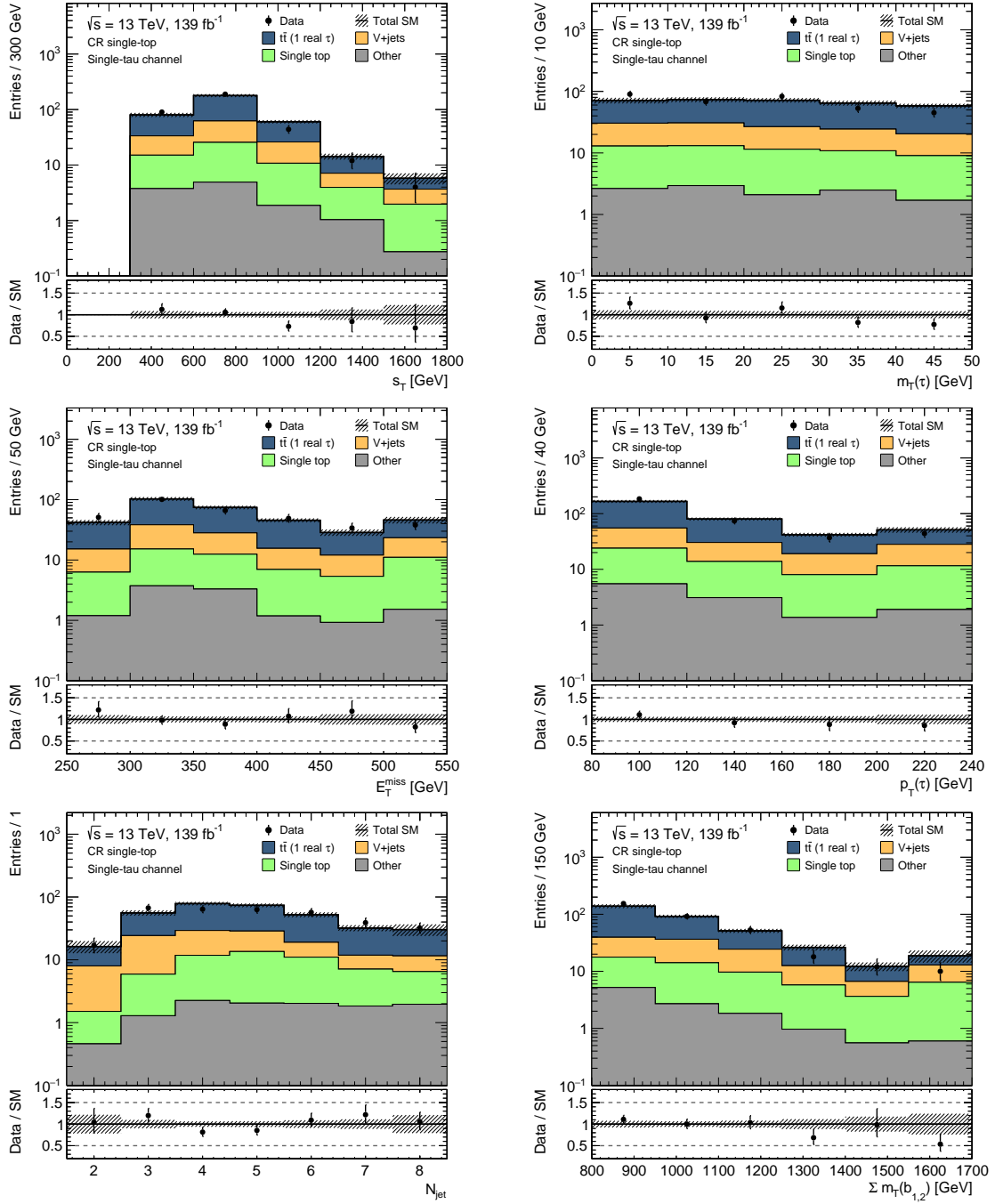


**Figure B.4:** Kinematic distributions in the single-top CR in the single-tau channel. The stacked histograms show the various SM background contributions. The hatched band indicates the total statistical and systematic uncertainty of the background. The expected event yields are scaled with the respective normalization factors obtained from the background-only fit. Minor backgrounds are grouped together and denoted as ‘Other’. This includes  $t\bar{t}$ -fake,  $t\bar{t} + X$ , multiboson, and other top. The rightmost bin includes the overflowed events.

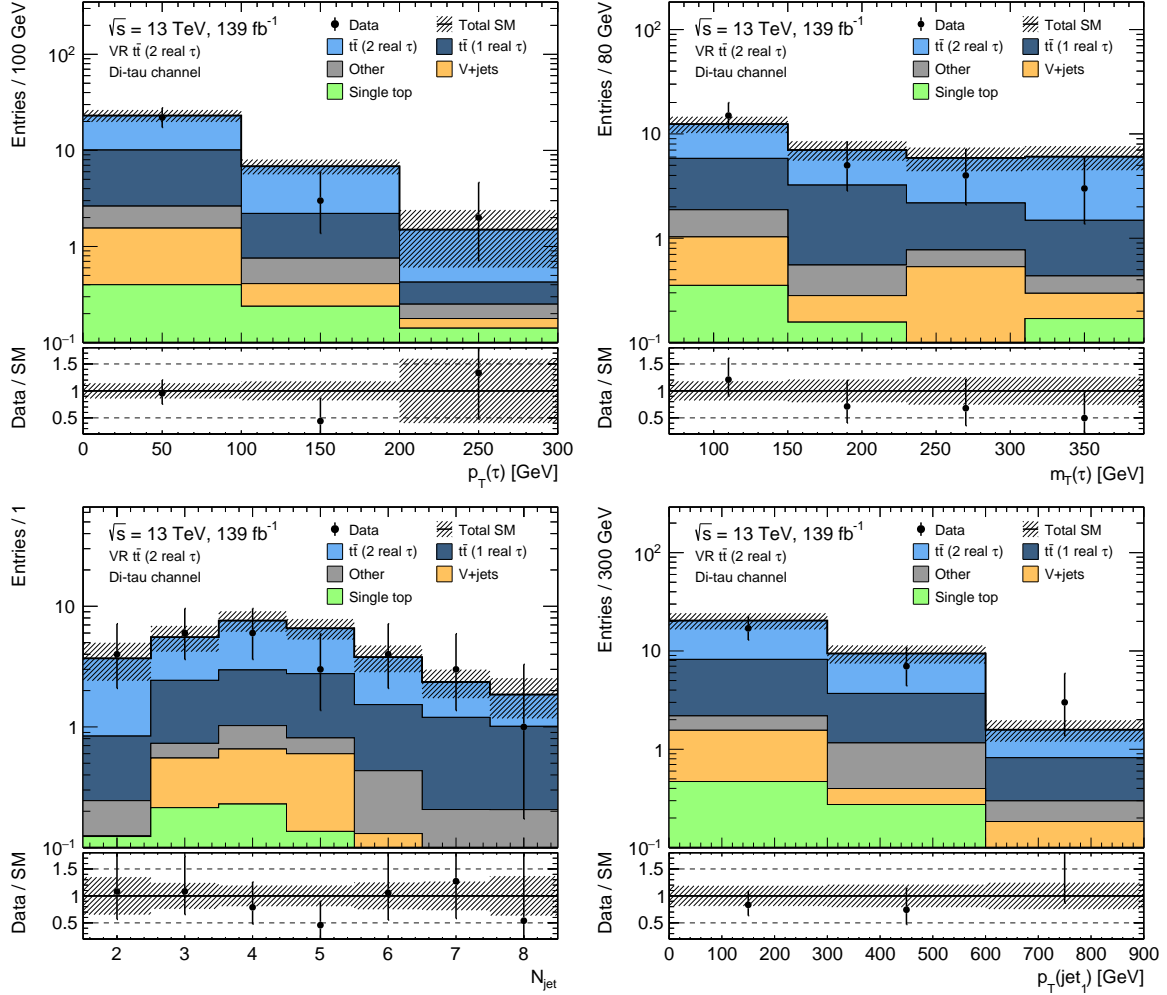


**Figure B.5:** Kinematic distributions in the  $t\bar{t}$  (2 real  $\tau$ ) VR in the di-tau channel. The stacked histograms show the various SM background contributions. The hatched band indicates the total statistical and systematic uncertainty of the background. The expected event yields are scaled with the respective normalization factors obtained from the background-only fit. Minor backgrounds are grouped together and denoted as ‘Other’. This includes  $t\bar{t}$ -fake,  $t\bar{t} + X$ , multiboson, and other top. The rightmost bin includes the overflowed events.

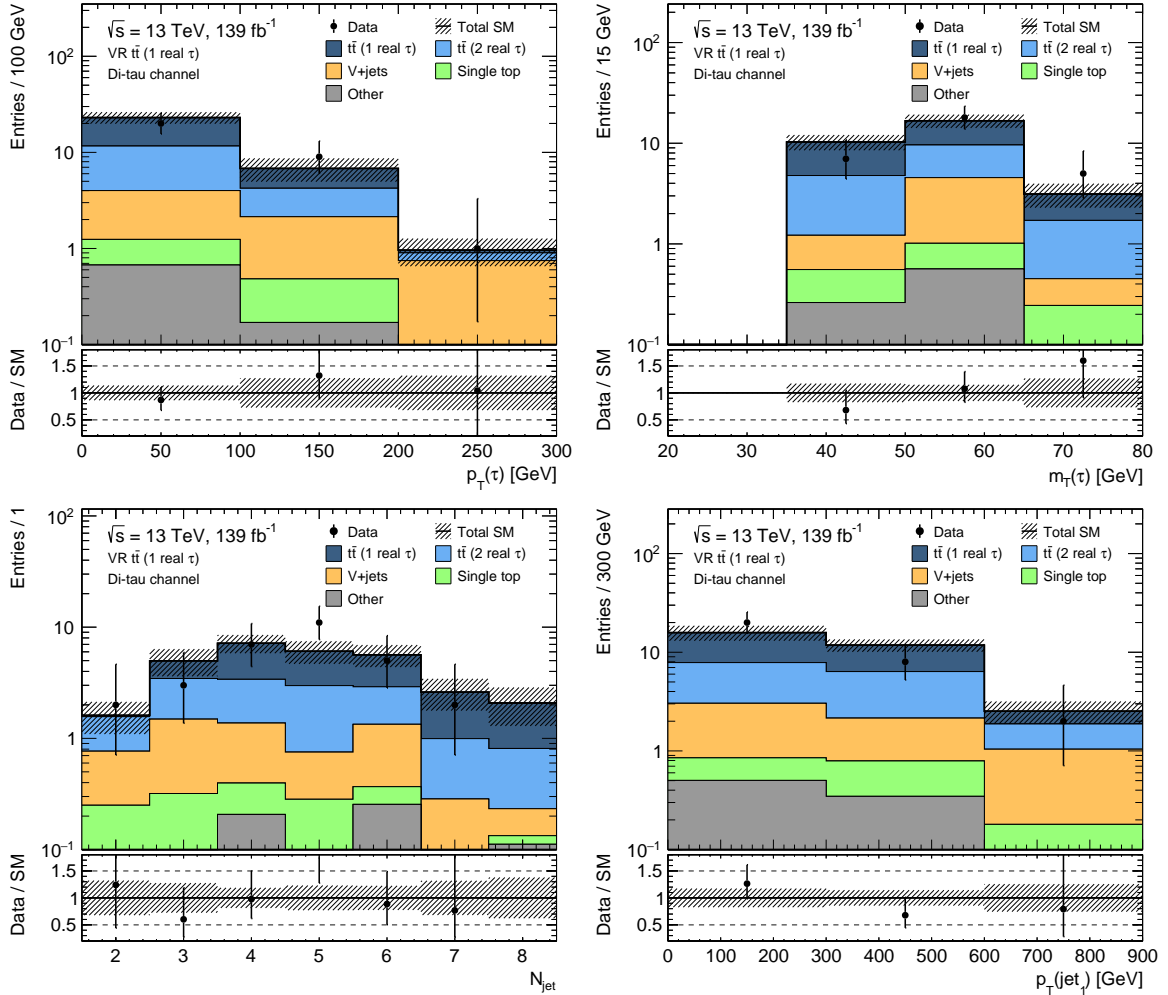


**Figure B.6:** Kinematic distributions in the  $t\bar{t}$  (1 real  $\tau$ ) VR in the di-tau channel. The stacked histograms show the various SM background contributions. The hatched band indicates the total statistical and systematic uncertainty of the background. The expected event yields are scaled with the respective normalization factors obtained from the background-only fit. Minor backgrounds are grouped together and denoted as ‘Other’. This includes  $t\bar{t}$ -fake,  $t\bar{t} + X$ , multiboson, and other top. The rightmost bin includes the overflowed events.

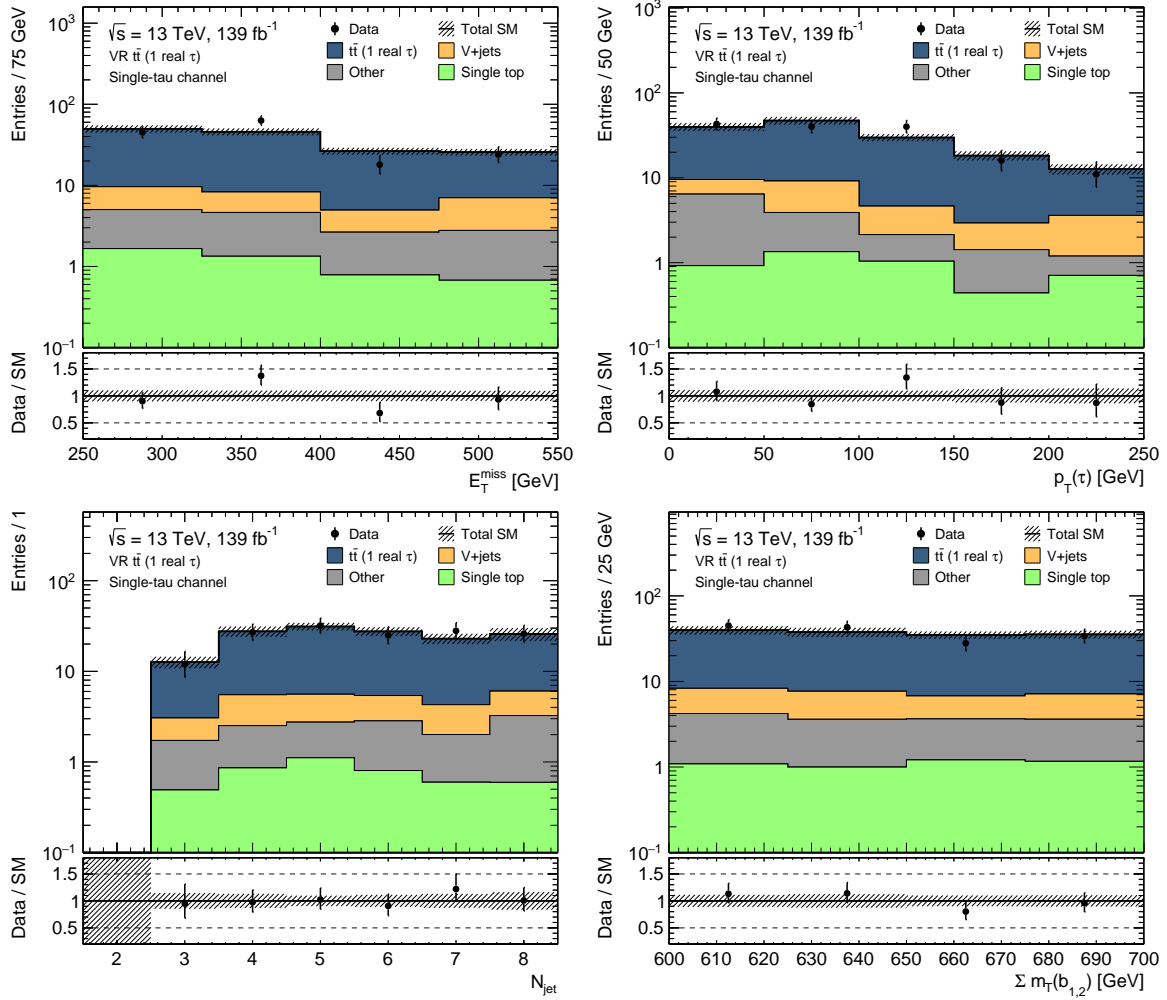


**Figure B.7:** Kinematic distributions in the  $t\bar{t}$  (1 real  $\tau$ ) VR in the single-tau channel. The stacked histograms show the various SM background contributions. The hatched band indicates the total statistical and systematic uncertainty of the background. The expected event yields are scaled with the respective normalization factors obtained from the background-only fit. Minor backgrounds are grouped together and denoted as ‘Other’. This includes  $t\bar{t}$ -fake,  $t\bar{t} + X$ , multiboson, and other top. The rightmost bin includes the overflowed events.

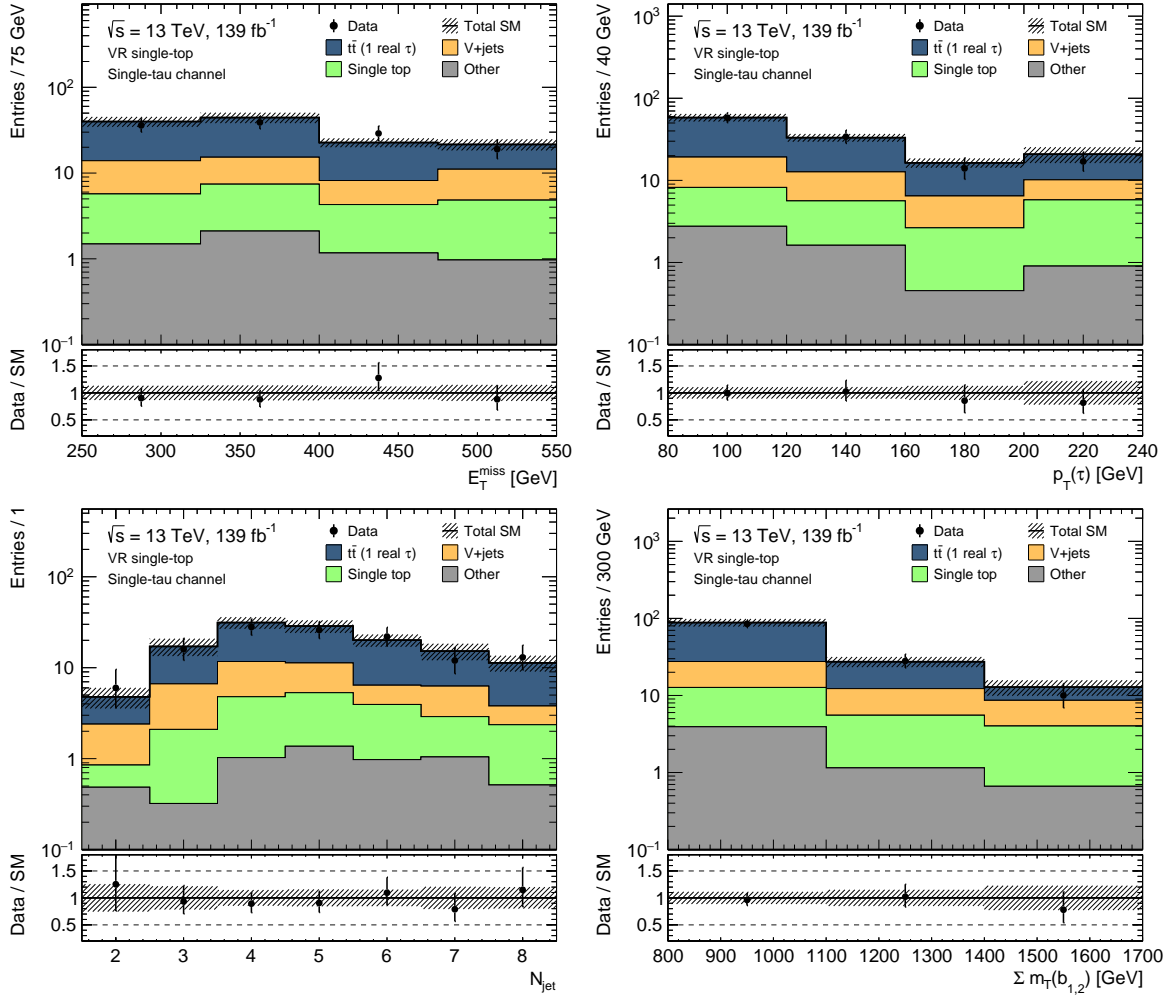


**Figure B.8:** Kinematic distributions in the single-top VR in the single-tau channel. The stacked histograms show the various SM background contributions. The hatched band indicates the total statistical and systematic uncertainty of the background. The expected event yields are scaled with the respective normalization factors obtained from the background-only fit. Minor backgrounds are grouped together and denoted as ‘Other’. This includes  $t\bar{t}$ -fake,  $t\bar{t} + X$ , multiboson, and other top. The rightmost bin includes the overflowed events.

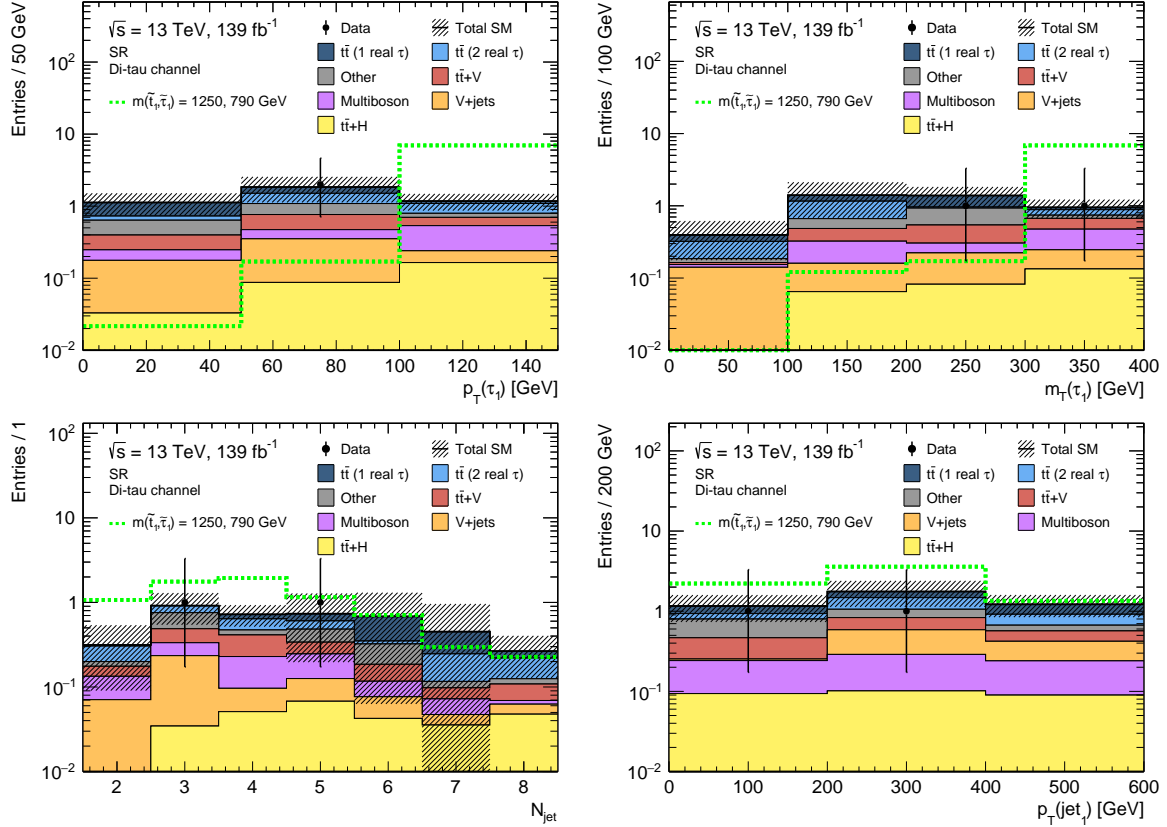


**Figure B.9:** Kinematic distributions in the di-tau SR. The stacked histograms show the various SM background contributions. The hatched band indicates the total statistical and systematic uncertainty of the background. The expected event yields are scaled with the respective normalization factors obtained from the background-only fit. Minor backgrounds are grouped together and denoted as ‘Other’. This includes  $t\bar{t}$ -fake, single top, and other top. The rightmost bin includes the overflowed events.

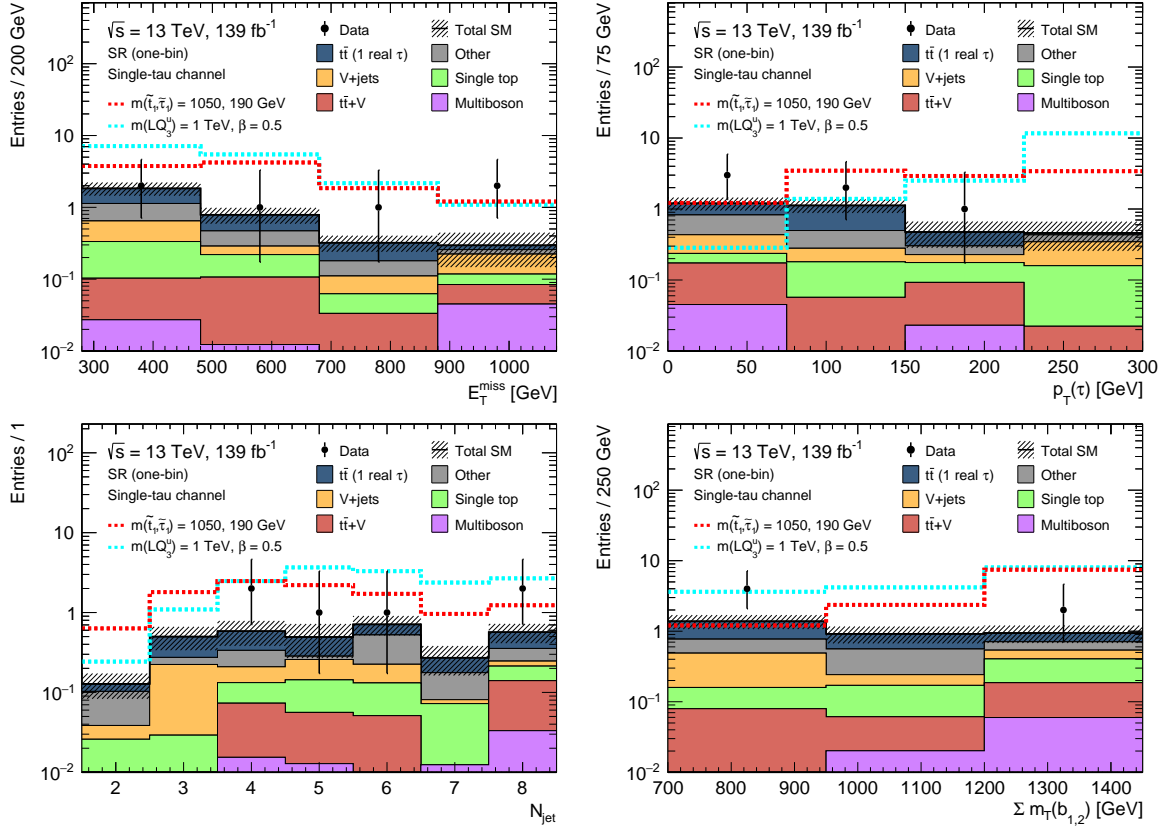


**Figure B.10:** Kinematic distributions in the single-tau one-bin SR. The stacked histograms show the various SM background contributions. The hatched band indicates the total statistical and systematic uncertainty of the background. The expected event yields are scaled with the respective normalization factors obtained from the background-only fit. Minor backgrounds are grouped together and denoted as ‘Other’. This includes  $t\bar{t}$ -fake,  $t\bar{t} + H$ , and other top. The rightmost bin includes the overflowed events.

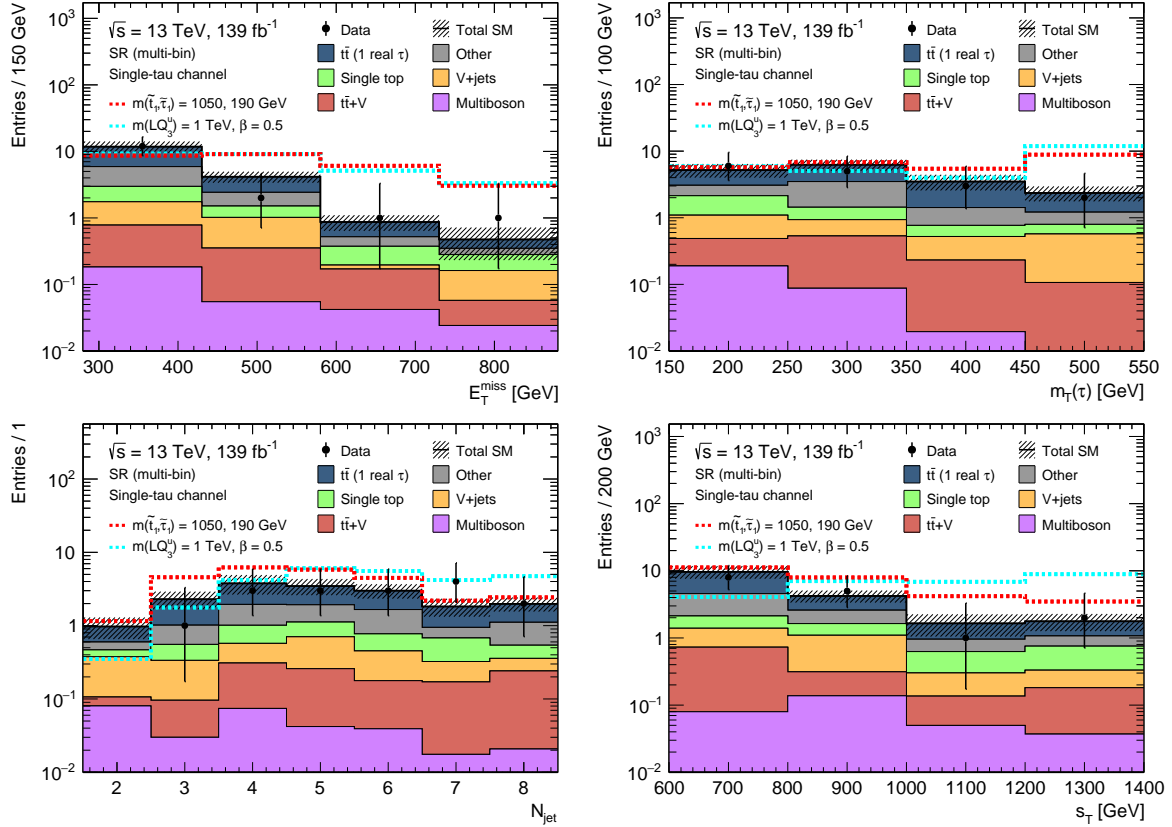


**Figure B.11:** Kinematic distributions in the single-tau multi-bin SR. The stacked histograms show the various SM background contributions. The hatched band indicates the total statistical and systematic uncertainty of the background. The expected event yields are scaled with the respective normalization factors obtained from the background-only fit. Minor backgrounds are grouped together and denoted as ‘Other’. This includes  $t\bar{t}$ -fake,  $t\bar{t} + H$ , and other top. The rightmost bin includes the overflowed events.

# Acknowledgements

I would like to express my gratitude to everyone who supported me on my journey culminating in this thesis.

First of all, I would like to thank Prof. Dorothee Schaile for giving me the opportunity to conduct my research in this intriguing field which is experimental particle physics. I am especially grateful to have had the chance to work abroad at CERN for an extended period of time.

Thank you, Alexander, for supervising my work. Your patience, help and guidance was not only a great source of inspiration but indispensable to bringing this analysis from development to publication stage. It has been a pleasure working with you!

A big thanks goes to each and every one of my colleagues at LMU Munich for your kindness and companionship as well as sharing your knowhow with me. Looking back at the past years, I have learned so much from all of you and will always keep fond memories of this time, in particular of our joint trips to the DPG conferences. Furthermore, I would like to thank my colleagues in the ATLAS collaboration for their support and feedback in regards to my research.

Last but definitely not least, my deepest gratitude goes to my parents for their unconditional support and motivation during these often strenuous times. Really, you are the best!

*“So long, and thanks for all the fish.”* – D. Adams [234]

